

**Characterization of the Dynamic Mechanical Properties of Single
Cardiovascular Cells**

A DISSERTATION
SUBMITTED TO THE FACULTY OF THE
UNIVERSITY OF MINNESOTA

BY

Taylor Marie Rothermel

IN PARTIAL FULFILLMENT OF THE REQUIREMENTS
FOR THE DEGREE OF
DOCTOR OF PHILOSOPHY

Advisor: Dr. Patrick W. Alford

August 2023

Acknowledgements

I am extremely blessed to have been surrounded and supported by a wonderful group of family, friends, and mentors for the duration of my doctoral work. Words cannot describe how much each of you mean to me. Without you, I would not be the person I am today and I am forever grateful.

First and foremost, I must thank my advisor, Dr. Patrick W. Alford, for his patience, encouragement, and wisdom throughout the past six years. I could not have asked for a better advisor and am thankful for all your assistance. Your dedication to each student's personal and professional development is both admirable and appreciated. You foster an environment that makes research enjoyable even when difficult times are encountered. Thank you for teaching me the difference between "effect" and "affect" and for letting me join your lab.

To my fellow Alford lab members: Nick, Elizabeth, Bernie, Sam and Ryan, thank you for all the procrastination conversations and coffee breaks. Elizabeth, you have been a truly exceptional friend to me over the past several years. I will miss our pop culture gossip sessions, conversations about ethics, and dinner/movie dates. Bernie, thank you for always listening to me rant about life and not being frightened of my laugh-crying. I would also like to give a special shout-out to Liz Gacek for being a great friend and helping me find my next job.

I would like to thank my committee members: Dr. Joseph Metzger, Dr. Victor Barocas, and Dr. Kyoko Yoshida. Thank you all for your support, time and expertise. A special thank you to Dr. Metzger and Houda Cohen from his lab who helped me troubleshoot when I encountered problems working with cardiac myocytes.

Most importantly, thank you to my family: Mom, Dad, and Lauren for your unwavering support, unconditional love, and unfaltering belief in me. Mom, thank you for always picking up the phone and listening to me talk even when you didn't understand what I was talking about. Dad, thank you for always sharing an anecdote from your own grad experience to make me feel better when I was floundering. Thank you for always letting me come back home when I needed to reset and just generally being the best. And to the dogs, Penny, Murphy, and Bowman, thank you for the cuddles and for being the "goodest girl" and "bestest boys".

Abstract

Cardiovascular tissues are exposed to complex strains during the cardiac cycle in vivo. Strains can change as a result of disease and surgical interventions necessitating tissues to mechanoadapt to maintain function. Biomechanical models provide insight into tissue behavior and disease progression that can be incorporated into clinically relevant models for guiding treatment to improve patient outcomes. Frameworks for modeling tissue mechanical properties, such as the constrained mixture model, require mechanical descriptions of each individual component of the tissue. For models of cardiovascular tissues, the mechanical behavior of the force generating cells, including vascular smooth muscle cells (VSMCs) in arteries and cardiac myocytes in the heart, must be considered. Cellular microbiaxial stretching (C μ BS) is used to measure and characterize the anisotropic mechanics of cells with in vivo like geometries. Here, C μ BS is used to investigate the dynamic mechanical properties of single cardiovascular cells to better understand changes in mechanical function and cytoskeletal structure in response to large biaxial strains.

First, the contributions of VSMCs to the large-strain nonlinearity of whole vessel mechanics was investigated using C μ BS. The mechanical properties of VSMCs with native-like architectures are highly anisotropic, due to their highly aligned actomyosin cytoskeletons, but inhibition of actomyosin contraction results in nearly isotropic material properties. Additionally, VSMCs have a surprisingly linear stress-strain relationship even at large deformations, and a Holzapfel-Gasser-Ogden type strain energy density function is used to describe individual VSMCs mechanical properties.

To further understand the mechanical behavior of VSMCs to complex loading conditions, cell stress in response to both extension and compression as well as immediate

temporal changes in stress in response to cyclically applied deformations were measured. VSMCs display clear hysteresis under incremental extension and compression and demonstrate cycle-dependent stress-relaxation after cyclic step change extension and compression. A Hill-type active fiber model reproduces all observed hysteresis and cycle-dependent stress-relaxation, suggesting that the temporal stress-strain behavior of the cell is regulated by actomyosin contraction and relaxation, rather than passive viscoelasticity.

Finally, the sarcomere length-tension relationship in single neonatal cardiac myocytes was investigated using C μ BS. Cardiac myocytes have a highly organized structure. Using C μ BS, the length between sarcomeres was changed as a function of applied stretch. When stretching cells such that the length between sarcomeres changes, the force generated by the cells changes consistent with previous understanding of the length-tension curve. Stretching cells perpendicular to sarcomere alignment holds the length between sarcomeres relatively constant, but the active force of contraction changes with stretch, decreasing as the cell was extended and compressed. A relatively simple active contraction based model, dependent on lattice and sarcomere spacing, robustly recapitulates the experimentally observed behavior. These results indicate that the active force of contraction of cardiac myocytes is dependent on both lattice spacing and length between sarcomeres.

Altogether, this work aims to elucidate the nonlinear mechanical properties of cardiovascular cells and aid in creating constitutive models of cardiovascular mechanics. This has important implications for modeling in mechanobiology as VSMCs and cardiac myocytes are mechanosensitive and actively remodel to maintain function.

Table of Contents

Acknowledgements.....	i
Abstract.....	iii
Table of Contents.....	v
List of Figures.....	ix
Chapter 1. Introduction.....	1
1.1 Cardiovascular disease epidemiology and pathophysiology.....	1
1.2 Considerations for studying cardiovascular tissue and single cell biomechanics	2
1.3 Significance.....	4
Chapter 2. Large-Deformation Strain Energy Density Function for Vascular Smooth Muscle Cells.....	6
2.1 Summary.....	6
2.2 Introduction.....	7
2.3 Methods.....	8
2.3.1 C μ BS Substrates Preparation.....	8
2.3.2 Cell Culture.....	10
2.3.3 Large Deformation Uniaxial Testing.....	10
2.3.4 Cell Stress Analysis.....	11
2.3.5 Cell Architecture Analysis.....	13
2.3.6 Planar Strain Energy Density Function Determination.....	15
2.4 Results.....	17
2.4.1 F-Actin is realigned during large deformation stretching, but not plastically deformed.....	17

2.4.2	VSMC stress-strain relationship is anisotropic.....	17
2.4.3	VSMC stress anisotropy is primarily due to the actomyosin cytoskeleton.	19
2.4.4	VSMC stress-strain behavior can be described by a linear fiber model.	21
2.5	Discussion	23
Chapter 3. Anisotropic Mechanics of Vascular Smooth Muscle Cells Exposed to		
Dynamic Loads		
3.1	Summary	28
3.2	Introduction	29
3.3	Methods.....	31
3.3.1	Cellular Microbiaxial Stretching.....	31
3.3.2	Cell Culture.....	31
3.3.3	Stretching Protocols.....	33
3.3.4	Cell Stress Analysis.	36
3.3.5	Hill-Type Active Fiber Model.	39
3.4	Results	41
3.4.1	VSMCs with elongated geometry are anisotropic and demonstrate hysteresis under both tensile and compressive loading	41
3.4.2	A Hill-type active fiber model recapitulates anisotropic mechanical behavior of VSMCS under complex loads.....	45
3.4.3	VSMCs demonstrate temporally dynamic stress-strain behavior.....	45
3.4.4	A Hill-type active fiber model predicts the cycle-dependent stress relaxation of VSMCs.....	48
3.5	Discussion	48

Chapter 4. An experimentally validated model of the length tension relationship in cardiac myocytes.....	54
4.1 Introduction	54
4.2 Methods.....	56
4.2.1 Cellular Microbiaxial Stretching.....	56
4.2.2 Neonatal mouse cardiac myocyte isolation.....	59
4.2.3 Stretching protocol.....	59
4.2.4 Force analysis.....	60
4.2.5 Cell architecture analysis.....	61
4.2.6 Activation based model for active force of contraction.	62
4.3 Results	64
4.3.1 Sarcomere spacing changes linearly with measured cellular deformations applied with C μ BS.....	64
4.3.2 Cardiac myocyte force of contraction is anisotropic in response to biaxial strains.	65
4.3.3 Consideration of the radial organization of actin and myosin in modeling captures the biphasic force response to biaxial stretching.....	68
4.4 Discussion	71
Chapter 5. Conclusions.....	76
5.1 Summary	76
5.2 Impact.....	76
5.3 Future directions.....	77
Bibliography	80

Appendix A. PDMS 527 coated membranes functionalized with fluorescent beads as
TFM substrates for C μ BS 113

A.1 Introduction 113

A.2 Methods 114

 A.2.1 Preparation of PDMS coated membranes 114

 A.2.2 Silanization and functionalization of PDMS coated membranes 115

 A.2.3 Micropatterning fibronectin for cell adhesion 116

A.3 Preliminary Results 117

 A.3.1 Strains are linearly transferred to the functionalized PDMS substrates. .. 117

 A.3.2 Cells are able to be micropatterned on the surface and their tractions
measured using functionalized PDMS substrates..... 117

A.4 Conclusions 119

List of Figures

Figure 2.1. C μ BS apparatus and methods for measuring cell stress.....	9
Figure 2.2. VSMC cell stress calculations.....	13
Figure 2.3. Actin architecture during stretching.....	14
Figure 2.4. C μ BS microscopy for a representative VSMC.....	18
Figure 2.5. Strip-biaxial test of individual VSMCs.....	19
Figure 2.6. C μ BS microscopy for a representative passivated VSMC.....	19
Figure 2.7. Strip biaxial tests of VSMCs with HA-1077 inhibited actomyosin complexes.	20
Figure 2.8. HGO model fits to experimental data.....	22
Figure 3.1. Cellular microbiaxial stretcher.....	33
Figure 3.2. Incremental Stretching Protocol.....	35
Figure 3.3. Cyclic stretch protocol.....	38
Figure 3.4. Incremental Stretching C μ BS Experiments.....	42
Figure 3.5. Hill-type active fiber model fit to incremental stretching results.....	44
Figure 3.6. Cyclic Stretching C μ BS Experiments.....	47
Figure 3.7. Hill-type active fiber model applied to cyclic step-change protocol.....	49
Figure 4.1. C μ BS used to measure single neonatal cardiac myocyte contraction forces.....	58
Figure 4.2. Sarcomere length changes during C μ BS.....	61
Figure 4.3. Active force of contraction for cardiac myocytes during C μ BS.....	67
Figure 4.4. Active contraction based model considering sarcomere length and lattice spacing recapitulates experimentally observed force trends.....	70

Figure A.1. Functionalized PDMS substrates function similarly to polyacrylamide gels
for performing TFM and C μ BS..... 118

Chapter 1. Introduction

1.1 Cardiovascular disease epidemiology and pathophysiology

Cardiovascular disease is the leading cause of death in the United States and responsible for approximately 31% of deaths worldwide annually [1]. As a result of cardiovascular disease, the mechanical environment experienced by cells and tissues changes causing maladaptive remodeling. In arteries, increased pressure from hypertension causes the vessel walls to thicken and stiffen [2]. In the heart, left ventricular hypertrophy and dilated cardiomyopathy involve the heart growing concentrically or eccentrically in response to pressure or volume overload, respectively. Left ventricular hypertrophy is the thickening of the wall of the left ventricle to compensate for elevated blood pressure, which commonly results from hypertension or aortic stenosis [3]. In dilated cardiomyopathy, the ventricle walls thin as the ventricle increases in volume to compensate for volume overload and decreased ejection fraction resulting from a weakened heart muscle [4]. Additionally, many cardiovascular diseases require surgical intervention, such as corrections for congenital heart defects in infants. Following surgery, the heart muscle, which is optimized for uniaxial contraction, is exposed to abnormal loading conditions [5]–[8].

In the heart, cardiovascular disease causes a marked change in physiology, not only on the tissue level, but also at the cellular level that corresponds to a change in overall function. In the heart, cardiac myocytes, the contractile cells for force generation, exhibit a tightly controlled geometry and cytoskeletal organization to function optimally. Further, cardiac myocytes play an important role in remodeling the heart in development[9], [10] and various cardiovascular pathologies[11]–[13]. Cardiac myocytes are exposed to

constant applied deformations during the cardiac cycle and are sensitive to mechanical stimuli such as strain and substrate stiffness [14]–[17]. Cardiac myocyte remodeling reflects the remodeling of the heart as a whole. In left ventricular hypertrophy, where the walls thicken in response to pressure overload, cardiac myocytes add sarcomeres in parallel to increase their cross-sectional area [11], [12]. Similarly, cardiac myocytes in dilated cardiomyopathy add sarcomeres in series increasing their length as the ventricle enlarges [11], [13]. Maladaptive remodeling in cardiac myocyte could be responsible for thickening or dilation of the ventricle wall by adding sarcomeres in parallel or in series, respectively, in an attempt to change the stress experienced by the cell [11], [18].

Biomechanical models are useful for predicting disease development [19] and evaluating surgical outcomes [20]–[22]. Because of its impact and prevalence, improving understanding of cardiovascular mechanics will enable the creation of better, clinically relevant models for cardiovascular disease to improve patient outcomes and guide treatment.

1.2 Considerations for studying cardiovascular tissue and single cell biomechanics

Cardiovascular tissues must adapt to perturbations in their mechanical environment in order to maintain tissue integrity and functionality [23]. However, the exact mechanisms by which cells and tissues sense and adapt to their surrounding mechanical environment are not fully understood. Vascular smooth muscle cells in the arterial wall and cardiac myocytes in the heart play important roles in tissue function and remodeling as they are the primary force generating cell types in their respective tissue and are sensitive to mechanical stimuli. Mechanical stimuli, such as substrate stiffness and shape, influence

cell function, which alters function on the tissue scale. In cardiac myocytes, cell shape influences calcium signaling and fiber alignment [14]–[16] and static strains alter stretch-activated ion channels [17] and cause remodeling by sarcomere addition [24], [25].

Biomechanical models can be used to understand and predict how tissues will respond and adapt to mechanical stimuli. Common frameworks for modeling tissue level mechanical properties, such as the constrained mixture model, require mechanical descriptions of each individual component within the tissue to create predictive models [26]. In order to formulate predictive models of behavior for the cardiovascular system, it is imperative that the biomechanical response of these cells be characterized.

Single-cell biomechanical properties can be examined in a variety of ways such as atomic force microscopy [27], [28], carbon fiber cantilevers [29]–[32], PDMS micropillar array detectors (μ PADs)[33], [34], and magnetic twisting cytometry[35], [36]. However, some methods for measuring cellular mechanical properties are typically limited to describing isotropic, linear moduli at small strains [37]. These methods have improved understanding of cellular mechanics; however, they are best suited reporting bulk moduli for isotropic descriptions of the cell and typically fail to account for the structural anisotropy of the cellular cytoarchitecture in whole cell mechanical descriptions. Many cells have highly organized cytoskeletal architectures indicating potentially important anisotropic contributions to their mechanobiology that must be included in a full description of cellular mechanical properties. On the tissue scale, the orientation of fibrous matrices confers many biological tissues with anisotropic mechanical properties [38]. In vitro tissue models, like muscular thin films demonstrate that cellular architecture influences cell functional contractility in smooth muscle [39]–[41], cardiac [39], [42], and

skeletal muscle [43] cells, suggesting that anisotropic descriptions of cell properties are needed.

Cellular microbiaxial stretching (C μ BS) was developed to measure the anisotropic mechanical properties of cells by performing biaxial mechanical tests on single cells micropatterned with in vivo like geometries to account for cytoskeletal organization [44]. Using C μ BS, we are able to probe the force-feedback relationship in single cells by simultaneously applying controlled deformations to single cells and measuring the resulting changes in cell stress. C μ BS utilizes traction force microscopy to quantify traction stresses of cells during stretch. C μ BS is advantageous because it allows the measurement of anisotropic cell stress while controlling cell geometry, substrate mechanics, and applied strains.

1.3 Significance

Cells, like tissues, have complex anisotropic mechanical properties that evolve during mechanotransduction and mechanoadaptation. Studying the mechanical properties of cells is important for understanding the biomechanics of tissues and formulating predictive mechanical models of tissues. There is a need to understand how changes in the mechanical environment of cells influence cell function. Evaluating how the stress and contractility of single cells evolves under complex loading conditions is difficult to study, and current studies have yet to capture the full mechanical properties and mechano-adaptive behavior of single cardiovascular cells. Because of the unique combination of tunable parameters, the C μ BS assay allows for novel measurements of cellular mechanics and mechanoadaptation. Here, I use C μ BS to simultaneously measure the anisotropic stress and cytoskeletal organization of cardiac myocytes exposed to complex loads to

characterize their dynamic mechanical properties while also using measurements of their cytoskeletal architecture to create simple, biologically relevant mechanical models of their behavior. Taken together the findings presented in this thesis provide a clearer understanding of the single cell mechanical response to applied deformations. This has important implications for understanding cellular mechanoadaptation and may ultimately lead to better understanding of the nonlinear mechanical properties of cardiac myocytes necessary for creating constitutive models of cellular mechanics and growth and remodeling.

Chapter 2. Large-Deformation Strain Energy Density Function for Vascular Smooth Muscle Cells

This chapter contains material published in the Journal of Biomechanics and is reproduced with permission from reference [45]. Rothermel, T.M., Win, Z. and Alford, P.W., 2020. Large-deformation strain energy density function for vascular smooth muscle cells. *Journal of Biomechanics*, 111, p.110005.

2.1 Summary

Vascular tissue exhibits marked mechanical nonlinearity when exposed to large strains. Vascular smooth muscle cells (VSMCs) are the most prevalent cell type in the artery wall, but it is unclear how much of the vessel nonlinearity is attributable to VSMCs. Here, we used cellular microbiaxial stretching (C μ BS) to measure the large-strain mechanical properties of individual VSMCs. We find that the mechanical properties of VSMCs with native-like architectures are highly anisotropic, due to their highly aligned actomyosin cytoskeletons, and that inhibition of actomyosin contraction with rho-associated kinase inhibitor HA-1077 results in nearly isotropic material properties. We further find that when VSMCS are exposed to large strains (up to 60% stretch), the cells' stress-strain behavior is surprisingly linear. Finally, we modified a previously published Holzapfel-Gasser-Ogden type strain energy density function to characterize individual VSMCs, to account for the observed large-deformation linearity. These data have important implications in the development of models of vascular mechanics and mechanobiology.

2.2 Introduction

Arteries exist in dynamic mechanical environments, necessitating active contraction and dilation to regulate blood flow dynamics [46], [47]. Changes in the mechanical environment, such as those experienced in vascular pathologies, induce arteries to remodel, altering vessel mechanical properties [48], which in turn can impact cell behavior [49]. A better understanding of arterial response to mechanical stimuli will help inform better models of disease progression.

Arteries have nonlinear mechanical properties, with stiffness typically increasing with increasing strain [50]–[52]. An artery has three primary layers comprised of three main components: cells, collagen, and elastin. The mechanical response of an artery is dependent on the collective behavior of these layers and components [53]–[55]. A common method for modeling artery mechanics, growth, and remodeling, is the constrained mixture model, which accounts for contributions of individual constituents [26], [56]–[58]. Since each component is treated separately, it is important to determine the mechanical properties of each of the components of the vessel.

Vascular smooth muscle cells (VSMCs) are the most prevalent cells in the arterial wall. VSMCs wrap circumferentially around the vessel and typically have an elongated spindle shape [59]. VSMCs are responsible for maintaining physiological function of the vessels [47] and can undergo strains of up to ~15% per cardiac cycle [60]. VSMCs respond to mechanical cues, which influence cellular functions such as protein synthesis [61], focal adhesion formation [62], and cytoskeletal organization [62].

Cells have complex, temporally-dynamic mechanical properties and are often characterized as viscoelastic materials because they display hysteresis, creep, and stress

relaxation behaviors similar to viscoelastic materials [63], [64]. Cellular mechano-adaptation via actomyosin contraction [65] and remodeling [66] has also been observed. Current methods for measuring cellular mechanical properties include atomic force microscopy [67], [68] and magnetic twisting cytometry [69], [70]. These methods are best suited for describing linear isotropic cellular properties. In vivo, however, cells likely have anisotropic mechanical properties due to anisotropic organization of the cytoskeleton. Cellular microbiaxial stretching (C μ BS) has been developed as a method to measure the nonlinear anisotropic mechanical properties of single cells [44].

Recently, we have shown that under relatively small strains, the stress-strain behavior of VSMCs can be described by a Holzapfel-Gasser-Ogden (HGO) type strain energy density function [44]. However, whole-vessel mechanical properties are notably nonlinear at larger strains, and large deformation studies up to 60-70% applied strain are used to investigate and characterize their mechanical properties. It is unknown whether VSMCs are similarly nonlinear at large strains. Here, we use C μ BS to measure the large-strain anisotropic mechanical properties of individual VSMCs. We find that the mechanical response of VSMCs is consistent with previous anisotropic descriptions, and is surprisingly linear even at large deformations.

2.3 Methods

2.3.1 C μ BS Substrates Preparation.

Micropatterned C μ BS substrates (Fig. 2.1(a-c)) were prepared as previously described [44]. Briefly, fluorescent bead-doped polyacrylamide (PA) gels with an elastic modulus of 13.5 kPa were adhered on top of elastic PDMS membranes fixed between metal brackets under slight tension (Fig. 2.1(a-b)). PDMS stamps with arrays of 4000 μm^2

rectangles of aspect ratio of two (AR2) ($91\mu\text{m} \times 44\mu\text{m}$) were fabricated using standard photolithography techniques. The stamps were used to microcontact print rectangular patterns of human fibronectin onto a glass coverslip which were then transferred to the PA gel (Fig. 2.1(c)).

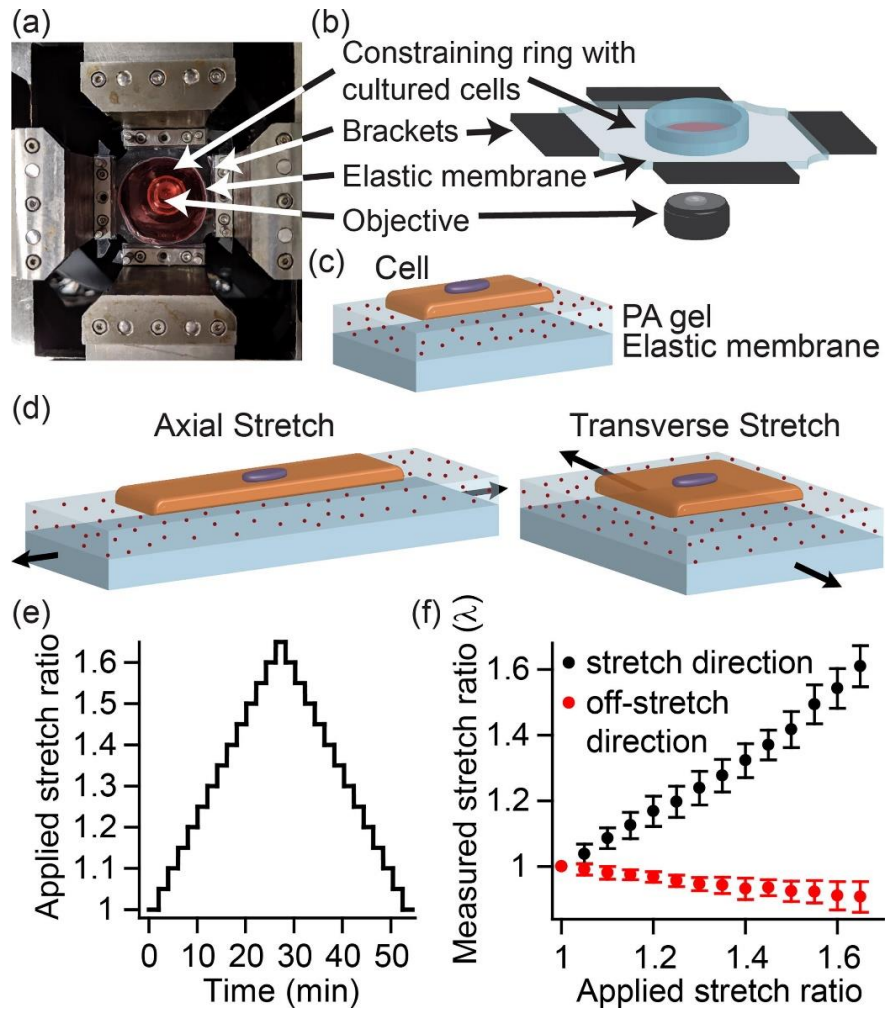


Figure 2.1. C μ BS apparatus and methods for measuring cell stress.

(a) C μ BS device and substrates mounted on the microscope. (b) Schematic representation of C μ BS. (c) Schematic representation of the cells micropatterned on the substrate. (d) Schematic representation of the cells and substrates during axial stretch (parallel to the long axis of the cell) and transverse stretch (perpendicular to the long axis of the cell). (e) Applied stretch (λ_x or λ_y) for one stretch cycle. (f) Applied stretch versus measured substrate stretch.

2.3.2 Cell Culture.

Human umbilical artery VSMCs (Lonza) were obtained at passage 3 and cultured at 37°C and 5% CO₂ in growth media composed of Medium 199 (GenDEPOT, Baker, TX), 10% FBS (Gibco, Grand Island, NY), 10 mM 4-(2-hydroxyethyl)-1-piperazineethanesulfonic acid (Gibco), 3.5 g/L glucose (Sigma-Aldrich, St. Louis, MO), 2mg/L vitamin B12 (Sigma-Aldrich), 50 U/mL penicillin–streptomycin (Gibco), 1% minimal essential medium nonessential amino acids (Gibco), and 2mM L-glutamine (Gibco). Cells between passage 5 and 7 were used for experiments. Cells were seeded onto the micropatterned C μ BS substrates at a density of ~30 cells/mm². The cells were allowed to adhere to the micropatterned fibronectin islands for 24 hours and then serum starved, using the same growth media formula above, but without the FBS, for 24-48 hours before conducting C μ BS experiments. Experiments were conducted in Tyrode's solution at 37 °C.

2.3.3 Large Deformation Uniaxial Testing.

VSMCs were stretched either axially (parallel with the long axis of the cell) or transversely (parallel with the short axis of the cell) (Fig. 2.1(d)). The stretching protocol began with a priming stretch to the maximum stretch ratio $\lambda=1.65$, where $\lambda = \frac{\text{deformed length}}{\text{undeformed length}}$, to eliminate any slippage between the membrane and the bracket, followed by a second stretch to locate cell positions in the deformed state. The experimental stretch was then performed by increasing the stretch ratio in step-wise increments of 0.05 at stretch rate 0.005/sec from 1.0 to 1.65 applied stretch ratio. The C μ BS device allows for near strip biaxial testing, with deformations perpendicular to the stretch direction ~15% of those in the stretch direction. The substrates were held at each position for 2 min to acquire bright field images of the cell and fluorescent images of the cell deformed bead layer. After

reaching the maximum applied stretch ratio, the constructs were then unloaded by stretch increments of 0.05 at the same rate and held at each position for 2 min for image acquisition (Fig. 2.1(e)). Once the substrate returned to its initial configuration, the cells were lysed with a 0.5% sodium dodecyl sulfate (SDS) solution and an identical stretching protocol was applied to capture cell-free images, providing the undeformed reference configuration of the fluorescent bead layer. To determine the passive properties of the cell, a saturating dosage of 100 μM of Rho-associated kinase (ROCK) inhibitor HA-1077 was added to the cells for 1 hour prior to stretching to induce relaxation. HA-1077 inhibits actomyosin contractility and has previously been shown to eliminate nearly all tension in the cell at this concentration [71]–[73]. After treatment, the same stretching protocol was used and images were acquired at each deformed position. The substrate stretch ratio was measured via brightfield imaging and compared to the applied stretch ratio (Fig. 2.1(f)).

2.3.4 Cell Stress Analysis.

A particle image velocimetry (PIV) algorithm was used to find the cell-induced bead displacement between the with- and without-cell images of the fluorescent bead layer at each deformed position (Fig. 2.2(a)). Traction stress vector fields were determined from bead displacements using an unconstrained Fourier transform traction cytometry algorithm (regularization factor: $1\text{E-}9$, Poisson's ratio: 0.5) [74]. The force field was composed of substrate traction force vectors defined by $\mathbf{T}^n a^n$ where $\mathbf{T}^n = T_x^n \mathbf{e}_x + T_y^n \mathbf{e}_y$ is the traction vector acting on area a^n and \mathbf{e}_i is the unit vector in the i direction (Fig. 2.2(b)). Forces are balanced at the interface between substrate tractions and cell forces (\mathbf{f}^n), such that $\mathbf{f}^n = f_x^n \mathbf{e}_x + f_y^n \mathbf{e}_y = -T_x^n a^n \mathbf{e}_x + -T_y^n a^n \mathbf{e}_y$. Forces oriented away from the center of the cell were denoted as tensile (positive). The total tensile force was given as $2f_x = \sum_n f_x^n r_x^n / |r_x^n|$

and $2f_y = \sum_n f_y^n r_y^n / |r_y^n|$, where $\mathbf{r}_n = r_x^n \mathbf{e}_x + r_y^n \mathbf{e}_y$ is the vector that described the location of n with respect to the cell center. The first Piola-Kirchhoff (PK1) stresses, represented by $P_x = (f_x/A_x)$ and $P_y = (f_y/A_y)$, was calculated at the midplane of the cell using the total tensile force and the undeformed cross sectional area of the cell (Fig. 2.2(c)). The cross sectional areas were measured in a previous study to be $A_x = 99 \mu\text{m}^2$ and $A_y = 199 \mu\text{m}^2$ [44].

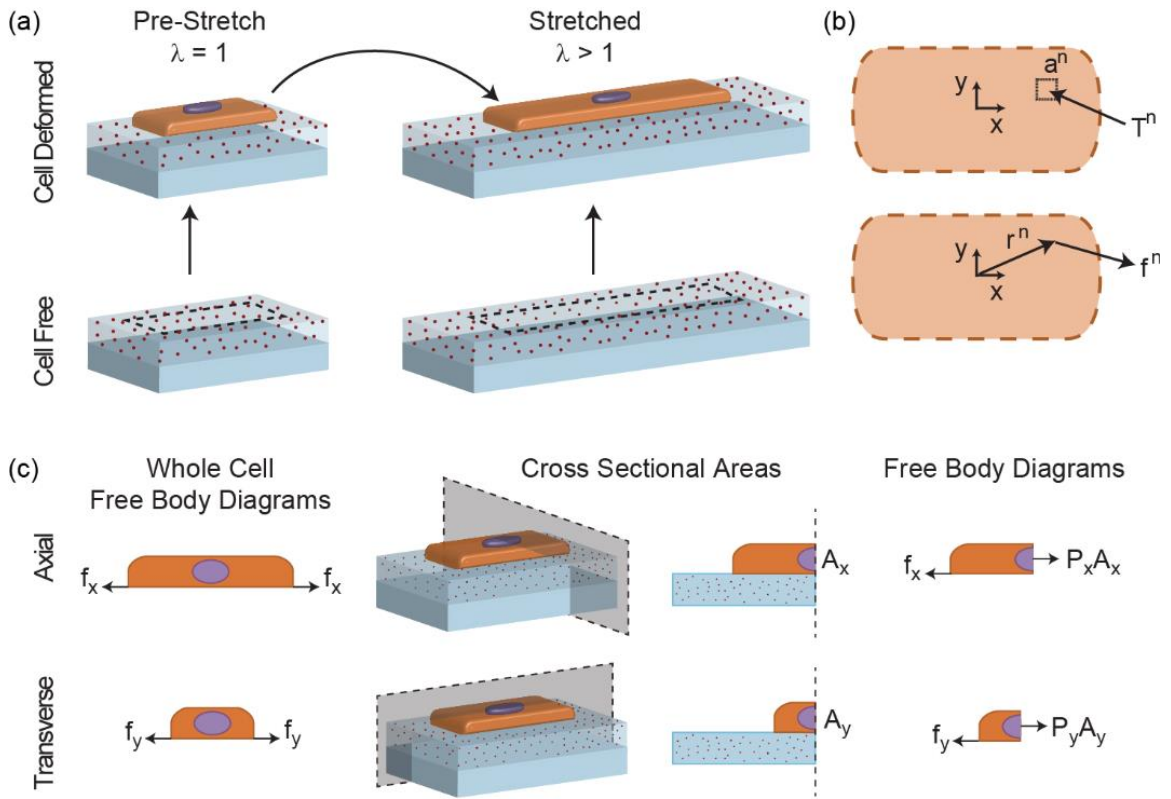


Figure 2.2. VSMC cell stress calculations.

(a) Cell and substrate deformation pre-stretch ($\lambda=1$) and stretched ($\lambda>1$) showing cell-induced substrate displacement of the polyacrylamide gel at both positions, (b) substrate surface traction stress T^n acting on area a^n (top) and the cell force f^n at position r^n relative to the center of the cell, (c) free body diagrams for whole-cell equilibrium (left), schematic of the cross sectional planes bisecting the cell (middle-left), cross sectional area along the bisecting plane (middle-right), and the free body diagram describing the midplane stress (right).

2.3.5 Cell Architecture Analysis.

Micropatterned VSMCs were incubated in serum-free media with 1 μM SIR actin and 1 μM verapamil (Spirochrome) for 1 hr to fluorescently stain F-actin fibers. Constructs were placed in Tyrode's solution and were stretched as described above. At each step,

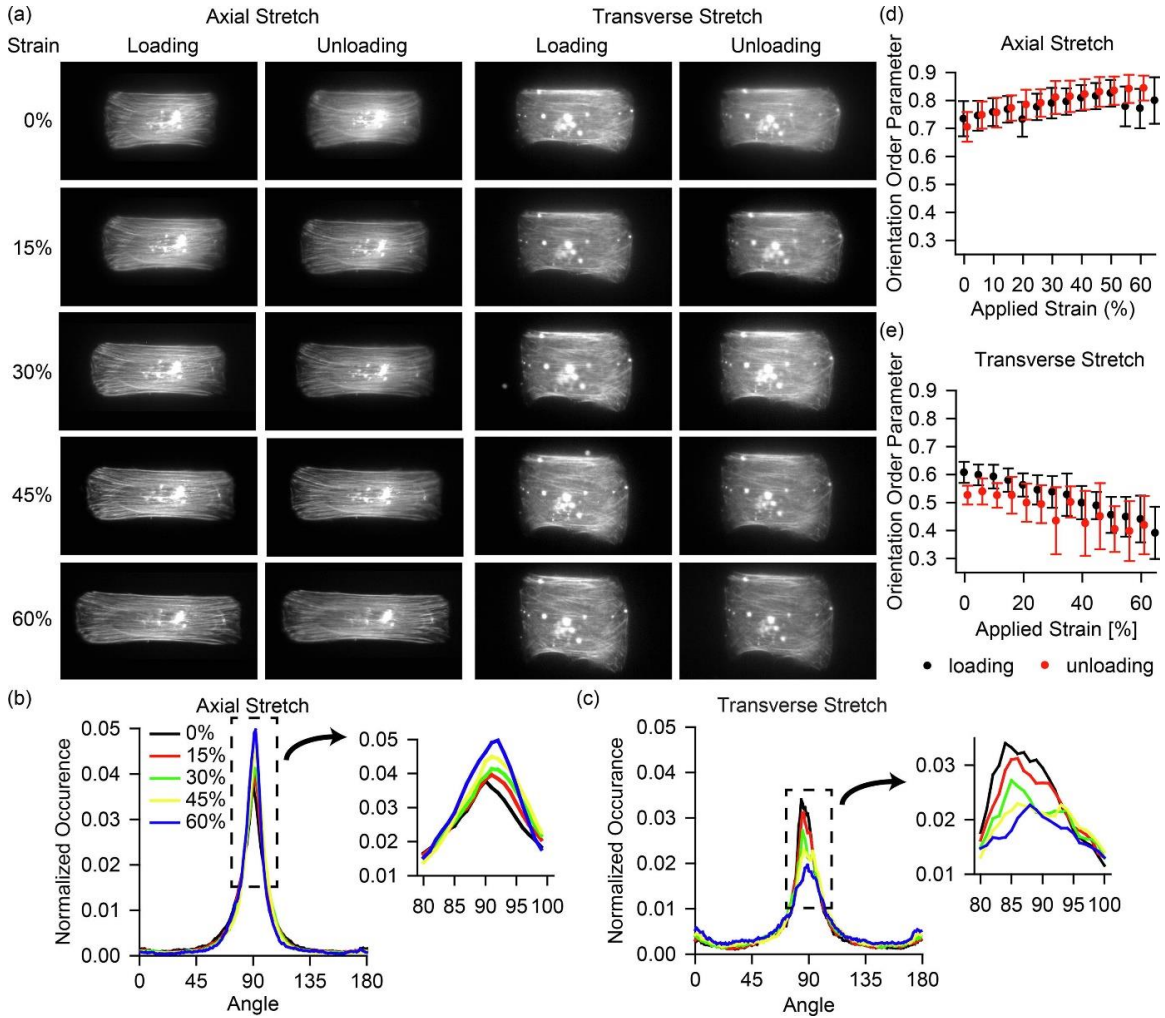


Figure 2.3. Actin architecture during stretching.

(a) Representative SIR-actin imaging of VSMCs during loading and unloading. (b) Actin alignment increases during axial loading, inset: peaks of alignment data. (c) Actin alignment decreases during transverse loading, inset: peaks of alignment data. (d) Orientation order parameter (OOP) during axial loading (black) and unloading (red). (e) OOP during transverse loading (black) and unloading (red). (n=8 for axial stretching and n=2 for transverse stretching) (mean +/- standard deviation)

fluorescent images of the F-actin fibers in the cytoskeleton of the VSMCs were acquired

(Fig. 2.3(a)). A custom Matlab script was used to threshold the images to identify F-actin fibers. The orientation of the fibers was determined using a ridge-detection algorithm [73], [75], [76]. Circular statistics [77] were used to determine the orientation order parameter (OOP), which quantifies actin fiber alignment on a scale ranging from 0 to 1 where 0 is completely isotropic and 1 is completely anisotropic.

2.3.6 Planar Strain Energy Density Function Determination.

Cells were treated as anisotropic and incompressible uniform materials undergoing planar deformation. The deformation of the cell was assumed to be in the principal orientation, and the deformation gradient tensor is given by $\mathbf{F} = \text{diag}[\lambda_x, \lambda_y, \lambda_z]$ where λ_i is the stretch ratio in the i direction. The first Piola-Kirchhoff stress in the i direction (P_i) is given by $P_i = \frac{dW}{d\lambda_i} - \frac{p}{\lambda_i}$, where W is the strain energy density of the cell and p is the Lagrange multiplier given by $p = \lambda_z \frac{dW}{d\lambda_z}$ when $P_z = 0$.

The cell was assumed to be composed of pre-stressed actomyosin fibers in an isotropic matrix with shear modulus μ_m . The fiber stiffness is characterized by parameter C_f and the stress-free shortening that the fiber would undergo if unconstrained is given by λ_a . Fiber orientation was given by the measured orientation probability density in the x-y plane with an assumed Gaussian distribution out of the x-y plane. A structure tensor given by $\mathbf{H} = \alpha_{ij} \mathbf{e}_i \mathbf{e}_j$ was used to characterize the fiber orientations [78].

As previously described [44], [78], fiber orientation was given by the $\mathbf{M}(\boldsymbol{\theta}, \boldsymbol{\phi}) = \sin \theta \cos \phi \mathbf{e}_x + \sin \theta \sin \phi \mathbf{e}_y + \cos \theta \mathbf{e}_z$ unit vector where θ and ϕ are Eulerian angles with respect to the z and x axes, respectively, and \mathbf{e}_i is the unit vector in the i direction. The density function is normalized so that

$$\frac{1}{4\pi} \int_{\omega} \rho(\mathbf{M}(\Theta, \Phi)) d\omega = 1 \quad (1)$$

And the structure tensor is then given by

$$\mathbf{H} = \alpha_{ij} \mathbf{e}_i \mathbf{e}_j = \frac{1}{4\pi} \int_{\omega} \rho(M(\Theta, \Phi)) M(\Theta, \Phi) M(\Theta, \Phi) d\omega \quad (2)$$

The actin fiber tensor values, reported previously [44], for AR2 VSMCs were used for all experiments. The resulting actin fiber components were $\alpha_{xx} = 0.846$, $\alpha_{yy} = 0.126$, and, $\alpha_{zz} = 0.028$. Two forms of the strain energy density function were considered. The first [44] gives fiber stress as quadratic with stretch and is given by

$$W = \frac{\mu_m}{2} (\lambda_x^2 + \lambda_y^2 + \lambda_z^2 - 3) + \frac{C_f}{4} \left(\alpha_{xx} \left(\frac{\lambda_x}{\lambda_a} \right)^2 + \alpha_{yy} \left(\frac{\lambda_y}{\lambda_a} \right)^2 + \alpha_{zz} \left(\frac{\lambda_z}{\lambda_a} \right)^2 - 1 \right)^2 \quad (3)$$

In this text, this strain energy density function is denoted as the quadratic fiber model. The second gives fiber stress as linear with stretch and is given by

$$W = \frac{\mu_m}{2} (\lambda_x^2 + \lambda_y^2 + \lambda_z^2 - 3) + \frac{C_f}{4} \left(\alpha_{xx} \left(\frac{\lambda_x}{\lambda_a} \right) + \alpha_{yy} \left(\frac{\lambda_y}{\lambda_a} \right) + \alpha_{zz} \left(\frac{\lambda_z}{\lambda_a} \right) - 1 \right)^2 \quad (4)$$

In this text, this strain energy density function is denoted as the linear fiber model.

The parameters μ_m , C_f , λ_a were fit to the SED functions described by minimizing the sum of squared error (S) for all measured values of P_x and P_y , given by

$$S = \sum \left(\frac{P_j \text{ model} - P_j \text{ experiment}}{P_j \text{ experiment}} \right)^2 \quad (5)$$

where $j=x$ or y .

2.4 Results

2.4.1 F-Actin is realigned during large deformation stretching, but not plastically deformed.

We first asked whether large-deformation stretching acutely alters VSMC cytoskeleton organization. To measure actin organization, we stained F-actin with fluorescent SIR actin and analyzed the cytoskeletal structure as the cell underwent the large-deformation stretching protocol (Fig. 2.3(a)). When the cells were stretched axially, we observed an increase in the fraction of fibers aligned axially at large strains (Fig. 2.3(b)). Conversely, when the cells were stretched transversely, there was a decrease in fiber axial alignment with increasing stretch (Fig. 2.3(c)). The OOP was determined to quantify alignment during both loading and unloading. The OOP was consistent with the alignment distribution data for both axial loading (increasing with stretch) and transverse loading (decreasing with stretch). The OOP was nearly identical for loading and unloading suggesting that the actin fibers do not plastically deform or remodel during large-deformation loading (Fig. 2.3(d-e)).

2.4.2 VSMC stress-strain relationship is anisotropic.

Next, we asked how cell stress changes with large-deformation stretching. The C μ BS device was used to deform micropatterned VSMCs, while concurrently measuring the traction forces exerted by the cells on the underlying substrate (Fig. 2.4(a)). Consistent with previous studies of cells micropatterned with elongated architectures [44], [79], [80], we found that the tractions were largely concentrated at the axial ends of the cells and the corners of the micropatterns (Fig. 2.4(a)). Using the geometry and the traction forces we calculated mid-plane stresses (Fig. 2.4(b)).

The cells were stretched uni-axially in either the axial (parallel to the long axis of the cell) or transverse (parallel to the short axis of the cell) directions up to a stretch ratio of $\lambda=1.6$. When undergoing the axial stretch (Fig. 2.5(a)), the axial stress (P_x) increased with increasing stretch during loading and decreased during unloading (Fig. 2.5(b)). There was a lower initial transverse stress (P_y), which increased with loading and returned to the initial stress after unloading (Fig. 2.5(c)), but the increase was less than that seen in P_x . The stresses were greater during loading than unloading. This hysteresis is consistent with

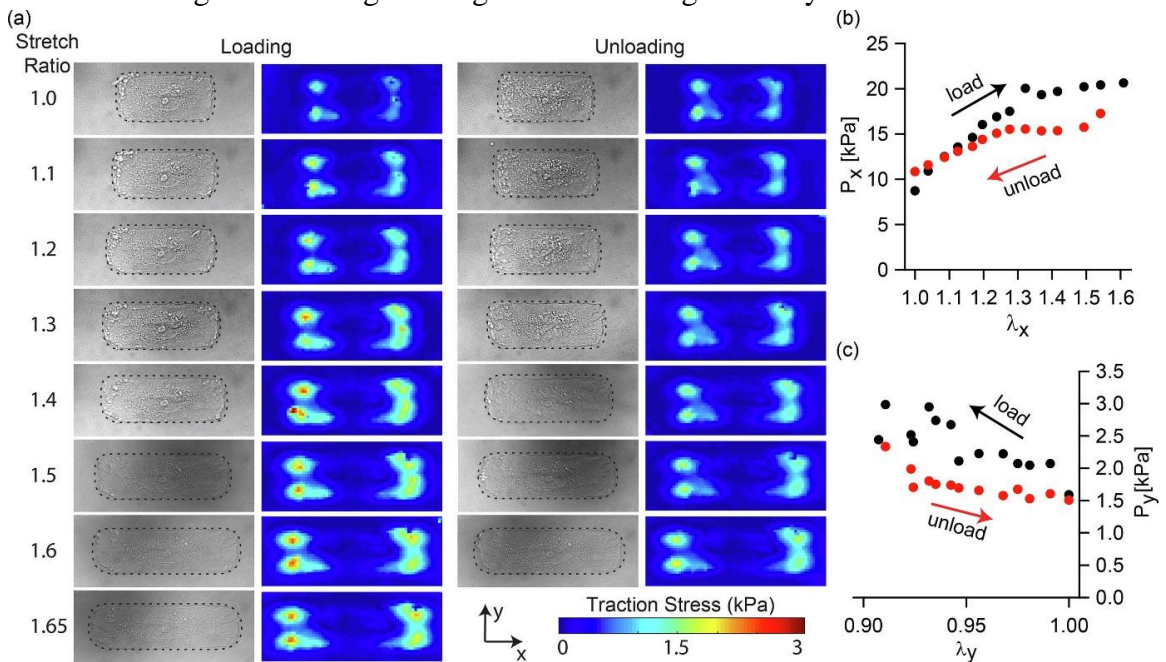


Figure 2.4. C μ BS microscopy for a representative VSMC.

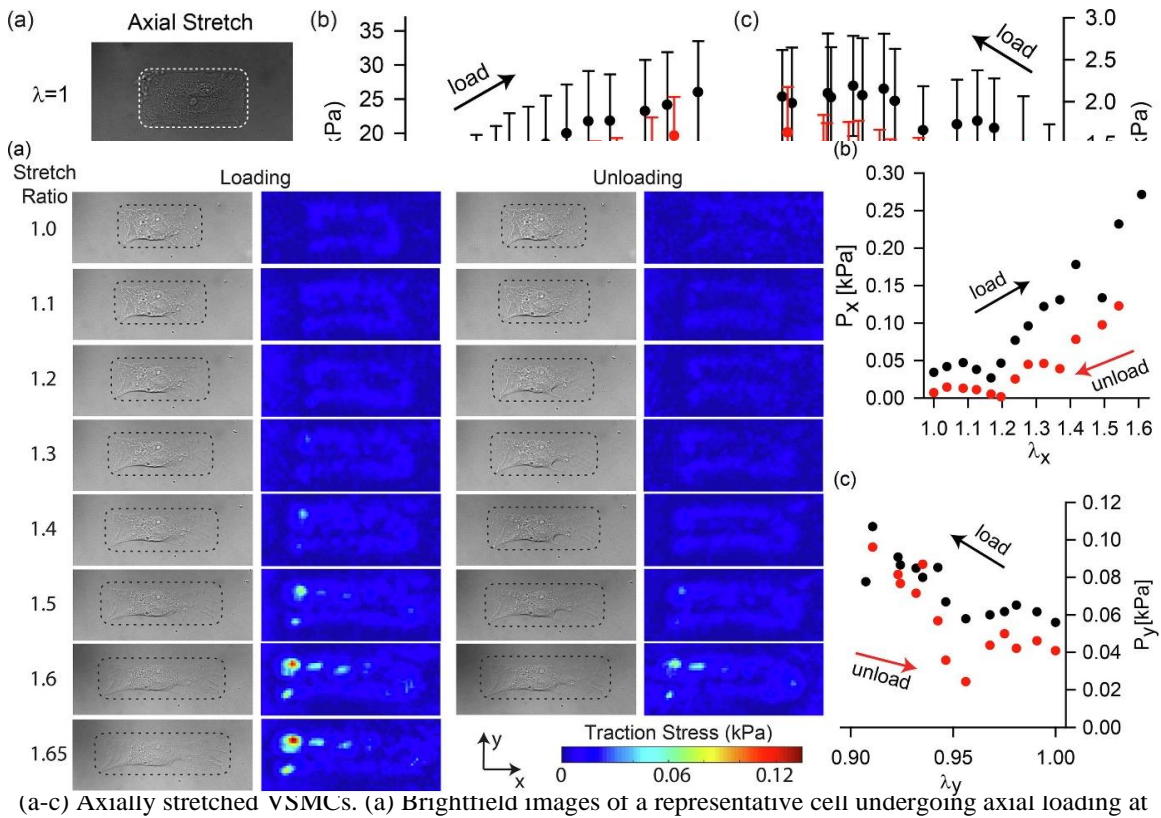
(a) Representative bright field images of a cell undergoing axial stretching (left column with dotted black line outlining the cell) and heat maps of the corresponding traction stress fields (right column). (b) Axial first Piola-Kirchhoff stress (P_x) for the representative cell during axial stretching during loading (black) and unloading (red). (c) Transverse first Piola-Kirchhoff stress (P_y) for the representative cell during axial stretching during loading (black) and unloading (red). cytoskeletal relaxation during elongation of the cell and contraction during shortening [71].

When undergoing transverse stretching (Fig. 2.5(d)), P_x increased during loading, but the increase was substantially less than was observed in axial loading (Fig. 2.5(e)). P_y also

increased with loading, though less than P_x , and both stresses decreased during unloading (Fig. 2.5(f)). Little hysteresis was observed during transverse stretching compared to axial stretching. These data demonstrate that VSMCs with in vivo-like architecture are anisotropic under large deformations.

2.4.3 VSMC stress anisotropy is primarily due to the actomyosin cytoskeleton.

To investigate potential contributions of actomyosin to VSMC stress, actomyosin contractility was blocked with ROCK inhibitor HA-1077 and the same stretching protocol



(a-c) AXIALLY stretched VSMCs. (a) Brightfield images of a representative cell undergoing axial loading at

Figure 2.6. CuBS microscopy for a representative passivated VSMC.

stretch ratios $\lambda=1$ and $\lambda=1.6$. (b-c) First Piola-Kirchhoff stresses, (b) P_x and (c) P_y , for VSMCs during (a) Representative bright field images of a cell undergoing axial stretching (left column with dotted black loading (black) and unloading (red) corresponding to measured stretch ratios ($n=9$). (d-f) Transversely line outlining the cell) and heat maps of the corresponding traction stress fields (right column). (b) Axial stretched VSMCs. (d) Brightfield images of a representative cell undergoing transverse loading at stretch ratios $\lambda=1$ and $\lambda=1.6$. (e-f) First Piola-Kirchhoff stresses, (e) P_x and (f) P_y , for VSMCs during transverse and unloading (red). (c) Transverse first Piola-Kirchhoff stress (P_y) for the representative cell during axial loading (black) and unloading (red) corresponding to measured stretch ratios ($n=8$). (all plots: mean +/- stretching during loading (black) and unloading (red). standard deviation)

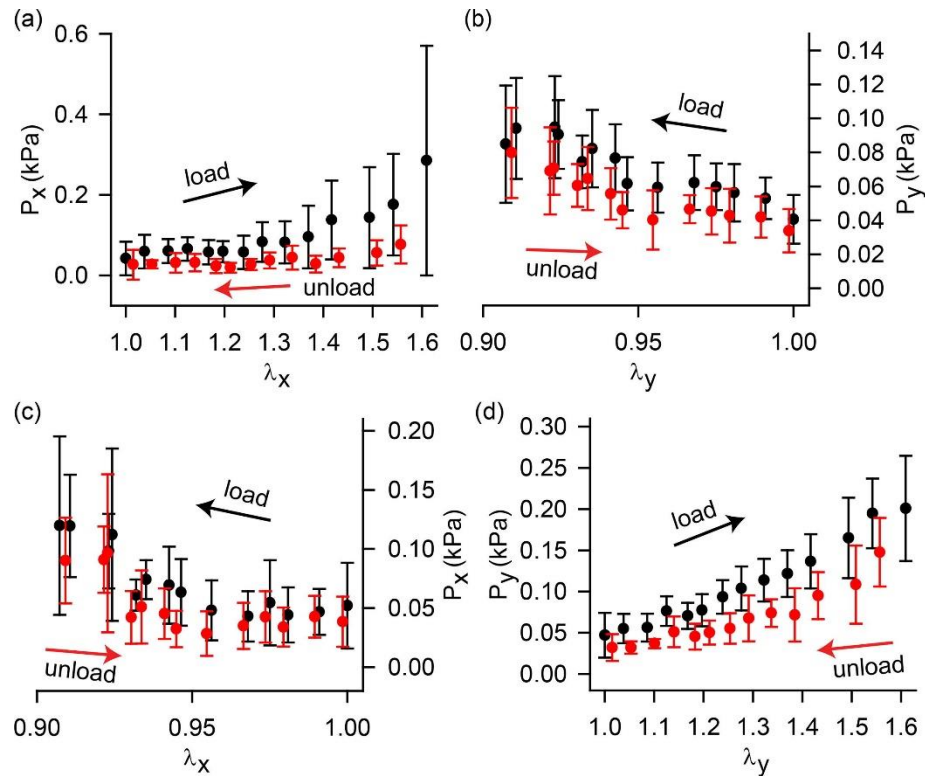


Figure 2.7. Strip biaxial tests of VSMCs with HA-1077 inhibited actomyosin complexes.

(a-b) Axially stretched VSMCs. First Piola-Kirchhoff stresses, (a) P_x and (b) P_y , during loading (black) and unloading (red) corresponding to measured stretch ratios ($n=11$). (c-d) Transversely stretched VSMCs. First Piola-Kirchhoff stresses, (c) P_x and (d) P_y , during loading (black) and unloading (red) corresponding to measured stretch ratios ($n=8$). (all plots: mean +/- standard deviation)

was applied (Fig. 2.6(a-c)). The passive cells exerted very low stress both before and during stretching, relative to the active cells (Fig. 2.7(a-d)). Passive cell stiffness was similarly low, relative to active cells. Notably, these passive data appear more isotropic than the active data. The stresses in the direction of stretch (P_x for axial and P_y for transverse) both increased slightly with stretch to approximately the same magnitude (Fig. 2.7(a and d)). The stresses in the off-stretch direction (P_y for axial and P_x for transverse) also increased slightly with stretch, though less than in the direction of stretch (Fig. 2.7(b and c)). These

data suggest that cytoskeletal actomyosin is the primary contributor to cell stiffness and material anisotropy under large deformation.

2.4.4 VSMC stress-strain behavior can be described by a linear fiber model.

Finally, we aimed to develop a model for characterizing the large-deformation mechanical properties of VSMCs by determining the strain-energy density function. In a previous study [44], we characterized the relatively small-strain (up to $\lambda=1.20$) strain energy density function of VSMCs, using a model that included a neo-Hookean bulk term and pre-strained actomyosin fibers whose stress varies quadratically with fiber strain (quadratic fiber model) (Eq. 4). That model, with the previously determined parameters

($\mu=0.5$ kPa, $\lambda_\alpha =0.8$, and $C_f=11.8$ kPa), fit our axial data well for small stretch ratios, but for stretch ratios greater than 1.20, the model diverged from our measured data (Fig. 2.8(a-d)). For this model, the sum of squared error S for all data, was 14.85.

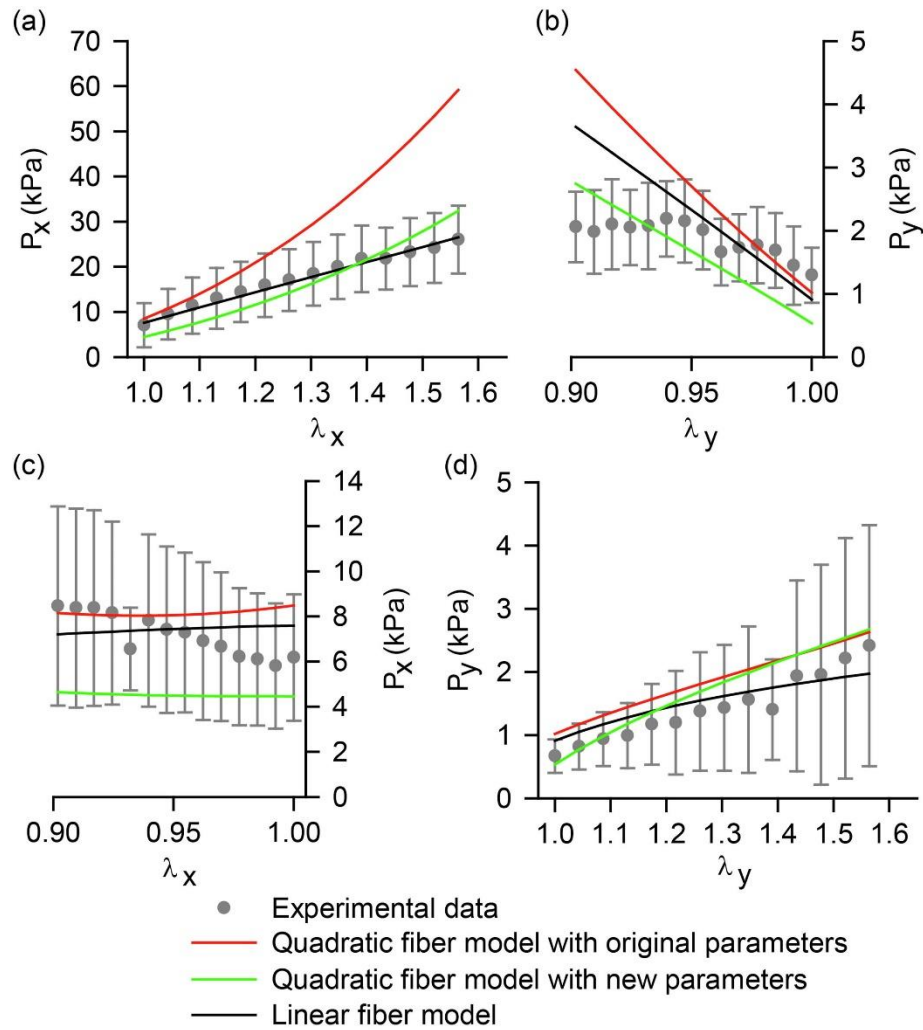


Figure 2.8. HGO model fits to experimental data.

(a-b) Axial stretch data and model predictions for (a) axial stress, P_x , and (b) transverse stress, P_y . (c-d) Transverse stretch data and model predictions for (c) axial stress, P_x , and (d) transverse stress, P_y . All plots: experimental data (grey, mean \pm standard deviation), quadratic fiber model with original parameters (red), quadratic fiber model with new parameters (green), linear fiber model (black).

Next, we fit the same quadratic fiber model to our large-deformation data with the best fit parameters ($\mu=1.4$ kPa, $\lambda_\alpha=0.8$, and $C_f=6$ kPa). The quadratic fiber model with the new parameters fit better ($S = 4.93$), but the concavity of the model curve did not replicate the measured data.

Finally, we refined the model so that the fiber stress was linearly related to fiber stretch (linear fiber model) (Eq. 5). This model ($\mu=0.8$ kPa, $\lambda_\alpha=0.8$, and $C_f=59.6$ kPa) fit the data significantly better than the quadratic fiber model ($S = 3.07$). These data demonstrate that the mechanical properties of single VSMCs with in vivo-like architecture deformed at relatively slow strain rates are linear at large deformations.

2.5 Discussion

A standard method for quantifying the mechanical properties of soft tissues is to perform biaxial stretching experiments [81]–[83]. These tests are typically done to large strains so that the full mechanical properties and nonlinearity of the tissue can be examined [55], [84]. These tissue properties are needed to develop computational models of tissue growth and remodeling [57] and disease progression [85], and to simulate surgical intervention [86], [87]. A common modeling technique used in these simulations on the tissue-scale is the constrained mixture model, which requires the mechanical properties of each component to be described, including VSMCs. In addition, VSMC loading influences VSMC function, suggesting that cellular stress is a key contributor to tissue maintenance [88]. So, here we expand our previous study [44] to examine large deformation mechanical properties of VSMCs. Our large-deformation C μ BS measurements demonstrated three key characteristics of VSMCs with native-like architecture: they are highly anisotropic, display significant hysteresis, and are surprisingly linear even when exposed to large strains.

We found that VSMCs with an in vivo-like elongated architecture have anisotropic cytoskeletal organization and mechanical properties. In vivo, many cells have highly organized and anisotropic structure [18], [59]. This in vivo anisotropy has been replicated in vitro using micropatterning in a wide range of cell types [14], [72], [89], [90] to demonstrate the role of architecture in cellular functions such as migration [89], [91], contractility [15], [42], [73], and focal adhesion formation [92]. This anisotropic cytoskeletal architecture also influences the location of cell generated tractions. In cells with elongated geometries, thicker bundles of actin run primarily parallel to periphery of the cell and corner-to-corner through the middle of the cell [93], [94]. As a result, the cell tractions are largely concentrated at the axial ends and corners of the micropatterned VSMCs, as seen in previous studies of micropatterned cells [44], [79], [80]. This nonuniform traction distribution results in axial stresses (P_x) being much larger than transverse stress (P_y), even prior to any stretching. When the cell is stretched, the degree of cytoskeletal anisotropy increases with increasing stretch, as the fibers reorient with greater alignment. These findings are consistent with studies in reconstituted actomyosin networks [95], as well as in other non-patterned cells [96], [97].

In this study, we focused on the influence of actomyosin architecture on VSMC mechanics. It should be noted that other cytoskeletal elements could contribute to the observed mechanical behavior. In our small strain studies, we found that depolymerization of microtubules did not significantly alter small strain VSMC mechanics [44]. However, intermediate filaments play key roles in maintaining the mechanical integrity of the cell and protecting cells from mechanical stress [98]–[101] and cannot be fully decoupled from the actomyosin mechanics via the methods used here. We found that mechanical anisotropy

of micropatterned VSMCs strongly correlates with actomyosin architecture and inhibition of actomyosin contractility eliminated nearly all tension within the cell. Interestingly, in cells in which contraction was inhibited, the mechanical properties were isotropic, further supporting the conclusion that cytoskeletal organization is a primary mediator of mechanical anisotropy.

Cellular hysteresis, measured by atomic force microscopy, has been observed in embryonic stem cells [102], skeletal muscle cells [63], and neurons [103]. Here, we observed hysteresis in our loading-unloading cell stress data. Notably, even with large deformations, we did not observe any structural reorganization of the cytoskeleton, suggesting that we are not plastically deforming the cell. The observed hysteresis may be due to cell viscoelasticity [104], [105], active contraction and relaxation [71], or remodeling [66]. For the uni-axial properties analyzed in this study, we characterized only the loading portion of the stress-strain curves, and ignored the viscoelastic or contractile effects on hysteresis.

In a previous study, we used C μ BS to characterize a strain energy density function for relatively small deformations [44]. Here we expanded that work to measure and characterize large deformations, up to stretch ratios of $\lambda=1.6$. Under the large deformation conditions reported here, the previously described quadratic fiber model did not fit the data, necessitating the development of a new model. The linear fiber model fit the data better over the whole range of stretch ratios. This is notably different from models of the whole artery which are nonlinear and strain-stiffening [55], consistent with models of extracellular matrix components such as collagen networks [106], [107]. These data suggest that VSMCs, unlike whole arteries and collagen, do not display non-linear

mechanical properties even at large strains and that linear models can provide a good approximation of their mechanical properties.

While the linear fiber model best fits our experimental data, it is clear that neither the quadratic nor the linear model exactly replicates the experiments. None of the elastic models presented can replicate the hysteresis measured experimentally. And, even our best model fails to replicate the stresses perpendicular to the direction of stretch (see Fig 8 b, c). This is most likely because these passive models do not consider dynamic cellular processes that are occurring during stretching. In a previous study, we found that incorporating active Hill-type contraction and relaxation of actomyosin fibers results in a better model fit with small-strain $C\mu$ BS experiments [71]. For example, that model predicts that axial fibers will contract during transverse stretching so that P_x increases. This phenomenon was observed experimentally here, but not captured by our passive models (see Fig 8c). Other models that consider cytoskeletal dynamics [108] and focal adhesion remodeling [109] might also better replicate the experiments. These dynamic processes are likely of particular importance when describing high-strain rate-dependent material properties of the cells. Here, we used relatively low strain rates to approximate the quasi-static deformation appropriate for measuring the strain energy density function. However, in vivo strain rates for arteries are reported between 0.25-3%/s [110], [111], suggesting that quasi-static properties may not be sufficient in all clinically relevant models. Further development of dynamic models and further studies of strain rate dependent cellular properties are both warranted to develop a better understanding of vascular cell mechanics.

These results have important implications in modeling of mechanobiology. VSMCs are known to alter their function in response to chronic deformation [112]–[114] and

altered extracellular material properties [41], [62]. This altered function can subsequently lead to VSMC induced remodeling of extracellular mechanics [115], [116]. Models of mechano-adaptation often assume cell stress is a primary driver of growth and remodeling phenomena. The results presented here are a key step toward connecting measurable cell stresses to these models.

Chapter 3. Anisotropic Mechanics of Vascular Smooth Muscle Cells Exposed to Dynamic Loads

This chapter contains material published in the Journal of Biomechanical Engineering and is reproduced with permission from reference [117]. Rothermel, T.M., Franczek, I.A. and Alford, P.W., 2021. Anisotropic mechanics of vascular smooth muscle cells exposed to dynamic loads. *Journal of biomechanical engineering*, 143(12), p.121007.

3.1 Summary

Vascular smooth muscle cells (VSMCs) are the most prevalent cells in the arterial wall. In vivo, arteries are exposed to dynamic biaxial loads, thus when characterizing VSMC mechanics it is important to determine their anisotropic and time-dependent mechanical properties. Here, we use cellular microbiaxial stretching (C μ BS) to apply complex deformations to single micropatterned VSMCs and measure the resulting changes in cell stress. Previously, C μ BS has been used to measure VSMC mechanical properties in response to extensional strain. Here, we measure changes in cell stress in response to both extension and compression. Additionally, we measure immediate temporal changes in stress in response to cyclically applied deformations. We find that the VSMCs display clear hysteresis when incrementally stretched and compressed and demonstrate cycle-dependent stress-relaxation when exposed to cyclic step change extension and compression. Finally, we demonstrate that a Hill-type active fiber model is capable of replicating all observed hysteresis and cycle-dependent stress-relaxation, suggesting that the temporal stress-strain behavior of the cell is regulated by acto-myosin contraction and relaxation, rather than

passive viscoelasticity. This study improves upon previous studies of cellular mechanical properties by considering cellular architecture and more complex deformations when measuring the time-dependent mechanical properties of VSMCs. These findings have important implications for modeling in mechanobiology as VSMCs are mechanosensitive and actively respond to changes in their mechanical environment to maintain vascular function.

3.2 Introduction

Arteries are exposed to constant mechanical loading, experiencing cyclic strains of 2-15% per cardiac cycle as a result of normal blood pressure [53], [60], [118], with even larger strains possible in pathologies such as hypertension. In this dynamic mechanical environment, vascular smooth muscle cells (VSMCs), the most prevalent cell type in the arterial wall, are responsible for maintaining physiological function of the vessels via vasoconstriction and dilation [47]. Mechanical stimuli such as extracellular substrate stiffness and applied strains influence VSMC functions such as protein synthesis, focal adhesion formation, and cytoskeletal organization [41], [61], [62], [119], [120]. Cyclic loading is of particular relevance to VSMCs because of the pulsatile nature of in vivo loading. Cyclic stretching has been shown to affect alignment, migration, and protein synthesis in VSMCs [112], [114], [121]–[123]. Because VSMCs are sensitive to their mechanical environment and imposed mechanical loads influence cellular behavior, it is important that the response of VSMCs to mechanical loads is fully characterized.

Cells have relatively complex, temporally-dynamic mechanical properties and are typically characterized as viscoelastic [64], [105], [124]–[131] because they display hysteresis [63], [132], creep [131], [133], [134], and stress relaxation [135]–[137]

behaviors. Previous studies have utilized techniques such as magnetic bead cytometry [69], [70], [138] and atomic force microscopy [67], [68], [139] to investigate time dependent cellular mechanical properties. These methods are best for describing linear, isotropic mechanical properties and do not account for the structural anisotropy of the cell. In vivo, VSMCs are wrapped circumferentially around the blood vessel and have an elongated spindle-shaped architecture [59]. In VSMCs with this elongated architecture, the cytoskeleton is highly anisotropic, with acto-myosin stress fibers aligned parallel to the long axis of the cell. Thus, to characterize VSMC mechanics, it is important to determine their anisotropic properties.

We recently developed cellular microbiaxial stretching (C μ BS) as a tool to measure single-cell mechanical properties under complex loads while accounting for structural anisotropy in micropatterned cells [44]. In prior studies, we have measured the strain energy density function of VSMCs under relatively small [44] and large strains [45]. Additionally, we found that VSMCs with in vivo like geometry display direction-dependent hysteresis, which can be described using a Hill-type active fiber model [71]. Here, we build on these previous studies, using C μ BS to measure the anisotropic mechanical properties of VSMCs exposed to incremental and cyclic loads and model the stress-strain behavior using a Hill-type active fiber model. We find that VSMCs are anisotropic in both tension and compression, display hysteresis when stretched and compressed, and undergo stress relaxation in response to cyclic step changes in strain. We further find that the Hill-type active fiber model is able to recapitulate all of these phenomena. These results have important implications for understanding cell mechanical function in vascular tissues.

3.3 Methods

3.3.1 Cellular Microbiaxial Stretching.

The cellular microbiaxial stretching (C μ BS) device (Fig. 3.1A) is a custom-built, microscope mounted device consisting of four independently controlled linear actuators used to simultaneously apply controlled strains to and image micropatterned cells. C μ BS substrates were prepared as previously described [44]. Briefly, an elastomeric membrane was clamped between custom metal brackets. Substrates for tension experiments were placed under slight tension. Substrates for compression experiments were under an additional 15% strain. A fluorescent bead doped polyacrylamide (PA) gel with a 13.5 kPa Young's modulus was bonded to the elastomeric membrane. The PA gel was micropatterned with 127 μm x 32 μm fibronectin rectangles for cell adhesion, using standard microcontact printing techniques (Fig. 3.1B). Gel moduli were measured by performing uniaxial testing using an Instron biaxial stretcher (Tissue Mechanics Lab, University of Minnesota) on dog-bone shaped gels (\sim 5 mm width, \sim 5 mm thick, \sim 50 mm length).

3.3.2 Cell Culture.

Human umbilical artery vascular smooth muscle cells (VSMCs) (Lonza) were obtained at passage 3 and cultured in VSMC growth media containing Medium 199 (GenDEPOT, Baker, TX) supplemented with 10% fetal bovine serum (Gibco, Grand Island, NY), 10 mM HEPES (Gibco), 3.5 g L $^{-1}$ glucose (Sigma-Aldrich, St. Louis, MO), 2 mg L $^{-1}$ vitamin B12 (Sigma-Aldrich), 50 U mL $^{-1}$ penicillin–streptomycin (Gibco), 1 \times MEM non-essential amino acids (Gibco), and 2 mM L-glutamine (Gibco). Cells between passages 5-7 were used for experiments and were seeded onto prepared micropatterned

substrates at a density of ~25 cells per mm². Cells were allowed to adhere to the substrates for 24 hours in an incubator and then serum starved for 24 hours to induce a contractile

phenotype prior to performing experiments. Experiments were performed at 37 °C and 5% CO₂ to preserve cell viability.

3.3.3 Stretching Protocols.

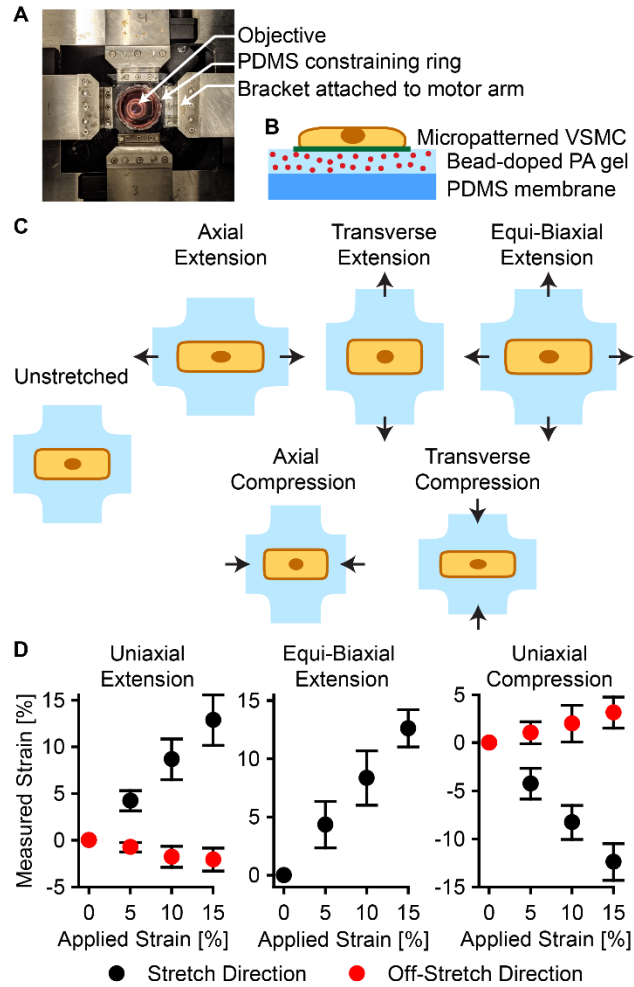


Figure 3.1. Cellular microbiaxial stretcher.

(a) Image of C_μBS device mounted in the microscope. (b) Schematic of VSMC micropatterned on PA gel.

(c) Schematics of the five different loads applied to the cell using C_μBS: axial extension, transverse extension, equi-biaxial extension, axial compression, and transverse compression. (d) Comparison between the applied grip strain and actual measured cell strain using C_μBS for uniaxial extension (n = 18), equi-biaxial extension (n = 10), and uniaxial compression (n = 27). Error bars: standard deviation.

For the experiments presented here, two stretching protocols were used: an incremental stretching protocol and a cyclic step-change stretching protocol. Experimental protocols were performed such that cells were either extended (tension) or shortened (compression) in the direction of stretch. Tensile deformations were applied axially (membrane stretched parallel to the long axis of the cell and unstretched parallel to the short axis), transversely (membrane stretched parallel to the short axis of the cell and unstretched parallel to the long axis), or equi-biaxially (stretch applied in both directions simultaneously). Compressive deformations were applied axially or transversely (Fig. 3.1C). Due to the constraint of ring containing cell culture media, end-to-end membrane strain was not identical to the strain applied to the cell. To measure cell strain, the membrane was stretched over a range of stretch ratios (λ) of 1-1.15 and individual cells were imaged using brightfield microscopy. Cell stretch ratios were determined from the initial and deformed geometries of the cells. Applied and measured linear strains were calculated as $\epsilon = \lambda - 1$ (Fig. 3.1D). Measured cell stretch ratios and strains were used for all calculations and are reported in all figures.

Incremental Stretching Protocol. An initial stretch to the maximum stretch ratio of $\lambda = 1.15$ for extension or $\lambda = 0.85$ for compression was performed to locate cell positions at each deformation and eliminate any slippage in the membrane followed by the loading and unloading stretches for image acquisition. Deformations were applied in a stepwise fashion in increments of $\Delta\lambda = \pm 0.05$ at a rate of 0.005 s^{-1} until a maximum of $\lambda = 1.15$ applied stretch ratio for extension and $\lambda = 0.85$ applied stretch ratio for compression. The applied strains were then removed in increments of $\Delta\lambda = \pm 0.05$ until the cell returned to the unstretched configuration $\lambda = 1.00$ (Fig. 3.2A-B). At each increment, the strain was held

for two minutes to acquire bright field images of the cell and the cell-deformed fluorescent bead layer at the cell-gel interface. After stretching, the cells were lysed using a 0.1% sodium dodecyl sulfate (SDS) solution. Cell-free images of the fluorescent bead layer were then acquired at each increment.

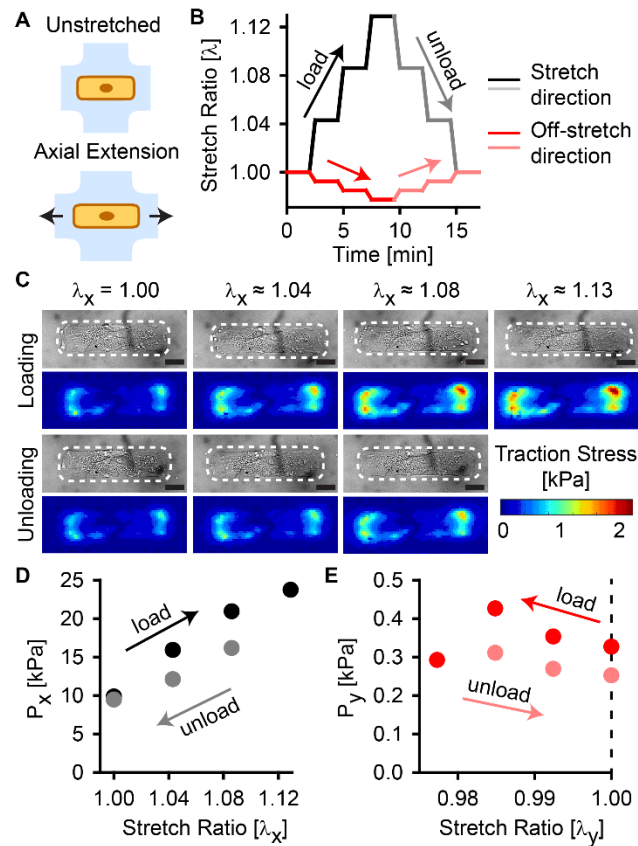


Figure 3.2. Incremental Stretching Protocol.

(a) Schematic of a micropatterned cell undergoing axial extension. (b) The incremental changes in the measured stretch ratio of the cell over time. (c) Bright field images and corresponding traction stress heat maps for a representative cell at each deformation. Scale bar: 15 μm . (d) First Piola–Kirchhoff stress in the axial direction during loading and unloading for the representative cell. (e) First Piola–Kirchhoff stress in the transverse direction during loading and unloading for the representative cell.

Cyclic Step-Change Stretching Protocol. An initial stretch to the maximum applied stretch ratio of $\lambda = 1.15$ for extension or $\lambda = 0.85$ for compression was performed to locate the cell position when in the deformed configuration and eliminate any slippage in the membrane followed by the cyclic stretches for image acquisition. After the priming stretch, a bright field image of the cell and an image of the fluorescent bead layer were taken and used as the initial time point. Deformations were then applied in a square-waveform stretch with peaks of $\lambda = 1.00$ and $\lambda = 1.15$ for extension or $\lambda = 0.85$ for compression. Strains were applied at a rate of 0.005 s^{-1} and held for three minutes at each deformation. This was repeated for a total of four cycles (Fig 3A-B). During each stretch, the fluorescent bead layer was imaged at 1 Hz for the duration of the three minute hold and a single bright field image of the cell was collected. After four cycles, cells were lysed with 0.1% SDS solution and cell-free images of the bead layer were acquired.

3.3.4 Cell Stress Analysis.

The cell-induced bead displacement was calculated using a particle image velocimetry (PIV) algorithm and the cell-attached and cell-free fluorescent bead layer images. An unconstrained Fourier transform traction cytometry algorithm [74] (regularization factor: $1\text{E-}9$, Poisson's ratio: 0.5) was used to form traction stress vector fields from the calculated bead displacements. Substrate traction force vectors were defined by $\mathbf{T}^n a^n$ where $\mathbf{T}^n = T_x^n \mathbf{e}_x + T_y^n \mathbf{e}_y$ is the traction vector acting on area a^n and \mathbf{e}_i is the unit vector in the i direction. Substrate tractions (Fig. 3.2C, 3.3C) are balanced with cell forces (\mathbf{f}^n) at the interface of the cell and the PA gel, such that $\mathbf{f}^n = f_x^n \mathbf{e}_x + f_y^n \mathbf{e}_y =$

$-T_x^n a^n \mathbf{e}_x + -T_y^n a^n \mathbf{e}_y$. Forces oriented away from the center of the cell were denoted as tensile (positive). The total tensile force $2f_x = \sum_n f_x^n r_x^n / |r_x^n|$ and $2f_y = \sum_n f_y^n r_y^n / |r_y^n|$,

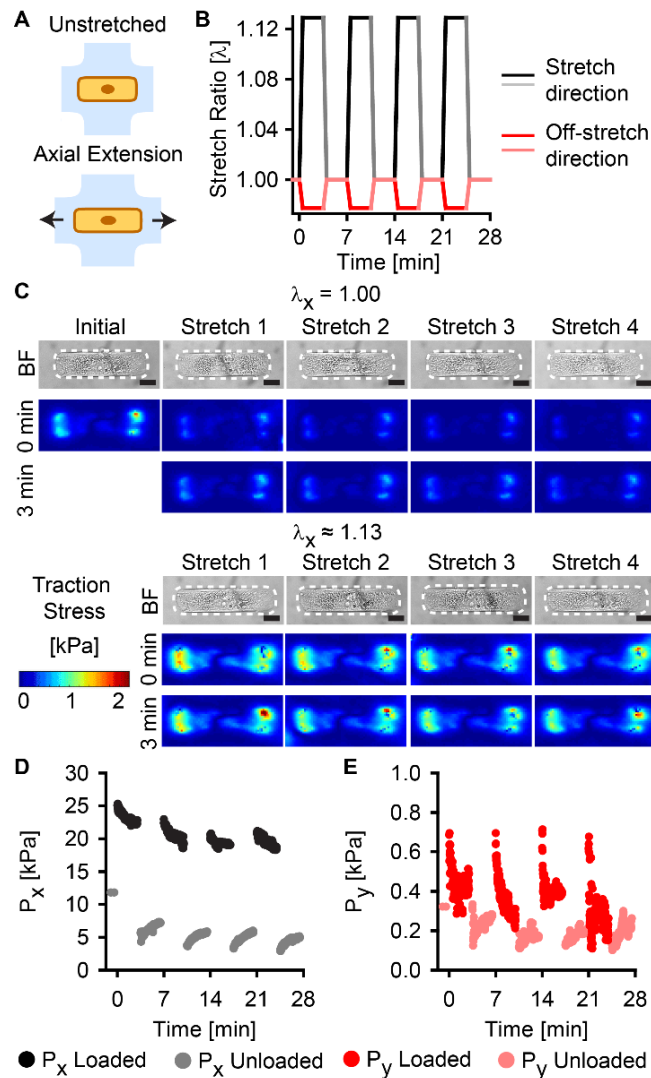


Figure 3.3. Cyclic stretch protocol.

(a) Schematic of a micropatterned cell undergoing axial extension. (b) Stretching protocol for cyclic step change stretching showing step changes in the applied stretch ratio between from the unloaded configuration ($\lambda = 1.00$) and the loaded configuration ($\lambda = 1.15$) held for three minutes at each position. (c) Bright field images of a representative cell at each strain for each cycle and corresponding traction stress heat maps at the beginning and end of each stretch. Scale bar: $15 \mu\text{m}$. (d) First Piola–Kirchhoff stress in the long axis of the cell (P_x) for the representative cell during the axial extension cyclic step change protocol. (e) First Piola–Kirchhoff stress in the short axis of the cell (P_y) for the representative cell during the axial extension cyclic step change protocol.

where $\mathbf{r}_n = r_x^n \mathbf{e}_x + r_y^n \mathbf{e}_y$ is the vector describing the location of n with respect to the center of the cell. The first Piola-Kirchhoff (PK1) stresses were calculated at the mid-plane of the cell using the total tensile force and the undeformed cross-sectional area of the cell. The PK1 stress in the direction of the long axis of the cell is represented by $P_x = (f_x/A_x)$ and the PK1 stress parallel to the short axis of the cell is represented by $P_y = (f_y/A_y)$ (Fig. 3.2D-E, 3.3D-E). The cell cross-sectional areas were measured in a previous study to be $A_x = 78 \mu\text{m}^2$ and $A_y = 278 \mu\text{m}^2$ [44].

3.3.5 Hill-Type Active Fiber Model.

The cell was assumed to undergo isochoric planar biaxial deformation (no shear). The deformation tensor $\mathbf{F} = \text{diag}[\lambda_x, \lambda_y, \lambda_z]$ was measured from the observed deformation of the cell, where λ_i was the stretch ratio in the i direction (x: parallel to the long axis of the cell, y: parallel to the short axis of the cell, and z: normal to the surface of the gel). Previous studies [66] found that the volume of micropatterned VSMCs was unchanged when stretched, so we assumed $\lambda_z = (\lambda_x \lambda_y)^{-1}$.

The cell was modeled as discrete one-dimensional, contractile acto-myosin fibers within an isotropic matrix. When the cell was deformed according to \mathbf{F} , each fiber within the cell is also deformed (λ_f) according to its orientation within the matrix such that

$$\lambda_f^2 = \lambda_x^2 \cos^2 \theta + \lambda_y^2 \sin^2 \theta \quad [1]$$

The isotropic matrix was treated as neo-Hookean such that the strain energy density function was described as

$$W_b = \frac{\mu}{2} (I_1 - 3), \quad [2]$$

where $I_1 = \lambda_x^2 + \lambda_y^2 + \lambda_z^2$ is the first strain invariant and μ is the shear modulus of the matrix. For a discrete number of fibers (n) the constitutive equation for the strain energy density for the fiber matrix is

$$W_f = \frac{1}{n} \sum_{i=1}^n \frac{C_f}{2} \left(\left(\frac{\lambda_{fi}}{\lambda_{ai}} \right)^2 - 1 \right)^2, \quad [3]$$

where C_f is a stiffness parameter and λ_{fi} and λ_{ai} are the fiber stretch ratio and active stretch ratio of the i^{th} fiber, respectively. Thus, the total strain energy density for the cell is given as

$$W = W_b + W_f, \quad [4]$$

Active contraction of the acto-myosin fibers using the Hill equation for muscular contraction [140] as we have previously described [71], given by

$$\frac{\dot{\lambda}_a}{\lambda_a} = \frac{b(P_f - P_o)}{\lambda_f(P_f + a_o)}, \quad [5]$$

where P_f is the First Piola-Kirchhoff stress in the direction of fiber orientation, λ_f is the fiber stretch ratio, P_o is the fiber stress at the beginning of the experiment when the cell is maintaining homeostatic stretch, and a_o and b are constants.

Solution Method. The model was fit to the extension data from the incremental stretching protocol. A random family of 200 fibers was generated with a von Mises distribution ($\kappa = 32.46$) [71] consistent with what has been measured in VSMCs micropatterned in an elongated architecture. Time for the incremental stretching experiments was set to 14 minutes. Parameters were fit to the extension incremental stretching data via least-squares fitting of the experimentally-measured stresses (both P_x

and P_y for axial, transverse and equi-biaxial extension) to the mean model predicted stresses during the holding period at each increment. The parameter range that was considered was $\mu = 0.5 - 11.5 \text{ kPa}$, $C_f = 0.25 - 5.75 \text{ kPa}$, $\lambda_{a0} = 0.6 - 0.75$, $a_0 = 0.5 - 8 \text{ kPa}$, and $b = 0.005 - 0.05$. The values for the stretch ratios were taken from a linear fitting of the measured stretch ratio of the cell. Stretch ratios were $\lambda_{stretch} = [1.000, 1.043, 1.086, 1.129]$ and $\lambda_{off-stretch} = [1.000, 0.992, 0.985, 0.977]$ for uniaxial extension, $\lambda_{stretch} = [1.000, 1.042, 1.084, 1.126]$ for equi-biaxial extension, and $\lambda_{stretch} = [1.000, 0.958, 0.917, 0.875]$ and $\lambda_{off-stretch} = [1.000, 1.010, 1.021, 1.031]$ for uniaxial compression. After parameter optimization, PK1 stresses for all incremental stretching protocols were determined. Additionally, the same parameters from the incremental extension fitting were used to calculate the PK1 stress over time during the cyclic step-change loading protocol.

3.4 Results

3.4.1 VSMCs with elongated geometry are anisotropic and demonstrate hysteresis under both tensile and compressive loading.

In previous studies, we found that VSMCs have anisotropic mechanical properties and demonstrate stretch-dependent hysteresis under tensile strains [71]. Here, we first asked how cell stress changes under complex loading conditions including compressive strains. We applied incremental step changes in stretch ratio ($\Delta\lambda = \pm 0.05$ per step). Applied strains were either extensional or compressive and aligned parallel to the long axis of the cell (axial) (Fig. 3.4A(i-ii), 3.4B(i-ii)), the short axis of the cell (transverse) (Fig. 3.4C(i-ii), 3.4D(i-ii)), or both axes (equi-biaxial) (Fig. 3.4E(i-ii)).

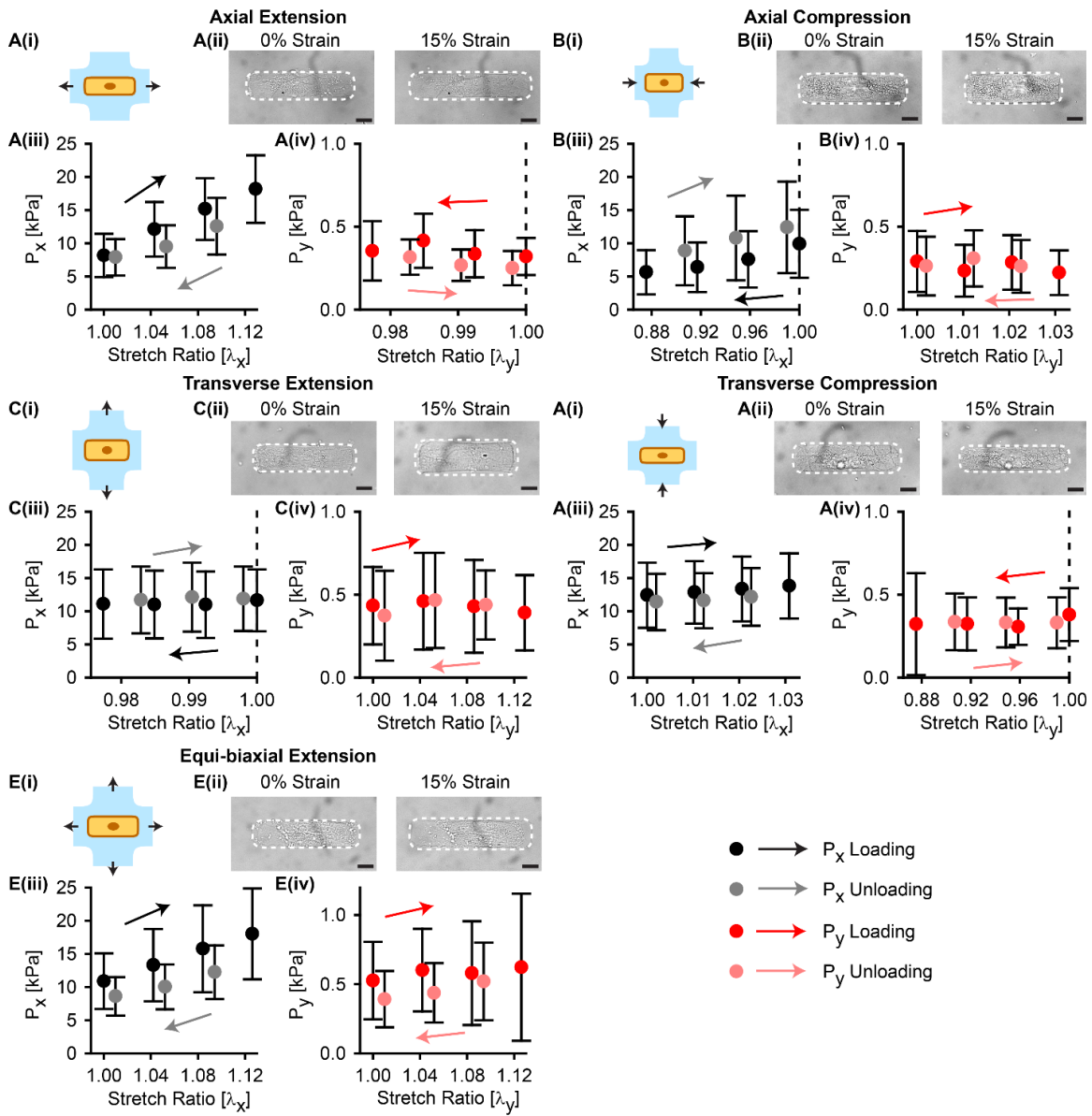


Figure 3.4. Incremental Stretching C μ BS Experiments.

Experimental results for cells under (a) axial extension ($n = 9$), (b) axial compression ($n = 15$), (c) transverse extension ($n = 9$), (d) transverse compression ($n = 12$), and (e) equi-biaxial extension ($n = 8$). For all panels, (i) schematic of the stretch, (ii) Bright field images of micropatterned VSMC at 0% and 15% applied strain, (iii) First Piola–Kirchhoff stress in the long axis of the cell (P_x) during loading and unloading, (iv) First Piola–Kirchhoff stress in the short axis of the cell (P_y) for loading and unloading. Error

bars: standard deviation. Scale bar: 15 μm .

Note: due to the ring adhered to the membrane to hold the media, the uniaxial deformations are not purely strip biaxial (see Fig. 3.1A, 3.1D). This is reflected in the results and analyses. Using C μ BS, we measured the cell stress at each increment of deformation. Prior to stretch, stress was greater parallel to the long axis of the cell (axial stress, P_x) than parallel to the short axis of the cell (transverse stress, P_y) consistent with previous studies [44], [45].

Axial Stretching. In cells undergoing the axial extension, P_x (Fig. 3.4A(iii)) increased during loading as the cell was stretched and decreased during unloading. Hysteresis was observed as P_x was greater during loading than unloading. P_y (Fig. 3.4A(iv)) increased slightly during loading though the change stress was relatively small compared to P_x . When undergoing axial compression, P_x (Fig. 3.4B(iii)) decreased during loading as the cell was compressed and increased during unloading, and hysteresis was observed. P_y (Fig. 3.4B(iv)) also decreased slightly during axial compression, though less than the change in P_x .

Transverse Stretching. In cells undergoing transverse extension, P_x (Fig. 3.4C(iii)) decreased slightly as the cell was stretched and was slightly greater during unloading than loading, and P_y (Fig. 3.4C(iv)) remained relatively unchanged during loading and unloading. Under transverse compression, P_x (Fig. 3.4D(iii)) increased slightly as the cell was compressed and then decreased again with unloading and stresses were slightly greater during loading than unloading. P_y (Fig. 3.4D(iv)) remained relatively unchanged during compression. Overall, stresses during transverse stretching changed relatively little

compared to axial stretching, demonstrating that the micropatterned VSMCs are highly anisotropic.

Equi-Biaxial Stretching. In cells undergoing equi-biaxial extension, P_x and P_y (Fig. 3.4E(iii-iv)) increased with stretch and decreased when unloaded and there was hysteresis

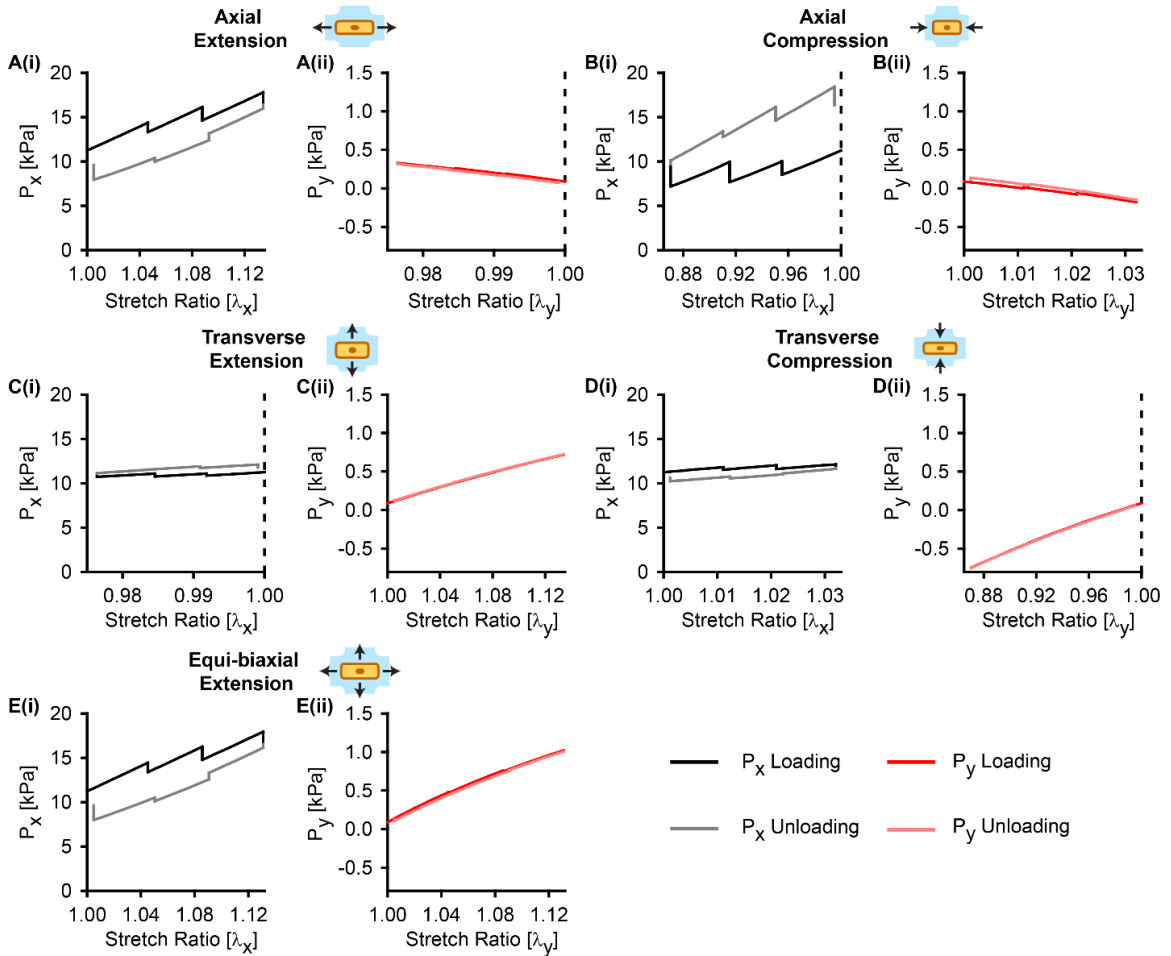


Figure 3.5. Hill-type active fiber model fit to incremental stretching results.

Hill-type active fiber model (a) axial extension, (b) axial compression, (c) transverse extension, (d) transverse compression, and (e) equi-biaxial extension. For each panel, (i): PK1 stress in the long axis of the cell (P_x) during loading and unloading and (ii) PK1 stress in the short axis of the cell (P_y) during loading and unloading.

where stress was greater during loading than unloading. Consistent with the anisotropic results above, P_x increased more than did P_y when stretched.

3.4.2 A Hill-type active fiber model recapitulates anisotropic mechanical behavior of VSMCS under complex loads.

We have previously used this Hill-type active fiber model to describe VSMC anisotropic hysteresis under extension. Here, we fit the model using the extension data from the incremental stretching protocol yielding the following parameters: $\mu = 1.5kPa$, $C_f = 3.75kPa$, $\lambda_{a0} = 0.74$, $b = 0.02$, and $a_0 = 5.5kPa$. The model with these parameters was able to robustly recapitulate the anisotropic mechanical behavior of VSMCs under the experimental stretching protocol for both tension and compression as well as the observed hysteresis (Fig. 3.5A-E).

3.4.3 VSMCs demonstrate temporally dynamic stress-strain behavior.

Next, we measured how VSMCs adapt their stresses over a short time in response to cyclically applied step changes in strain. The cyclic step change loading protocol applied a stretch ratio of $\lambda = 1.15$ for extension or $\lambda = 0.85$ for compression at a rate of 0.005 s^{-1} , maintaining the deformation for three minutes, then returning to the original unstretched configuration for four cycles. In all experiments, VSMCs demonstrated stress relaxation during each cycle, and cell stress varied with each cycle.

Axial Stretching. When the cell was axially extended, we observed stress relaxation in P_x (Fig. 3.6A(i)) both after the stretch was applied and after the cell was returned to the unstretched position. This stress relaxation was repeated for each stretching cycle, but P_x decreased with each cycle indicating a cycle-dependency to the cellular response to this

strain pattern. P_Y (Fig. 3.6A(ii)) demonstrated a similar stress relaxation response to stretching as seen in P_x , though to a lesser magnitude. When the cell was axially compressed using cyclic step change loading, the stress relaxation was also observed. However, in compression, P_x (Fig. 3.6B(i)) and P_y (Fig. 3.6B(ii)) increased with each cycle.

Transverse stretching. As with axial stretching, when transverse cyclic step change stretching was applied, we observed stress relaxation during each cycle. And, consistent with the anisotropic properties measured using incremental loading, we observed less change in cell stress for transverse loading, compared to axial. For transverse extension, P_x

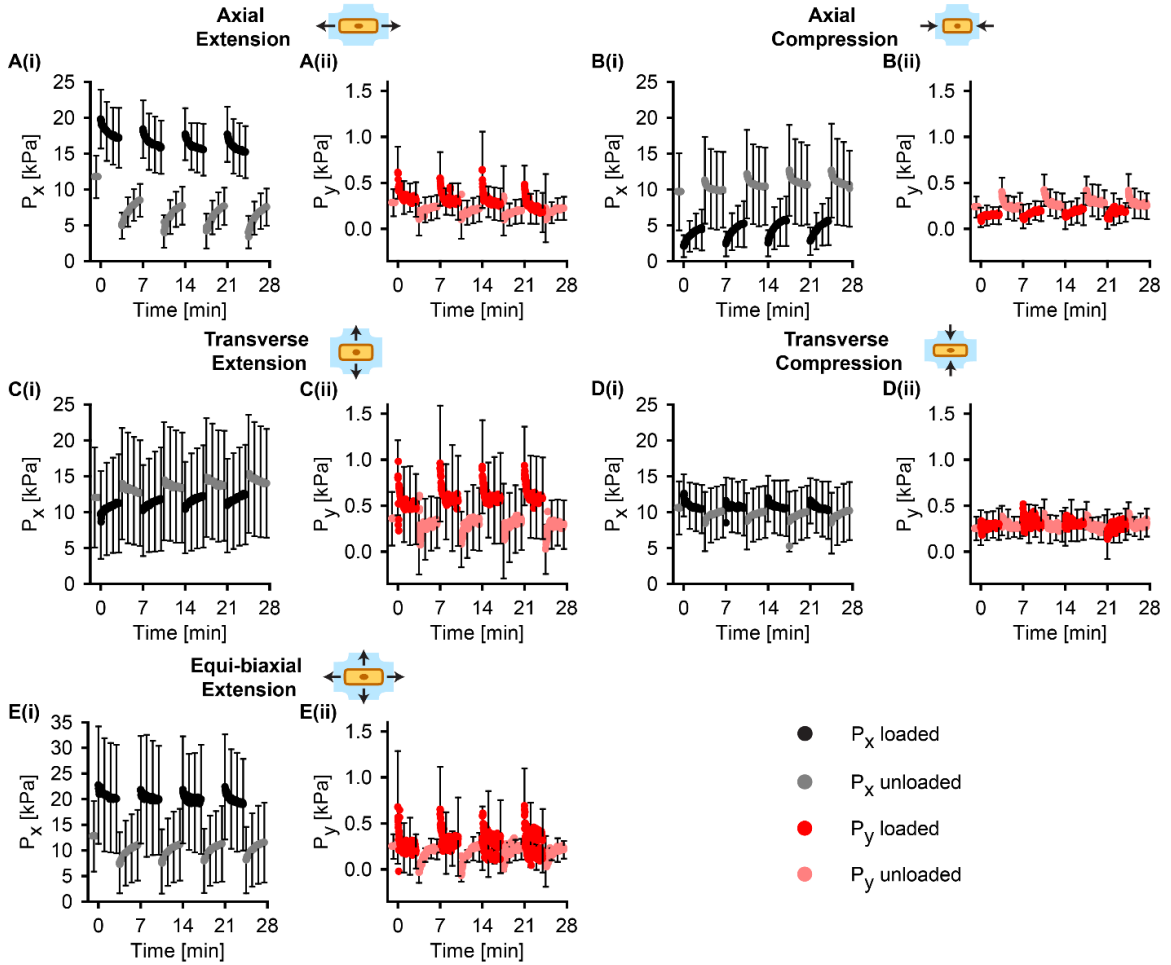


Figure 3.6. Cyclic Stretching CμBS Experiments.

First Piola Kirchoff stresses for cells exposed to (a) axial extension ($n = 7$), (b) axial compression ($n = 11$), (c) transverse extension ($n = 8$), (d) transverse compression ($n = 6$), (e) equi-biaxial extension ($n = 7$). For all stretches, (i) PK1 stress along the long axis of the cell (P_x) when unloaded ($\lambda = 1.00$) and loaded ($\lambda = 1.15$ for extension or $\lambda = 0.85$ for compression) and (ii) PK1 stress along the short axis of the cell (P_y) when unloaded ($\lambda = 1.00$) and loaded ($\lambda = 1.15$ for extension or $\lambda = 0.85$ for compression). Error bars: standard deviation.

(Fig. 3.6C(i)) and P_y (Fig. 3.6C(ii)) increased with each cycle. For transverse compression, P_x (Fig. 3.6D(i)) and P_y (Fig. 3.6D(ii)) decreased with each cycle.

Equi-biaxial stretching. VSMCs exposed to equi-biaxial cyclic step change stretching displayed stress relaxation similar to that observed in uniaxial stretching. P_x (Fig. 3.6E(i)) decreased with each cycle and P_y (Fig. 3.6E(ii)) increased with each cycle.

3.4.4 A Hill-type active fiber model predicts the cycle-dependent stress relaxation of VSMCs.

Finally, we used our model to simulate cyclic step-change loading of VSMCs. The parameters determined using the incremental loading were used in all cyclic step-change models. In these simulations, the model was able to recapitulate all of the experimentally-observed behaviors of the VSMCs (Fig. 3.7A-C). The model was able to predict the stress-relaxation observed experimentally, though the amount of stress recovery during each cycle was reduced in the model. Notably, the model reproduced the cycle-dependent changes in stress for all of the experimental conditions. Taken together, these data suggest that dynamic mechanical behavior of VSMCs can be robustly replicated with our relatively simple Hill-type active fiber model.

3.5 Discussion

Vascular tissue demonstrates time dependent mechanical properties including hysteresis [55], [141]–[144], stress relaxation [142], [145]–[148], and creep [149]–[152], typically associated with viscoelasticity. Cells are also often described as viscoelastic and hysteresis [63], [102], [103], creep [133], [134], [153]–[155], and stress relaxation [135]–[137], [156]–[158] have been measured in a variety of cell types using techniques such as

atomic force microscopy and magnetic twist cytometry. Using CuBS, we find that VSMCs have similar time-dependent behavior.

Previous studies have modeled cells as viscoelastic and typically linear [64], [105], [131], [154], [159], [160]. Hill-type fiber contraction models have been used in previous studies to model cell processes like durotaxis [161]–[163], migration [164], [165], and

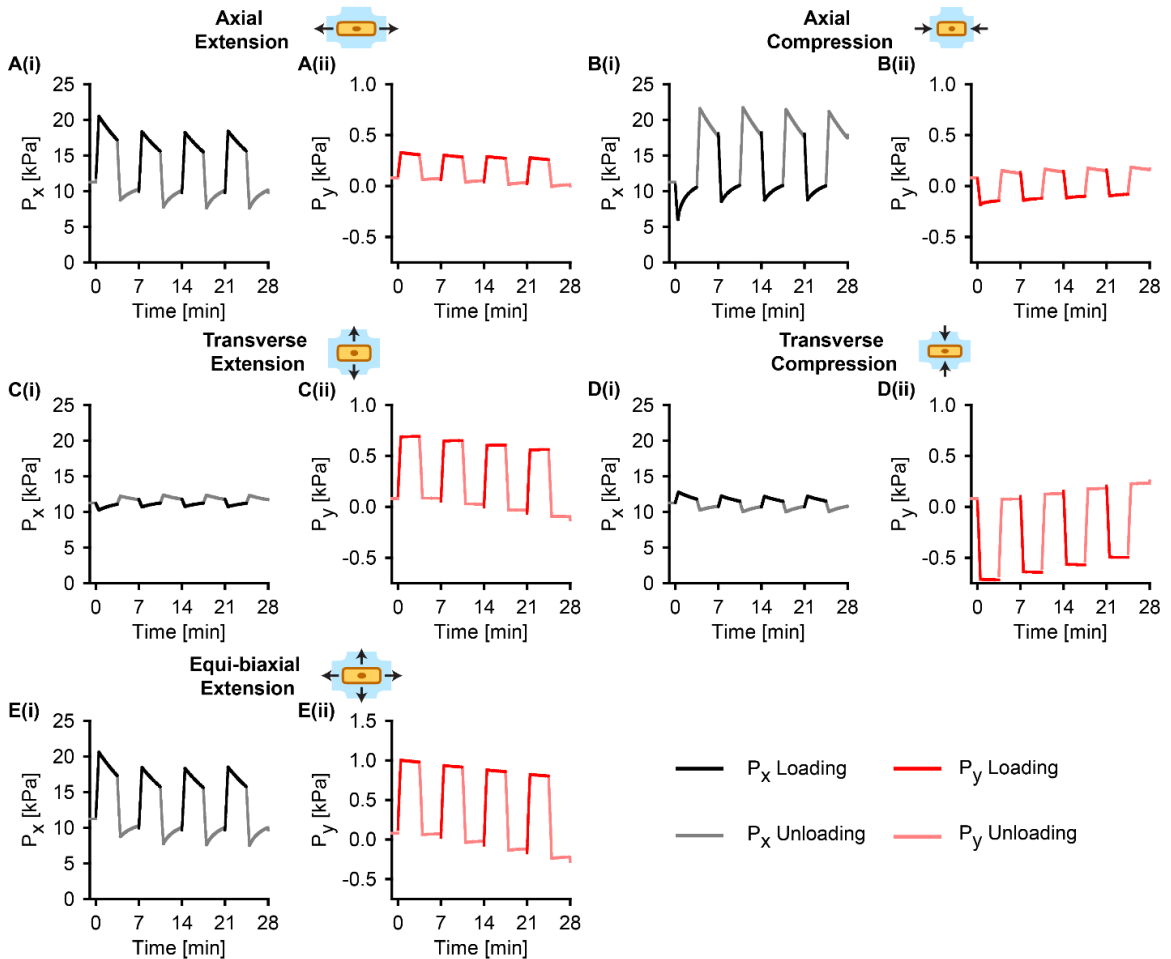


Figure 3.7. Hill-type active fiber model applied to cyclic step-change protocol.

Hill-type active fiber model for (a) axial extension, (b) axial compression, (c) transverse extension, (d) transverse compression, and (e) equi-biaxial extension. For each panel, (i) PK1 stress in the long axis of the cell (P_x) during loading and unloading and (ii) PK1 stress in the short axis of the cell (P_y) during loading and unloading.

cytoskeletal organization [166]. Here, we used a Hill-type active fiber model to model the cell as a network of actively contracting and relaxing acto-myosin fibers with organization that mimics that of the cells. We have previously shown that incorporating Hill-type active contraction and relaxation of acto-myosin fibers, such that axial fibers contract during transverse stretching, increasing P_x was able to predict differences in $C\mu$ BS-measured hysteresis in VSMCs with different geometries [71]. In this study, the parameters for the model were determined using only the data from the incremental stretching experiments. When the model was then applied to the cyclic step change experimental protocol, it was able to capture both the observed stress-relaxation and the cycle-to-cycle changes. Taken with our previous work, this result demonstrates that the Hill-type active fiber model is quite robust within the limits of the types of deformation we can apply using $C\mu$ BS.

Cyclic stretching has a significant effect on cellular behavior. Repeated cyclic stretch affects extracellular matrix protein deposition [167], [168], protein synthesis [169], [170], growth factor expression [171], [172], proliferation [113], [121], [172], [173], and differentiation [174], [175]. Notably, cyclic stretching plays a key role in differentiation of stem cells into VSMCs [175]. Chronic cyclic stretch also affects the mechanical functions of cells, such as orientation [176]–[181], spreading [182], [183], and migration [184]–[186]. Here we see that cyclic stretch causes an immediate change in the force generation by the cell. Other studies suggest that focal adhesion remodeling [187], [188] is key to controlling the stress evolution of cells in response to cyclic stretching. Our model does not include focal adhesion remodeling, but suggests that early mechanical alteration can be explained by contraction and relaxation dynamics.

Understanding the mechanical properties of single cells is important for developing models of tissue biomechanics and mechanobiology. A standard model for simulating tissue growth and remodeling is the constrained mixture model [26], [56]. In this framework, the mechanical description of each component of the tissue and organ is necessary, so the full mechanical properties of VSMCs are needed to develop robust models of vascular growth and remodeling. Many growth and remodeling models assume that tissue remodeling occurs in response to changes in cell stress [66], [189]–[193]. Our results suggest that under dynamic load, the cell stress-strain behavior is itself temporally dynamic due to active modulation of the acto-myosin cytoskeleton. Incorporation of this observation into computational models could provide important insight into initiation and progression of mechanically induced tissue growth and remodeling.

The mechanical properties of VSMCs have been shown to differ based on their anatomical location and surrounding ECM composition [194]. Here, we used VSMCs from human umbilical arteries, which are muscular arteries, and have significantly different ECM composition than elastic arteries like the aorta. While it is possible that elastic artery VSMCs differ, we believe that our findings using umbilical artery VSMCs are representative of other VSMCs under the same conditions. VSMCs can also alter their phenotype between a contractile phenotype, which primarily regulates the vessel diameter, and a synthetic phenotype, which remodels the vessel via cell proliferation or ECM synthesis [195]. Prior studies have found that VSMCs with a contractile phenotype are stiffer than those with the synthetic phenotype [196]. Here, we only studied VSMCs with a contractile phenotype, induced via a 24 hour serum starvation [197], limiting the broad application of these results to all VSMCs. Additionally, we have previously demonstrated

that VSMCs can change their functional contractility in response to changes in the mechanical properties of the substrate [41] or altered cellular architecture [73], [90], in the absence of significant changes in molecular phenotype markers. Here, we only studied cells with a single architecture and in a single mechanical environment. Prior studies have considered the mechanics of airway [69], [198], [199], colon [200] and vaginal smooth muscle cells [201], [202]. Though this study was narrowly focused, our results show promise for general characterization of time- and architecture- dependent cell mechanical properties, and is likely expandable beyond the single type of VSMC studied here.

There are several limitations of the C μ BS experiments. First, we assumed that the cell is a uniform body and ignored potential stress distributions arising from non-uniform organization of the cytoskeleton or the contribution of the nucleus, focal adhesions, or microtubules. We also only measured the stress in 2D and ignored any out-of-plane stresses, though the alignment of the actin cytoskeleton is primarily in this 2D plane so we would expect any out of plane stresses to be relatively low. Other models of cell mechanics include focal adhesion and cytoskeletal remodeling [203], [204], but we have ignored their contribution here. It is possible that contributions from other cytoskeletal components or cytoskeletal remodeling contributes to the temporal changes in stress we observed, and future models could include these elements to further strengthen their mechanical description of the experimentally observed behaviors.

In conclusion, mechanical stimuli are important for regulating cell function, and cell stress is a key contributor to tissue maintenance [88]; yet, the exact mechanisms by which forces influence function are not fully understood. The complex loading experiments

described here aimed to measure the time dependent mechanical properties of VSMCs using C μ BS and demonstrated three key findings: VSMCs display hysteresis under tensile and compressive loads, VSMCs have a cycle-dependent stress relaxation response to cyclic step-changes in strain, and that a Hill-type active fiber model was able to recapitulate the experimentally observed phenomena. Our results suggest that cell stresses are dynamic in cyclically loaded vessels due to both the changing pressure and the changing contractile tone. The results presented here have important implications in modeling of mechanobiology, as VSMCs are the most prevalent cell type in arteries and undergo constant dynamic mechanical loading. VSMCs are known to alter their function in response to changes in their mechanical environment, and since models of mechano-adaptation often assume cell stress is a primary driver of growth and remodeling, understanding the temporally dynamic response of cells to different complex loads is crucial.

Chapter 4. An experimentally validated model of the length tension relationship in cardiac myocytes

4.1 Introduction

Cardiovascular tissues are exposed to constant dynamic mechanical loads in vivo as a result of the cardiac cycle pumping blood throughout systemic circulation. During a normal cardiac cycle, the ventricular myocardium undergoes large multidirectional strains in the circumferential and longitudinal directions [205], [206]. The strains experienced by the heart muscle also changes as a result of disease such as post-myocardial infarction [207] or as a result of surgical interventions [208]. Contractile functionality is altered by these changing strains, thus, there is a need to understand how the heart mechanoadapts to its mechanical environment.

Biomechanical models provide insight into tissue behavior and are advantageous for understanding disease progression and aiding clinicians in guiding treatment. Since the heart adapts to changes in mechanical load by remodeling cardiac myocytes [209], improved predictive models of cardiac myocyte mechanoadaptation are needed to develop better therapeutic predictions. One important factor in these models that is not well-described is the dynamic response of cardiac myocytes to complex biaxial loads. Common frameworks for modeling tissue mechanical properties, such as the constrained mixture model, require mechanical descriptions of the individual components within tissues. Thus to create the most predictive models for the heart, the mechanical properties of cardiac myocytes must also be elucidated.

Cardiac myocytes, the contractile cells within the heart muscle, play an important role in the remodeling of the heart involved in development[9], [10] and pathologies[11]–[13]. Cardiac myocytes are exposed to constant applied deformations during the cardiac cycle and are mechanosensitive to stimuli such as strain and substrate stiffness[14]–[17]. In healthy hearts, cardiac myocytes exhibit a tightly controlled geometry and cytoskeletal organization in order to function optimally. The Frank-Starling Law describes the relationship between stretch in myocardial fibers and the amount of tension the muscle is able to generate [210], [211]. Muscle fibers are able to generate a maximum amount of tension when their sarcomeres are at an optimal length and as the spacing deviates from the optimum, the force able to be generated decreases. This relationship has been shown in cardiac muscle [212] and on the single cell level [31], [213], [214]. Studies have also demonstrated that the length-tension curve in cardiac muscle is sensitive to extracellular calcium concentrations [215], [216].

Previous studies characterizing single cardiac myocyte mechanical properties have used carbon fiber cantilevers [31], [32], pipette attachment systems [217], and atomic force microscopy [218]. Though these methods have advanced the study of cardiac myocyte mechanical properties on the single-cell level, they have limitations, and current studies have yet to capture the full anisotropic response of cardiac myocytes to applied strains.

The sarcomere cytoskeletal architecture is a complex three dimensional lattice of actin and myosin. Computational models [219], [220] and experiments using X-ray diffraction and osmotic compression [219], [221], [222] have suggested that lattice spacing also affects the amount of tension that striated muscle is able to generate. Some single cell studies on the length-tension curve used skinned fibers to control calcium sensitivity,

however skinned fibers do not have a constant volume and the diameter of the cell does not change as the cell is stretched meaning the lattice spacing is likely unchanged [223]. There is still a need to understand the interplay between sarcomere length, lattice spacing, and active force generation on the single cell scale in cardiac myocytes.

Here we aim to measure and characterize the relationship between sarcomere length and the force of contraction in single neonatal cardiac myocytes subjected to biaxial strains. Cellular microbiaxial stretching (C μ BS) was developed to measure single-cell mechanics and characterize the anisotropic mechanical properties of cells exposed to complex loading conditions[44], [45], [71]. Here, C μ BS is used to apply biaxial strains to cardiac myocytes micropatterned with in vivo-like geometries to probe the force-strain relationship in individual cardiac myocytes.

4.2 Methods

4.2.1 Cellular Microbiaxial Stretching.

The C μ BS device is a custom built, microscope mounted stretcher consisting of four linear actuators that transfer strains to the cells micropatterned on polyacrylamide (PA) gels on flexible elastomer membranes[44] (Fig 4.1A). Micropatterned C μ BS substrates were prepared as previously described [44], [224]. Briefly, an elastomer membrane was clamped between metal brackets and placed under slight tension. A polydimethylsiloxane (PDMS) ring was adhered to the membrane creating a well for cell culture media. PDMS stamps with rectangular features (aspect ratio: 7:1, area: 2400 μm^2) for micropatterning cardiac myocytes into an in vivo like [14] geometry were fabricated using standard photolithography techniques. Stamps were inked with human fibronectin (FN) (Gibco) for cell attachment and the FN patterns were transferred using standard

microcontact printing techniques to a fluorescent bead-doped polyacrylamide gel doped

with a Young's modulus of 13.5 kPa (Fig 4.1B).

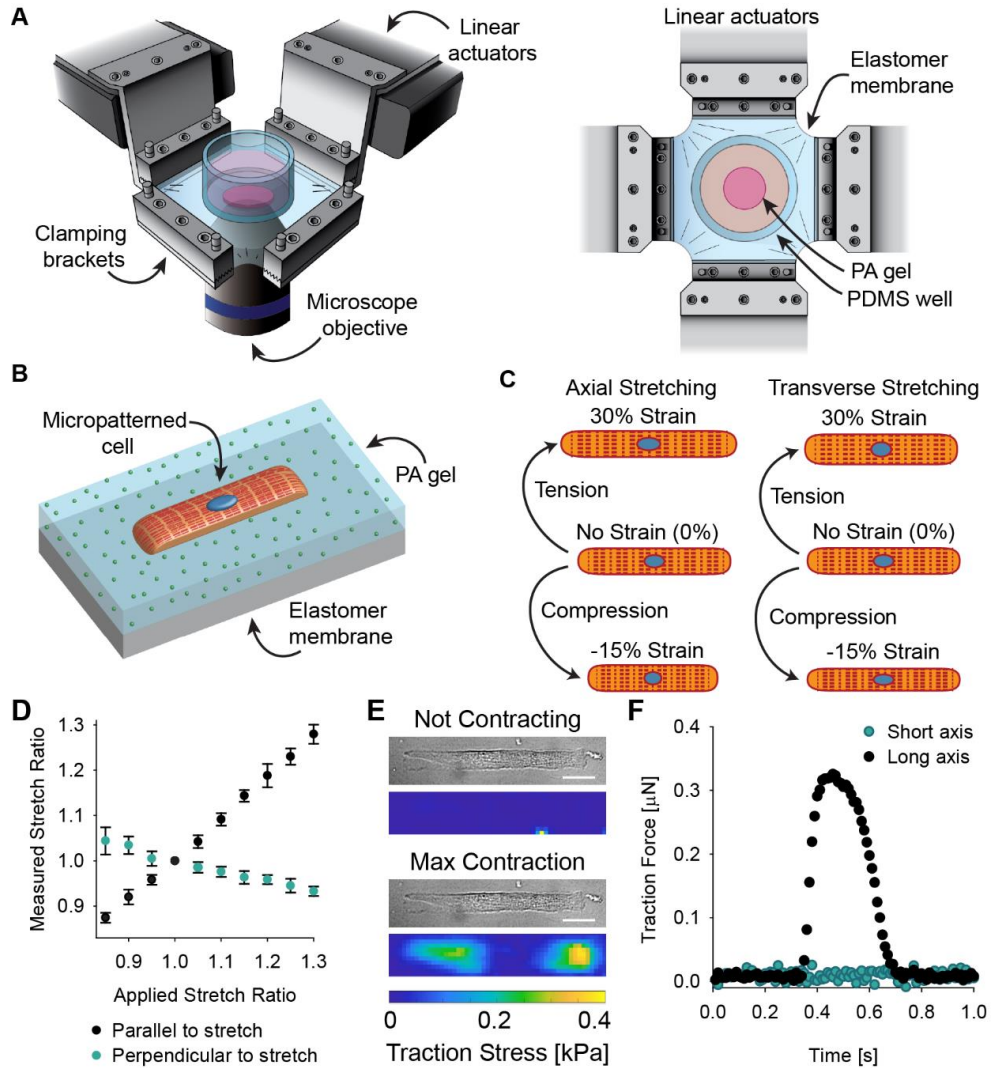


Figure 4.1. C μ BS used to measure single neonatal cardiac myocyte contraction forces.

(A) Schematics of the C μ BS device above the microscope objective (left: isometric view, right: top view), (B) Schematic of a cardiac myocyte micropatterned in an elongated geometry on a fluorescent bead-doped polyacrylamide gel adhered to an elastomer membrane, (C) Schematics of the stretching protocols applied to the cardiac myocytes, (D) Relationship between the applied grip strain and measured strain on the cells in the direction of stretch and orthogonal to the applied stretch ($n_{\text{extension}}=13$, $n_{\text{compression}}=13$) (error bars: \pm standard deviation), (E) Bright field images and corresponding traction stress maps for a cardiac myocyte at rest and at maximum contraction (scale bar: 20 μm), and (F) Trace of forces for a contracting cardiac myocyte in the direction of the long axis and short axis.

4.2.2 Neonatal mouse cardiac myocyte isolation.

Timed pregnant Black 6 mice (Charles River Labs) were ordered and housed in accordance with IACUC and university standards. Neonatal mouse ventricular myocytes were isolated using a Worthington Biochemical Neonatal Cardiomyocyte Isolation System (Worthington Biochemical Corporation) and standard methods [225]. Briefly, hearts were isolated from Day 0-1 neonatal mice. The ventricles were removed, rinsed with HBSS, minced, and incubated in trypsin at 4 °C overnight. The next day, the tissue was digested with collagenase and passed through a filter to remove the cells from undigested tissue. The isolated cells were seeded onto the polyacrylamide gels in cell culture media comprised of media 199 (Gibco) supplemented with FBS (Gibco), glucose (Fisher Chemical), vitamin B12 (Sigma-Aldrich), Penicillin (MP Biomedicals, LLC), L-glutamine, HEPES (Gibco), and MEM NEAA (Gibco) at a density of approximately 250,000 cells per well. Cells were left undisturbed for 24 hours to allow for attachment to the FN micropatterns. Cells were switched to a 2% FBS supplemented media 24 hours before experimentation.

4.2.3 Stretching protocol.

Using the C μ BS device, traction force microscopy experiments were performed on the micropatterned cardiac myocytes exposed to biaxial strains to quantify the active force of contraction as a function of stretch. Four straining protocols were applied to the micropatterned cells such that the cell was extended (tension) or shortened (compression) parallel to its long (axial) or short (transverse) axis (Fig 4.1C). Strains were applied in 5% increments at 0.5 %/s to a maximum of 30% applied strain for tension or -15% applied strain for compression. At each increment, images for performing traction force microscopy

analysis were acquired including a brightfield image of the cell was acquired and a high temporal resolution (100 frames per second) image of the fluorescent bead layer under the contracting cell. Myocytes were paced at 1 Hz using an Ionoptix MyoPacer to induce contraction. After stretching, cells were lysed with a 0.5% sodium dodecyl sulfate solution and an undeformed fluorescent bead layer images were acquired for each stretch. All experiments were performed in a temperature and CO2 controlled environment to preserve viability. Due to the constraint of PDMS ring, end-to-end membrane strain was not identical to the strain applied to the cell and measured cell stretch ratios were determined from the initial and deformed geometries of the cells (Fig 4.1D).

4.2.4 Force analysis.

During contraction, the cell exerts a maximum force at the peak of contraction and a minimum (passive) force when the cell is not contracting. The difference between the maximum and passive forces is the active force of contraction. The cell induced bead displacement during contraction was calculated using a particle image velocimetry algorithm comparing the uncontracted and contracted bead layer images. An unconstrained Fourier transform traction cytometry algorithm [74] (regularization factor $1e-9$, Poisson's ratio: 0.5) was used to form traction stress vector fields from the beads displacements (Fig 4.1E). Substrate traction force vectors were defined by $\mathbf{T}^n a^n$ where $\mathbf{T}^n = T_x^n \mathbf{e}_x + T_y^n \mathbf{e}_y$ is the traction vector acting on area a^n and \mathbf{e}_i is the unit vector in the i direction. Substrate tractions are balanced with cell forces (\mathbf{f}^n) at the interface of the cell and the PA gel, such that $\mathbf{f}^n = f_x^n \mathbf{e}_x + f_y^n \mathbf{e}_y = -T_x^n a^n \mathbf{e}_x + -T_y^n a^n \mathbf{e}_y$. Forces oriented away from the center of the cell were denoted as tensile (positive). The total tensile force $2f_x = \sum_n f_x^n r_x^n / |r_x^n|$

and $2f_y = \sum_n f_y^n r_y^n / |r_y^n|$, where $\mathbf{r}_n = r_x^n \mathbf{e}_x + r_y^n \mathbf{e}_y$ is the vector describing the location of n with respect to the center of the cell.

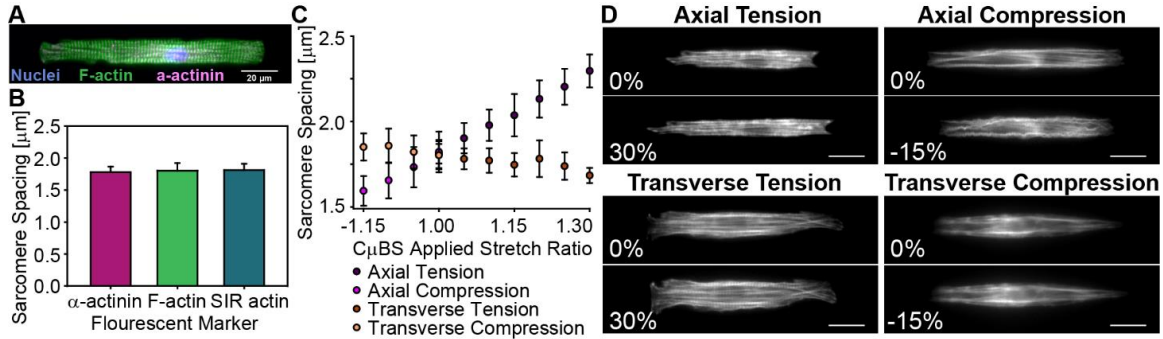


Figure 4.2. Sarcomere length changes during CμBS.

(A) Micropatterned cardiac myocyte stained to visualize the sarcomere structure showing nuclei (blue), F-actin (green) and a-actinin (magenta), (B) Length between sarcomeres measured using fast Fourier transform of IF stained or SIR actin stained cardiac myocytes ($n_{IF}=26$, $n_{SIR}=32$), (C) Change in sarcomere spacing resulting from each type of stretch as measured from SIR actin images ($n_{axial, tension}=8$, $n_{axial, compression}=13$, $n_{transverse, tension}=5$, $n_{transverse, compression}=6$), and (D) SIR actin images of stretched myocytes under axial tension, axial compression, transverse tension, and transverse compression. (scale bars: 20 μm) (error bars: \pm standard deviation)

4.2.5 Cell architecture analysis.

Immunofluorescence. Standard immunofluorescent staining techniques were used to visualize the cytoskeleton of the micropatterned cardiac myocytes. Cardiac myocytes seeded on to micropatterned on 13.5 kpa polyacrylamide gels on glass coverslips were fixed in 4% paraformaldehyde. Cells were then permeabilized in 0.05% Triton and blocked in 10% bovine serum albumin. Cells were incubated antibodies for α -actinin (Abcam), phalloidin (Invitrogen), and DAPI (Invitrogen) to visualize Z-discs, F-actin, and nuclei, respectively (Fig 4.2A).

SIR actin live cell stain. Micropatterned cells were dosed with SIR actin (Spirochrome) to a final concentration of 1 nM for 1 hr in the incubator. Myocytes were subjected to the same stretching protocol used for TFM, but only a single fluorescent image of the actin cytoskeleton and a bright field image of the cell was acquired at each stretching increment (Fig 4.2D).

Fast Fourier Transform spacing calculations. Sarcomere spacing was determined from the fluorescent images of F-actin and α -actinin architecture. In FIJI, fiber bundles were traced using the line tool and the intensity profile was measured along the line for the length of the bundle. Using a fast Fourier transform (fft) in Matlab, the peak frequencies of the intensity profile were obtained. The peak frequency corresponded to end of each sarcomere subunit, and was converted into the distance between sarcomeres using the pixel size of the original image (1 pixel = 0.161 μm). This was performed using immunofluorescent images of α -actinin and F-actin as well as the SIR actin images of F-actin at different stretches. The analysis was repeated for at least two fiber bundles with discernable sarcomeres per cell per stretching increment.

4.2.6 Activation based model for active force of contraction.

A contraction based model previously used to model epithelial morphogenesis [226] and arterial growth and remodelling [57] was used to model the active force of contraction of cardiac myocytes as a function of strain. Two models were considered: the sarcomere length model in which the force is dependent on the length of the sarcomere as measured from z disc to z disc and the length-radial spacing model in which the force is dependent on the length of the sarcomere as well as the radial distance of the actin from the myosin. In both models, the cell was treated as anisotropic and incompressible, undergoing

deformation in the principal orientation such that the deformation gradient tensor is given by $\mathbf{F} = \text{diag}[\lambda_x, \lambda_y, \lambda_z]$ where λ_i is the stretch ratio in the i direction. As such,

$$\lambda = \lambda^* \lambda_a \quad (1)$$

where λ is the measured stretch ratio from CμBS, λ_a is the activation stretch ratio, and λ^* is the elastic stretch ratio computed relative to the zero-stress configuration.

In the sarcomere length model, the active force of contraction, f_a , varies with changes in cell stiffness and zero stress length with a peak value at some stretch ratio giving the form:

$$f_a = \begin{cases} C_a(\lambda^*)(\lambda^* - 1)(\lambda_{crit}^* - \lambda^*), & \text{for } \lambda^* \leq 1 \text{ and } \lambda^* \leq \lambda_{crit}^* \\ 0, & \text{for } \lambda^* > 1 \text{ and } \lambda^* > \lambda_{crit}^* \end{cases} \quad (2)$$

where material coefficient C_a is the active cell stiffness and λ^* is the elastic stretch ratio relative to the active zero-stress configuration. In this model, the active force is zero when the cell is undeformed relative to its zero-stress length, λ^* , or when stretched beyond a maximum value, λ_{crit}^* , at which point contraction is no longer possible.

In the length-radial spacing model, actin is assumed to be distributed circularly around the myosin at an initial radius, r_0 (Fig 4.4B). In the post stretch configuration, actin is assumed to distribute uniformly in an elliptical array around the myosin allowing us to calculate the distance of the actin from the myosin as a function of the angle, θ :

$$r = r_0 \lambda_y \lambda_z (\lambda_z^2 \cos^2 \theta + \lambda_y^2 \sin^2 \theta)^{-1/2} \quad (3)$$

Consistent with previous models of lattice spacing and force [219], we can define a radial parameter for a single myosin interaction, R_m , that describes the difference in force generated by a single myosin, f_m , compared to the force at optimal lattice spacing, f_{m0} , such that

$$R_m = \frac{f_m}{f_{m0}} = C_R \left(1 - \frac{r}{r_0}\right)^2 \quad (4)$$

where f_m is assumed to be a function of the change in lattice radius and a scaling factor C_R .

Using quarter symmetry of the ellipse, the average integral of R_m yields radial parameter,

R , as defined by:

$$R = \frac{1}{\pi/2} \int_0^{\pi/2} R_m d\theta \quad (5)$$

Using the radial parameter, contributions from radial interactions of actin and myosin are incorporated into the sarcomere length model to give the length-radial spacing model with form:

$$f_a = \begin{cases} C_a(\lambda^*)(\lambda^* - 1)(\lambda_{crit}^* - \lambda^*)(1 - R), & \text{for } \lambda^* \leq 1 \text{ and } \lambda^* \leq \lambda_{crit}^* \\ 0, & \text{for } \lambda^* > 1 \text{ and } \lambda^* > \lambda_{crit}^* \end{cases} \quad (6)$$

For each model, the parameters λ_a , λ_{crit}^* , C_a , and C_R were fit to the axial stretching active force data using least square mean regression to find the minimum error between the model and the experimental data. The same values for the fitting parameters determined from the axial stretching data were then used to model the active force during transverse stretching.

4.3 Results

4.3.1 Sarcomere spacing changes linearly with measured cellular deformations applied with C μ BS.

Myocytes fixed and immunofluorescently stained for α -actinin and F-actin had resting sarcomere length of $1.78 \pm 0.08 \mu\text{m}$ and $1.80 \pm 0.12 \mu\text{m}$ measured using fft analysis of each respective component. The initial sarcomere length in live cells stained with SIR actin was $1.81 \pm 0.10 \mu\text{m}$, which was not significantly different from the F-actin and α -actinin measurements in immunofluorescently cells (Fig 4.2B). When myocytes stained

with SIR actin were stretched axially, sarcomere spacing increase as the cell was extended and decreased as the cell was compressed. Overall, sarcomere spacing changed ~4% with each 5% increment of C μ BS applied strain in the axial direction (Fig 4.2C). When myocytes were stretched transversely, the spacing of the sarcomeres remained relatively unchanged compared to stretching in the axial direction; however, the spacing did increase slightly as the cells were compressed and decreased slightly as the cells were extended. Sarcomere spacing changed ~1% with each 5% increment of C μ BS applied strain in the transverse direction (Fig 4.2C). The rates of change of sarcomere lengths resulting from both axial and transverse stretching are consistent with the measured changes in strain to the cells resulting from C μ BS.

4.3.2 Cardiac myocyte force of contraction is anisotropic in response to biaxial strains.

When cells were axially extended (Fig 4.3A), the active force initially increased as the cell is extended, but the force then generally decreased past 15% applied strain (Fig 4.3B). When the myocytes were axially compressed (Fig 4.3C), the active force decreased as the cells were compressed (Fig 4.3D). A similar trend was observed when the cells were stretched transversely. When the cells were extended in the transverse direction (Fig 4.3E), the force did not change much initially, but then decreases with increasing stretch (Fig 4.3F). The active force decreased more for cells extended transversely than for cells extended axially at the final strain ($\lambda = \sim 1.27$). Under transverse compression (Fig 4.3G), the force decreased with each increment, though generally less than under axial tension (Fig 4.3H). Normalizing the active force at each stretch to the initial, unstretched force, these trends become more evident. For axial stretching (Fig 4.3I), the active force

decreased as the cell was compressed and force increased as the cell was extended until ~15% applied strain when the force begins to decrease with increasing stretch.

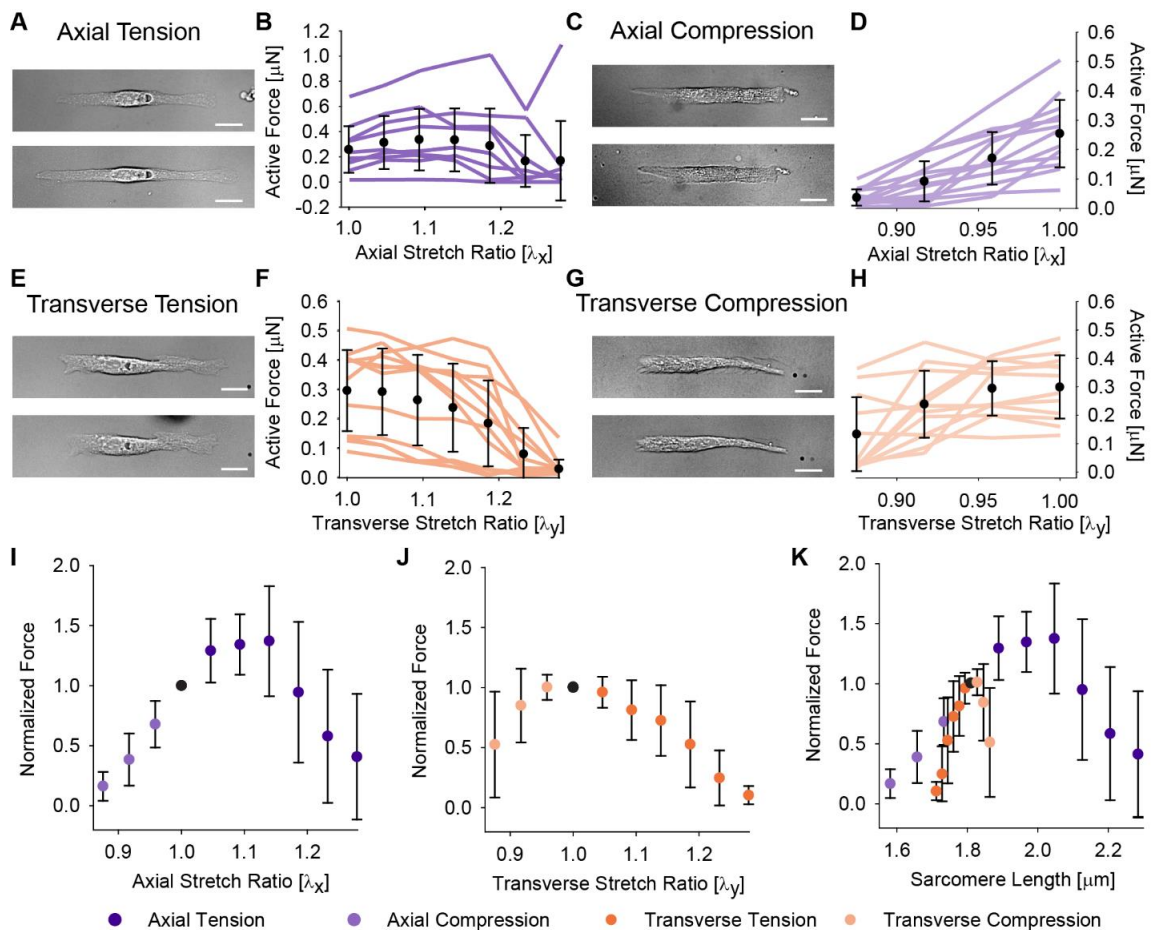


Figure 4.3. Active force of contraction for cardiac myocytes during C μ BS.

(A) Brightfield images of cardiac myocytes under axial tension, (B) Active force - stretch data for cells extended axially (n=11), (C) Brightfield images of cells under axial compression, (D) Active force - stretch data for cells compressed axially (n=13), (E) Brightfield images of cells under transverse extension, (F) Active force - stretch data for cells extended transversely (n=12), (G) Brightfield images of cells under transverse compression, (H) Active force - stretch data for cells compressed transversely (n=10), (I) Active force - stretch normalized to the unstretched force for cells stretched axially, (J) Active force - stretch data normalized to the unstretched force for cells stretched transversely, and (K) Normalized axial force for axial and transverse stretching compared using measured sarcomere lengths from SIR actin stained cells.

(scale bars: 20 μm) (error bars: \pm standard deviation)

For transverse stretching (Fig 4.3J), the active force generally decreased with increasing extension and compression. Using the sarcomere lengths measured from SIR actin analysis, the force produced at different sarcomere lengths for the four types of stretches were compared (Fig 4.3K). The active force in the cells stretched transversely decreased faster than for cells stretched axially both as the sarcomere lengths increased and decreased. The transversely stretched cells did not experience the same initial increase in force with increase in sarcomere spacing that the axially stretched myocytes did. These results demonstrate that sarcomere length alone does not dictate active force generation.

4.3.3 Consideration of the radial organization of actin and myosin in modeling captures the biphasic force response to biaxial stretching.

We aimed to develop a simple and biologically relevant model to characterize the relationship between stretch and the active force of contraction in cardiac myocytes. Here, we adapted a previously used [57], [226], [227] active contraction based model for this purpose. Initially, the model considered only the lengths of the sarcomeres. The sarcomere length model was fit to the experimental data for axial stretching ($C_a = 34.6 \mu\text{N}$, $\lambda_a = 0.86$, and $\lambda_{crit}^* = 1.54$). This model fits the axial stretching data well for all strains (Fig 4.4C), but does not align with the transverse stretching data (Fig 4.4D). The model also fails to capture the overall trend of the experimentally observed behavior for transversely stretched cells and diverges significantly from the experimental values at large deformations, particularly for cells under compression.

The radial spacing term was added to the model to account for the 3D lattice structure of the sarcomere and radial organization of actin thin filaments around myosin thick filaments. CμBS is not a purely strip biaxial stretching experiment due to the media

constraining in ring adhered to the PDMS membrane. Since the cell is assumed to be incompressible, as it is extended axially, it is compressed slightly in the transverse direction and when the cell is extended transversely, it is compressed slightly in the axial direction. During the stretches applied during C μ BS, the actin interacts radially around the myosin such that as the cell is stretched axially, the actin will move closer to the myosin in both the y and z directions, but as the cell is extended transversely, the actin will move away

from the myosin in the y-direction but still move closer to the myosin in the z-direction (Fig 4.4A). The radial term accounts for this change in spacing of actin from an assumed initial circular distribution to an elliptical deformed configuration (Fig 4.4B). Again, the model parameters were fit to the axial stretching experimental data ($C_R = 4.2$ nN, $C_a = 25.9$ μ N, $\lambda_a = 0.86$, and $\lambda_{crit}^* = 1.68$) and the radial model was able to recapitulate the axial stretching data similarly to the sarcomere length model (Fig 4.4C). Using the same parameters to model transverse stretching, the radial model was able to more closely

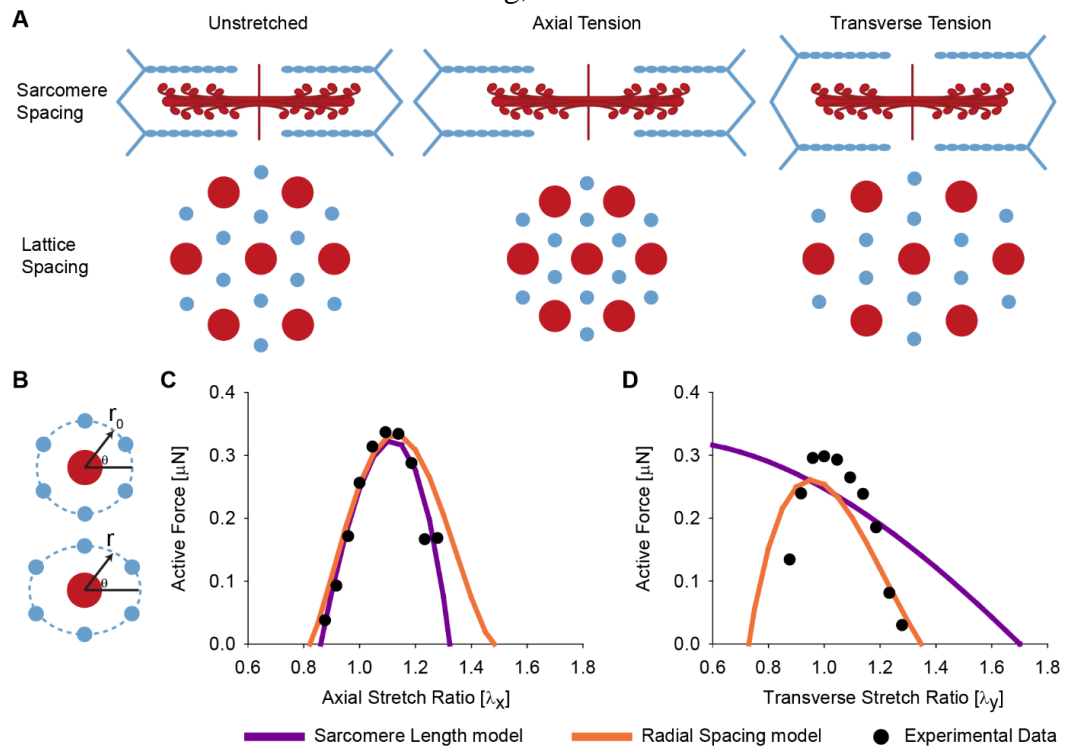


Figure 4.4. Active contraction based model considering sarcomere length and lattice spacing recapitulates experimentally observed force trends.

(A) Schematic of how the length between sarcomeres and lattice spacing between actin and myosin changes under axial and transverse tension, (B) Schematic of the rationale behind the radial term for the model, (C) Sarcomere length and radial spacing models compared to experimental data for axial stretching, and (D) Sarcomere length and radial spacing models compared to experimental data for transverse stretching

recapitulate the biphasic trend in active force observed experimentally. Without refitting any parameters, the model was able to represent the decrease in active force as the cell was transversely compressed and extended without diverging too significantly from the experimental data (Fig 4.4D). This indicates that it is necessary to consider not only sarcomere length, but also lattice spacing when writing mechanical descriptions of cardiac myocytes, and that a relatively simple representation of actin and myosin interactions is able to recapitulate the force-stretch relationship in single cardiac myocytes.

4.4 Discussion

The length-tension curve has yet to be fully elucidated on the single cell level in cardiac myocytes and there is a need to better understand the interplay between sarcomere length, lattice spacing and active force generation in cardiac myocytes. Current understanding of the length tension curve in cardiac tissue states that as the spacing deviates from its optimum length, the amount of tension will decrease. The mechanics of cardiac myocytes on the single cell level have been investigated using a variety of different techniques to measure length-tension relationship. Here, we measure the length-tension relationship in single neonatal cardiac myocytes using C_μBS which allows us to quantify the force produced by the cell while controlling its deformations in two dimensions to account for changes in sarcomere length and lattice spacing.

Cardiac myocytes have a regulated structure and are the force producing cells responsible for pumping blood throughout the body. As such, it is important to understand the interplay between their structure and function in order to predict how changes to their mechanical environment affect their behavior. Neonatal cardiac myocytes have a relatively immature structure compared to adult cardiac myocytes. Micropatterning cardiac myocyte

in different aspect ratios have shown to influence their contractility and the lateral registration of sarcomeres to more mimic a mature phenotype [14]. Here, the active force of contraction of single neonatal cardiac myocytes micropatterned with an in vivo like architecture was measured as a function of the sarcomere spacing. Using the micropatterns, the cardiac myocytes had sarcomeres generally aligned along the long axis of the cell allowing us to target the stretches and force measurements to the sarcomere or lattice spacing better than if the neonatal myocytes were allowed to attach in an unconstrained manner. Substrate stiffness also influences cardiomyocyte maturation, structure, and function [15], [228]–[230].

Here, we have performed biaxial stretching on single cells while holding other external mechanical stimuli constant. Importantly, our findings suggest that we are able to change the spacing of the sarcomeres or manipulate the lattice spacing yielding different length-tension curves for stretching in different directions relative to the alignment of the sarcomere. Furthermore, by fitting a simple, biologically relevant model to the data for stretching in one direction, we are able to recapitulate the forces generated when stretched in the other. This has demonstrated the ability of C μ BS to be a useful tool for characterizing cardiac biomechanics as it's able to measure the changes in sarcomere architecture and mechanical properties of myocytes in response to short term changes in load. This could have broader impacts for studying growth and remodeling in cardiac myocytes as it is hypothesized that cardiac myocytes adapt to long term changes in load by remodeling their cytoskeletal architecture by adding sarcomeres in order to return their mechanics to a homeostatic level.

The sarcomere cytoskeleton within striated muscle is a three dimension lattice of actin and myosin. It has also been theorized that lattice spacing in addition to sarcomere spacing influences the force generation in striated muscle. Because measuring lattice spacing during stretch is complex, teasing out its influence on force is more challenging to accomplish experimentally. X-ray diffraction and osmotic compression have been used to measure and change the lattice spacing of skinned fibers and muscle [231], [232]. Using transverse stretching, the effect of lattice spacing on active force generation was targeted. Using C μ BS, the cell was stretched transversely, but the spacing between sarcomeres remained experienced relatively small deformations (\sim -6% decrease in spacing at 30% transverse tension and \sim 3% increase in spacing at -15% transverse compression). When the forces generated under transverse tension are compared to those under axial tension for each sarcomere spacing, the cell's mechanical response is very different. This indicates that the spacing between sarcomeres alone is not responsible for the changes in force that we observed and that the lattice spacing is being altered affecting the active force of the myocytes. Our model shows that by incorporating a simple parameter accounting for changing lattice spacing into a contraction based model for the active force based on the sarcomere lengths, the experimentally observed trends are able to be recapitulated both as the cell is stretched parallel and perpendicularly to the alignment of its sarcomeres. This is consistent with the other models that have suggested a role for lattice spacing in the force generation of cardiac muscle.

Here we demonstrated the ability of C μ BS to measure cardiac myocyte changes in cytoskeletal architecture and cell forces in response to short term stretching, but these finding have other implications for studying remodeling relevant to creating models for

disease. C μ BS has previously been used to measure cellular mechanical and architectural responses to long term strains in vascular smooth muscle cells showing that they mechanoadapt over time to reach a homeostatic stress [193]. In cardiomyopathies, the heart grows eccentrically or concentrically in an effort to reach a homeostatic loading condition as a result of volume or pressure overload, respectively, resulting in ventricular dilation or wall thickening [233]. This tissue level change is reflected on the cellular level as cardiac myocytes have been shown to remodel in response to static applied strains by addition of sarcomeres in series or parallel [24], [25]. Because heart function is implicated in many different diseases, studying the mechanical properties and functional contractility of cardiac myocytes is important for understanding diseases [234] and evaluating potential therapeutic targets [235]. In diabetes, cardiac myocytes are stiffer as measured by AFM [236], have altered calcium sensitivity and sarcomere contractile dysfunction [237], [238]. Mouse models for Duchenne muscular dystrophy have demonstrated a marked difference in function in response to stretch and a membrane stabilizing copolymer has shown that it can preserve function in vivo [29]. C μ BS has the potential to measure disease induced differences in functionality resulting from changes in the structure of the cells.

With the increase in interest of tissue engineering especially with iPSC-derived cardiomyocytes there is a need to ensure that the function of engineered cells and tissues are functioning properly. The use of CM-iPSCs in vitro models of the heart for drug discovery and regenerative medicine applications are limited by their structural and functional immaturity. Several studies have used TFM and neonatal rodent myocytes as a standard for comparison of function and maturation in CM-iPSCs [239] as well as the influence of other mechanical cues such as substrate mechanics [16] and cyclic stretching

[240]. C μ BS could provide a good method for robustly characterizing the functional maturation of CM-iPSCs due to its ability to perform various stretching protocols on substrates with tunable stiffness.

Here, we present a simple model relying only on the spacing of actin thin filaments and myosin thick filaments within the cytoskeleton of the cardiac myocytes. Microtubules are a part of the non-sarcomeric cytoskeleton in cardiac myocytes, but are essential for proper structure and function in healthy cells and are implicated in several diseases effecting the functioning of the heart muscle. Microtubules are also involved in the mechanics of cardiac myocytes and have been shown to contribute to the viscoelasticity of cardiomyocytes [241]. Microtubules have been shown to buckle when contracting in conjunction with sarcomere shortening and this buckling contributes to the strength of cardiac muscle and is thought to act like a spring to return the cell to its original non contracting shape [242]. Changing the interaction between microtubules and the sarcomere via detyronisation affected the stiffness of the myocytes and impeded contraction [243]. Failing cardiomyocytes have a detyrosinated microtubule network associated with increased myocyte stiffness and impaired contractility which is implicated in the heart dysfunction and failure [244]. Using pharmacological agents to target detyrosinated microtubules restored contractile function in cardiac myocytes [241]. The mechanics of cells are very complex and contributions from other cytoskeletal components also exert influence over cellular mechanical properties and should be considered in future models. Additionally, C μ BS could be used to evaluate how using pharmaceuticals to target the cytoskeleton of cardiac myocytes affects function.

Chapter 5. Conclusions

5.1 Summary

The research described here has led to four main conclusions: 1) VSMCs have linear mechanical properties under large deformations, and the actin-myosin alignment is a primary mediator of anisotropic cell stress, 2) VSMCs display hysteresis under tension and compression, 3) VSMCs exhibit cycle dependent, stress relaxation in response to cyclic strains and 4) cardiac myocyte force generation during contraction is dependent on both sarcomere length and lattice spacing.

5.2 Impact

Cardiovascular disease is a leading cause of death worldwide and better understanding of the underlying mechanisms of disease progression is needed to improve patient care. The cardiovascular system is inherently mechanically dynamic due to the heart pumping blood throughout the body and blood vessels dilating and constricting to maintain blood pressure. The active components of cardiovascular tissues responsible for these functions are cardiac myocytes and vascular smooth muscle cells, respectively. These cells are not only responsible for force generation but have also been implicated in tissue remodeling such as that seen in cardiovascular disease. Since cardiovascular disease changes the mechanical environment experienced by the cells and maladaptive remodeling of these cells contributes to cardiovascular disease, there is a need to better understand cellular mechanics.

Biomechanics of soft tissues are often investigated using elasticity based methods such as biaxial characterization which considers the structure of the tissue in its mechanical

function. Many methods to describe cellular mechanics report linear moduli that neglect structural anisotropy within the cell. Many cells exhibit specialized geometries in vivo, with anisotropic cytoskeletal architectures reflective of their function, that influence their mechanical behavior. In vivo, cells are exposed to dynamic biaxial loads rather than purely uniaxial strains, highlighting the need for more complete descriptions of their anisotropic mechanical properties under complex deformations.

The work presented in this thesis utilized the C μ BS assay to make novel measurements of the dynamic mechanical properties of single cardiovascular cells while considering cellular anisotropy due to cytoskeletal structure. I was able to experimentally measure and mathematically describe the architecture-dependent anisotropic stress-strain relationship in VSMCs, stress-relaxation in VSMCs, and force-stretch relationship in cardiac myocytes exposed to a variety of complex loading conditions including large strains, compression, and cyclic stretching. Characterizing the mechanical properties of single cells is important for developing descriptive models of tissue mechanics and improving the understanding of mechanically driven cell processes. The results presented herein could be used in the future to create clinically relevant tissue models of disease and surgical interventions as well as guide future studies into cellular mechanics.

5.3 Future directions

The work described in this thesis builds off previous studies using C μ BS to measure the mechanical properties of VSMCs. Altogether, this thesis demonstrates that C μ BS is an effective method for measuring the dynamic, time- and architecture-dependent mechanical properties of single cardiovascular cells under a variety of loading conditions. This can be expanded upon to further understand the influence of mechanical stimuli on the structure

and function of cells and how changes to their mechanical environment lead to the maladaptive remodeling seen in disease.

Here, C μ BS was used to investigate the short-term stress relaxation behavior of VSMCs during cyclic stretching. Both VSMCs and cardiac myocytes undergo repeated cyclic stretching in vivo. Cells remodel the alignment of their actin cytoskeletons in response to cyclic stretching [245], [246]. Adapting C μ BS to cyclically stretch cells over a longer time scale could provide novel insights into how cells respond to dynamic substrates by both measuring changes in cytoskeletal alignment and cell stress simultaneously. C μ BS has also been used on longer timescales to measure mechanoadaptation in VSMCs. In response to chronic strains, VSMCs exhibited targeted growth behavior and adapted their stress to pre-stretch levels consistent with the belief that cells have a homeostatic “target stress” [193]. Here, I measured changes in sarcomere spacing and cell forces in response to short term loading in cardiac myocytes. However, cardiac myocytes are theorized to adapt to chronic, long term loads by addition of sarcomeres in series and parallel [24], [25]. Implementing C μ BS to measure cardiac myocyte stress evolution and cytoskeletal remodeling in response to long-term, chronic strains would provide novel insight into cardiac myocyte mechanoadaptation, growth and remodeling.

In this thesis, the contributions of actin and myosin were considered when characterizing cell mechanics. Though actin and myosin were the components responsible for generating most of the cell stress in VSMCs, cell mechanics are complex and there are other cytoskeletal components that could play a role. Similar studies to those presented here could be performed to investigate the contributions of other cytoskeletal components

such as using a live stain for microtubules since they play a role in the viscoelastic properties of cardiac myocytes.

Lastly, C μ BS is useful when assessing the functionality and maturation of cardiac myocytes from disease models and the effectiveness of potential therapies to restore function. iPSCs have great potential to be used in a variety of clinical and therapeutic applications, especially in the treatment of cardiovascular diseases. One limitation of iPSC-derived cardiac myocytes is their relative structural and functional immaturity. C μ BS could be a useful tool for creating metrics for maturation of iPSC-derived cardiac myocytes by characterizing how their structure and function change as a result of culture. This could help determine the best differentiation protocols for creating iPSCs with in vivo like functionality.

Additionally, diseases affecting the cytoskeleton of the cell, such as Duchenne muscular dystrophy (DMD), have different functionality. DMD-affected cells lack the protein dystrophin that connects the internal cytoskeleton to the extracellular environment resulting in a fragile cell membrane, increased cell stiffness, and increased susceptibility to stretch induced injury [247]. C μ BS could provide useful insights into functional differences in cardiac myocytes from animal models and iPSC derived models for DMD by quantifying their structure-function relationship in response to stretch. Additionally, membrane stabilizers have been investigated as a potential therapy for muscular dystrophy because they increase membrane integrity and robustness in response to stretch [29], [248]. Using C μ BS, metrics can be created for quantifying the efficacy of treatments targeting the membrane and cytoskeleton in order to restore mechanical functionality and prevent cellular damage in DMD-affected cardiac myocytes.

Bibliography

- [1] “Cardiovascular diseases (CVDs),” *World Heal. Organ.*, 2017.
- [2] H. D. Intengan and E. L. Schiffrin, “Vascular Remodeling in Hypertension,” *Hypertension*, vol. 38, no. 3, pp. 581–587, Sep. 2001.
- [3] B. H. Lorell and B. A. Carabello, “Left Ventricular Hypertrophy,” *Circulation*, vol. 102, no. 4, pp. 470–479, Jul. 2000.
- [4] K. Modesto and P. P. Sengupta, “Myocardial Mechanics in Cardiomyopathies,” *Prog. Cardiovasc. Dis.*, vol. 57, no. 1, pp. 111–124, 2014.
- [5] N. S. Khoo, J. F. Smallhorn, S. Kaneko, K. Myers, S. Kutty, and E. B. Tham, “Novel insights into RV adaptation and function in hypoplastic left heart syndrome between the first 2 stages of surgical palliation,” *JACC Cardiovasc. Imaging*, vol. 4, no. 2, pp. 128–137, Feb. 2011.
- [6] M. A. Fogel, P. M. Weinberg, A. J. Chin, K. E. Fellows, and E. A. Hoffman, “Late ventricular geometry and performance changes of functional single ventricle throughout staged fontan reconstruction assessed by magnetic resonance imaging,” *J. Am. Coll. Cardiol.*, vol. 28, no. 1, pp. 212–221, Jul. 1996.
- [7] C. Petko, A. Uebing, A. Furck, C. Rickers, J. Scheewe, and H.-H. Kramer, “Changes of Right Ventricular Function and Longitudinal Deformation in Children with Hypoplastic Left Heart Syndrome before and after the Norwood Operation,” *J. Am. Soc. Echocardiogr.*, vol. 24, no. 11, pp. 1226–1232, Nov. 2011.
- [8] S. C. Menon, L. L. Minich, T. C. Casper, M. D. Puchalski, J. A. Hawkins, and L. Y. Tani, “Regional myocardial dysfunction following Norwood with right ventricle to pulmonary artery conduit in patients with hypoplastic left heart

- syndrome,” *J. Am. Soc. Echocardiogr.*, vol. 24, no. 8, pp. 826–833, Aug. 2011.
- [9] M. J. B. van den Hoff, B. P. T. Kruithof, A. F. M. Moorman, R. R. Markwald, and A. Wessels, “Formation of Myocardium after the Initial Development of the Linear Heart Tube,” *Dev. Biol.*, vol. 240, no. 1, pp. 61–76, Dec. 2001.
- [10] L. A. Taber, I. -En Lin, and E. B. Clark, “Mechanics of cardiac looping,” *Dev. Dyn.*, vol. 203, no. 1, pp. 42–50, 1995.
- [11] A. M. Gerdes, “Cardiac myocyte remodeling in hypertrophy and progression to failure,” *J. Card. Fail.*, vol. 8, no. 6, pp. S264–S268, Dec. 2002.
- [12] B. Swynghedauw, “Molecular Mechanisms of Myocardial Remodeling,” *Physiol. Rev.*, vol. 79, no. 1, pp. 215–262, Jan. 1999.
- [13] M. M. Laks, F. Morady, and H. J. C. Swan, “Canine Right and Left Ventricular Cell and Sarcomere Lengths after Banding the Pulmonary Artery,” *Circ. Res.*, vol. 24, no. 5, pp. 705–710, May 1969.
- [14] P. Kuo *et al.*, “Myocyte Shape Regulates Lateral Registry of Sarcomeres and Contractility,” *Am. J. Pathol.*, vol. 181, no. 6, pp. 2030–2037, Dec. 2012.
- [15] A. J. S. Ribeiro *et al.*, “Contractility of single cardiomyocytes differentiated from pluripotent stem cells depends on physiological shape and substrate stiffness,” *Proc. Natl. Acad. Sci.*, vol. 112, no. 41, pp. 12705–12710, Oct. 2015.
- [16] L. B. Hazeltine *et al.*, “Effects of Substrate Mechanics on Contractility of Cardiomyocytes Generated from Human Pluripotent Stem Cells,” *Int. J. Cell Biol.*, vol. 2012, pp. 1–13, 2012.
- [17] M. Ward, I. A. Williams, Y. Chu, P. J. Cooper, Y. Ju, and D. G. Allen, “Stretch-activated channels in the heart: Contributions to length-dependence and to

- cardiomyopathy,” *Prog. Biophys. Mol. Biol.*, vol. 97, no. 2–3, pp. 232–249, Jun. 2008.
- [18] A. M. Gerdes *et al.*, “Structural remodeling of cardiac myocytes in patients with ischemic cardiomyopathy,” *Circulation*, vol. 86, no. 2, pp. 426–430, Aug. 1992.
- [19] S. Dewan *et al.*, “Model of Human Fetal Growth in Hypoplastic Left Heart Syndrome: Reduced Ventricular Growth Due to Decreased Ventricular Filling and Altered Shape,” *Front. Pediatr.*, vol. 5, p. 25, Feb. 2017.
- [20] A. Meoli *et al.*, “A multiscale model for the study of cardiac biomechanics in single-ventricle surgeries: a clinical case,” *Interface Focus*, vol. 5, no. 2, p. 20140079, Apr. 2015.
- [21] A. de Vecchi *et al.*, “Inflow Typology and Ventricular Geometry Determine Efficiency of Filling in the Hypoplastic Left Heart,” *Ann. Thorac. Surg.*, vol. 94, no. 5, pp. 1562–1569, Nov. 2012.
- [22] E. Kung *et al.*, “Predictive modeling of the virtual Hemi-Fontan operation for second stage single ventricle palliation: Two patient-specific cases,” *J. Biomech.*, vol. 46, no. 2, pp. 423–429, Jan. 2013.
- [23] L. A. Taber, “Biomechanics of Growth, Remodeling, and Morphogenesis,” *Appl. Mech. Rev.*, vol. 48, no. 8, pp. 487–545, Aug. 1995.
- [24] J. Yu and B. Russell, “Cardiomyocyte Remodeling and Sarcomere Addition after Uniaxial Static Strain In Vitro,” *J. Histochem. Cytochem.*, vol. 53, no. 7, pp. 839–844, Jul. 2005.
- [25] H. Yang *et al.*, “Dynamic Myofibrillar Remodeling in Live Cardiomyocytes under Static Stretch,” *Sci. Rep.*, vol. 6, no. 1, p. 20674, Feb. 2016.

- [26] J. D. Humphrey and K. R. Rajagopal, "A Constrained Mixture Model for Growth and Remodeling of Soft Tissues," *Math. Model. Methods Appl. Sci.*, vol. 12, no. 03, pp. 407–430, Mar. 2002.
- [27] Q. S. Li, G. Y. H. Lee, C. N. Ong, and C. T. Lim, "Biochemical and Biophysical Research Communications AFM indentation study of breast cancer cells," *Biochem. Biophys. Res. Commun.*, vol. 374, pp. 609–613, 2008.
- [28] S. Sen, S. Subramanian, and D. E. Discher, "Indentation and Adhesive Probing of a Cell Membrane with AFM : Theoretical Model and Experiments Prototype adhesion," *Biophys. J.*, vol. 89, no. November, pp. 3203–3213, 2005.
- [29] S. Yasuda, D. Townsend, D. E. Michele, E. G. Favre, S. M. Day, and J. M. Metzger, "Dystrophic heart failure blocked by membrane sealant poloxamer," *Nat. Lett.*, vol. 436, no. August, pp. 1025–1029, 2005.
- [30] G. Iribe, M. Helmes, and P. Kohl, "Force-length relations in isolated intact cardiomyocytes subjected to dynamic changes in mechanical load," *Am J Physiol Hear. Circ Physiol*, vol. 292, pp. 1487–1497, 2006.
- [31] S. Nishimura *et al.*, "Single cell mechanics of rat cardiomyocytes under isometric, unloaded, and physiologically loaded conditions," *Am. J. Physiol. Circ. Physiol.*, vol. 287, no. 1, pp. H196–H202, Jul. 2004.
- [32] S. Sugiura, S. Nishimura, S. Yasuda, Y. Hosoya, and K. Katoh, "Carbon fiber technique for the investigation of single-cell mechanics in intact cardiac myocytes," *Nat. Protoc.*, vol. 1, no. 3, pp. 1453–1457, 2006.
- [33] Q. Cheng, Z. Sun, G. Meininger, and M. Almasri, "PDMS elastic micropost arrays for studying vascular smooth muscle cells," *Sensors Actuators B Chem.*, vol. 188,

- no. 573, pp. 1055–1063, Nov. 2013.
- [34] M. L. Rathod, N. Pareek, S. Agrawal, and S. Jaddivada, “RSC Advances Engineered ridge and micropillar array detectors to quantify the directional migration of fibroblasts †,” *R. Soc. Chem.*, vol. 7, pp. 51436–51443, 2017.
- [35] N. Wang, J. P. Butler, and D. E. Ingber, “Mechanotransduction Across the Cell Surface and Through the Cytoskeleton,” *Science (80-.)*, vol. 260, no. 5111, pp. 1124–1127, 1993.
- [36] K. E. Kasza, D. Vader, S. Köster, N. Wang, and D. A. Weitz, “Imaging Techniques for Measuring the Materials Properties of Cells,” *Cold spring Harb. Protoc.*, pp. 380–391, 2010.
- [37] M. L. Rodriguez, P. J. McGarry, and N. J. Sniadecki, “Review on Cell Mechanics: Experimental and Modeling Approaches,” *Appl. Mech. Rev.*, vol. 65, no. 6, Nov. 2013.
- [38] M. S. Sacks and W. Sun, “Multiaxial Mechanical Behavior of Biological Materials,” *Annu. Rev. Biomed. Eng.*, vol. 5, no. 1, pp. 251–284, Aug. 2003.
- [39] P. W. Alford, A. W. Feinberg, S. P. Sheehy, and K. K. Parker, “Biohybrid thin films for measuring contractility in engineered cardiovascular muscle,” *Biomaterials*, vol. 31, no. 13, pp. 3613–3621, May 2010.
- [40] E. S. Hald, K. E. Steucke, J. A. Reeves, Z. Win, and P. W. Alford, “Long-term vascular contractility assay using genipin-modified muscular thin films,” *Biofabrication*, vol. 6, no. 4, p. 045005, Sep. 2014.
- [41] K. E. Steucke, P. V Tracy, E. S. Hald, J. L. Hall, and P. W. Alford, “Vascular smooth muscle cell functional contractility depends on extracellular mechanical

- properties,” *J. Biomech.*, vol. 48, no. 12, pp. 3044–3051, 2015.
- [42] A. W. Feinberg *et al.*, “Controlling the contractile strength of engineered cardiac muscle by hierarchal tissue architecture,” *Biomaterials*, vol. 33, no. 23, pp. 5732–5741, Aug. 2012.
- [43] Y. Sun, R. Duffy, A. Lee, and A. W. Feinberg, “Optimizing the structure and contractility of engineered skeletal muscle thin films,” *Acta Biomater.*, vol. 9, no. 8, pp. 7885–7894, Aug. 2013.
- [44] Z. Win, J. M. Buksa, K. E. Steucke, G. W. Gant Luxton, V. H. Barocas, and P. W. Alford, “Cellular Microbiaxial Stretching to Measure a Single-Cell Strain Energy Density Function,” *J. Biomech. Eng.*, vol. 139, no. 7, pp. 1–10, Jul. 2017.
- [45] T. M. Rothermel, Z. Win, and P. W. Alford, “Large-deformation strain energy density function for vascular smooth muscle cells,” *J. Biomech.*, vol. 111, p. 110005, Oct. 2020.
- [46] L. Bacakova *et al.*, “The Role of Vascular Smooth Muscle Cells in the Physiology and Pathophysiology of Blood Vessels,” in *Muscle Cell and Tissue - Current Status of Research Field*, K. Sakuma, Ed. London: IntechOpen, 2018, pp. 230–257.
- [47] F. V. Brozovich, C. J. Nicholson, C. V. Degen, Y. Z. Gao, M. Aggarwal, and K. G. Morgan, “Mechanisms of Vascular Smooth Muscle Contraction and the Basis for Pharmacologic Treatment of Smooth Muscle Disorders,” *Pharmacol. Rev.*, vol. 68, no. 2, pp. 476–532, Apr. 2016.
- [48] A. Ooshima, G. C. Fuller, G. J. Cardinale, S. Spector, and S. Udenfriend, “Increased Collagen Synthesis in Blood Vessels of Hypertensive Rats and Its

- Reversal by Antihypertensive Agents,” *Proc. Natl. Acad. Sci.*, vol. 71, no. 8, pp. 3019–3023, 1974.
- [49] D. E. Discher, P. Janmey, and Y. Wang, “Tissue Cells Feel and Respond to the Stiffness of Their Substrate,” *Science (80-.)*, vol. 310, no. 5751, pp. 1139–1144, 2005.
- [50] R. H. Cox, “Anisotropic Properties of the Canine Carotid Artery in Vitro,” *J. Biomech.*, vol. 8, pp. 293–300, 1975.
- [51] R. H. Cox, “Arterial wall mechanics and composition muscle activation and the effects of smooth,” *Am. J. Physiol.*, vol. 229, no. 3, pp. 807–812, 1975.
- [52] R. N. Vaishnav, J. T. Young, J. S. Janicki, and D. J. Patel, “Nonlinear Anisotropic Elastic Properties of the Canine Aorta,” *Biophys. J.*, vol. 12, no. 8, pp. 1008–1027, 1972.
- [53] P. B. Dobrin, “Mechanical Properties of Arteries,” *Physiol. Rev.*, vol. 58, no. 2, pp. 397–460, 1978.
- [54] P. B. Dobrin and A. A. Rovick, “Influence contractile of vascular mechanics smooth muscle on of arteries and elasticity,” *Am. J. Physiol.*, vol. 217, no. 6, pp. 1644–1651, 1969.
- [55] R. H. Cox, “Passive mechanics and connective composition of canine arteries,” *Am. J. Physiol. Circ. Physiol.*, vol. 234, no. 5, pp. H533–H541, 1978.
- [56] J. D. Humphrey and K. R. Rajagopal, “A constrained mixture model for arterial adaptations to a sustained step change in blood flow,” *Biomech. Model. Mechanobiol.*, vol. 2, no. 2, pp. 109–126, Nov. 2003.
- [57] P. W. Alford, J. D. Humphrey, and L. A. Taber, “Growth and remodeling in a

- thick-walled artery model: effects of spatial variations in wall constituents,”
Biomech. Model. Mechanobiol., vol. 7, no. 4, pp. 245–262, Aug. 2008.
- [58] J. E. Wagenseil, “A constrained mixture model for developing mouse aorta,”
Biomech. Model. Mechanobiol., vol. 10, no. 5, pp. 671–687, 2011.
- [59] I. Ushiwata and T. Ushiki, “Cytoarchitecture of the smooth muscles and pericytes
of rat cerebral blood vessels,” *J. Neurosurg.*, vol. 73, pp. 82–90, 1990.
- [60] V. Bell *et al.*, “Longitudinal and Circumferential Strain of the Proximal Aorta,” *J.
Am. Heart Assoc.*, vol. 3, no. 6, pp. 1–11, Dec. 2014.
- [61] R. T. Lee *et al.*, “Mechanical Strain Induces Specific Changes in the Synthesis and
Organization of Proteoglycans by Vascular Smooth Muscle Cells,” *J. Biol. Chem.*,
vol. 276, no. 17, pp. 13847–13851, Apr. 2001.
- [62] S. R. Peyton and A. J. Putnam, “Extracellular matrix rigidity governs smooth
muscle cell motility in a biphasic fashion,” *J. Cell. Physiol.*, vol. 204, no. 1, pp.
198–209, Jul. 2005.
- [63] A. M. Collinsworth, S. Zhang, W. E. Kraus, and G. A. Truskey, “Apparent elastic
modulus and hysteresis of skeletal muscle cells throughout differentiation,” *Am. J.
Physiol. Cell Physiol.*, vol. 283, no. 4, pp. C1219–C1227, 2002.
- [64] Y. Bu, L. Li, C. Yang, R. Li, and J. Wang, “Measuring Viscoelastic Properties of
Living Cells,” *Acta Mech. Solida Sin.*, vol. 32, no. 5, pp. 599–610, 2019.
- [65] K. Sethi, E. J. Cram, and R. Zaidel-Bar, “Stretch-induced actomyosin contraction
in epithelial tubes: mechanotransduction pathways for tubular homeostasis,”
Semin. Cell Dev. Biol., vol. 71, pp. 146–152, 2017.
- [66] K. E. Steucke, Z. Win, T. R. Stemler, E. E. Walsh, J. L. Hall, and P. W. Alford,

- “Empirically Determined Vascular Smooth Muscle Cell Mechano-Adaptation Law,” *J. Biomech. Eng.*, vol. 139, no. 7, pp. 1–9, Jul. 2017.
- [67] S. Nawaz, P. Sánchez, K. Bodensiek, S. Li, M. Simons, and I. A. T. Schaap, “Cell Visco-Elasticity Measured with AFM and Optical Trapping at Sub-Micrometer Deformations,” *PLoS One*, vol. 7, no. 9, p. e45297, 2012.
- [68] M. Radmacher, R. Tillamnn, M. Fritz, and H. Gaub, “From molecules to cells: imaging soft samples with the atomic force microscope,” *Science (80-.)*, vol. 257, no. 5078, pp. 1900–1905, Sep. 1992.
- [69] G. N. Maksym *et al.*, “Mechanical properties of cultured human airway smooth muscle cells from 0.05 to 0.4 Hz,” *J. Appl. Physiol.*, vol. 89, no. 4, pp. 1619–1632, Oct. 2000.
- [70] V. M. Laurent *et al.*, “Assessment of Mechanical Properties of Adherent Living Cells by Bead Micromanipulation: Comparison of Magnetic Twisting Cytometry vs Optical Tweezers,” *J. Biomech. Eng.*, vol. 124, no. 4, pp. 408–421, Aug. 2002.
- [71] Z. Win, J. M. Buksa, and P. W. Alford, “Architecture-Dependent Anisotropic Hysteresis in Smooth Muscle Cells,” *Biophys. J.*, vol. 115, no. 10, pp. 2044–2054, Nov. 2018.
- [72] G. J. C. Ye, Y. Aratyn-schaus, A. P. Nesmith, F. S. Pasqualini, P. W. Alford, and Kevin, “The contractile strength of vascular smooth muscle myocytes is shape dependent,” *Integr. Biol.*, vol. 6, no. 2, pp. 152–163, 2014.
- [73] P. W. Alford, A. P. Nesmith, J. N. Seywerd, A. Grosberg, and K. K. Parker, “Vascular smooth muscle contractility depends on cell shape,” *Integr. Biol.*, vol. 3, no. 11, pp. 1063–1070, Nov. 2011.

- [74] Q. Tseng *et al.*, “Spatial organization of the extracellular matrix regulates cell-cell junction positioning,” *Proc. Natl. Acad. Sci.*, vol. 109, no. 5, pp. 1506–1511, Jan. 2012.
- [75] D. Volfson, S. Cookson, J. Hasty, and L. S. Tsimring, “Biomechanical ordering of dense cell populations,” *Proc. Natl. Acad. Sci.*, vol. 105, no. 40, pp. 15346–15351, 2008.
- [76] M. Bray, S. P. Sheehy, and K. K. Parker, “Sarcomere Alignment is Regulated by Myocyte Shape,” *Cell Motil. Cytoskeleton*, vol. 65, no. 8, pp. 641–651, 2008.
- [77] P. Berens, “CircStat: A Matlab Toolbox for Circular Statistics,” *J. Stat. Softw.*, vol. 31, no. 10, 2009.
- [78] T. C. Gasser, R. W. Ogden, and G. A. Holzapfel, “Hyperelastic modelling of arterial layers with distributed collagen fibre orientations,” *J. R. Soc. Interface*, vol. 3, no. 6, pp. 15–35, Feb. 2006.
- [79] P. W. Oakes, S. Banerjee, M. C. Marchetti, and M. L. Gardel, “Geometry Regulates Traction Stresses in Adherent Cells,” *Biophys. J.*, vol. 107, no. 4, pp. 825–833, Aug. 2014.
- [80] K. K. Parker *et al.*, “Directional control of lamellipodia extension by constraining cell shape and orienting cell tractional forces,” *FASEB J.*, vol. 16, no. 10, pp. 1195–1204, 2002.
- [81] J. D. Humphrey, D. L. Vawter, and R. P. Vito, “Quantification of strains in biaxially tested soft tissues,” *J. Biomech.*, vol. 20, no. 1, pp. 59–65, 1987.
- [82] Y. Lanir and Y. C. Fung, “Two-Dimensional Mechanical Properties of Rabbit Skin-II Experimental Results,” *J. Biomech.*, vol. 7, no. 2, pp. 171–182, 1974.

- [83] Y. Lanir, O. Lichtenstein, and O. Imanuel, "Optimal Design of Biaxial Tests for Structural Material Characterization of Flat Tissues," *J. Biomech. Eng.*, vol. 118, pp. 41–47, 1996.
- [84] J. O. V. Delgadillo, S. Delorme, F. Thibault, R. DiRaddo, and S. G. Hatzikiriakos, "Large Deformation Characterization of Porcine Thoracic Aortas : Inverse Modeling Fitting of Uniaxial and Biaxial Tests," *J. Biomed. Sci. Eng.*, vol. 8, no. 10, pp. 717–732, 2015.
- [85] C. M. Witzenburg *et al.*, "Failure of the Porcine Ascending Aorta : Multidirectional Experiments and a Unifying Microstructural Model," *J. Biomech. Eng.*, vol. 139, no. 3, pp. 1–14, 2017.
- [86] F. Gervaso, C. Capelli, L. Petrini, S. Lattanzio, L. Di Virgilio, and F. Migliavacca, "On the effects of different strategies in modelling balloon-expandable stenting by means of finite element method," *J. Biomech.*, vol. 41, no. 6, pp. 1206–1212, 2008.
- [87] G. A. Holzapfel and T. C. Gasser, "Computational stress-deformation analysis of arterial walls including high-pressure response," *Int. J. Cardiol.*, vol. 116, no. 1, pp. 78–85, 2007.
- [88] P. W. Alford, B. E. Dabiri, J. A. Goss, M. A. Hemphill, M. D. Brigham, and K. K. Parker, "Blast-induced phenotypic switching in cerebral vasospasm," *Proc. Natl. Acad. Sci.*, vol. 108, no. 31, pp. 12705–12710, Aug. 2011.
- [89] A. Ray *et al.*, "Anisotropic forces from spatially constrained focal adhesions mediate contact guidance directed cell migration," *Nat. Commun.*, vol. 8, no. 1, p. 14923, Apr. 2017.
- [90] Z. Win, G. D. Vrla, K. E. Steucke, E. N. Sevcik, E. S. Hald, and P. W. Alford,

- “Smooth muscle architecture within cell-dense vascular tissues influences functional contractility,” *Integr. Biol.*, vol. 6, no. 12, pp. 1201–1210, Oct. 2014.
- [91] X. Jiang, D. A. Bruzewicz, A. P. Wong, M. Piel, and G. M. Whitesides, “Directing cell migration with asymmetric micropatterns,” *Proc. Natl. Acad. Sci.*, vol. 102, no. 4, pp. 975–978, 2005.
- [92] M. Thery, A. Pepin, E. Dressaire, Y. Chen, and M. Bornens, “Cell Distribution of Stress Fibres in Response to the Geometry of the Adhesive Environment,” *Cell Motil. Cytoskeleton*, vol. 63, no. 6, pp. 341–355, 2006.
- [93] D. Wang *et al.*, “Tissue-specific mechanical and geometrical control of cell viability and actin cytoskeleton alignment,” *Sci. Rep.*, vol. 4, no. 6160, pp. 1–6, 2014.
- [94] F. Li, B. Li, Q. M. Wang, and J. H. C. Wang, “Cell shape regulates collagen type I expression in human tendon fibroblasts,” *Cell Motil. Cytoskeleton*, vol. 65, no. 4, pp. 332–341, 2008.
- [95] M. L. Gardel, J. H. Shin, F. C. MacKintosh, L. Mahadevan, P. Matsudaira, and D. A. Weitz, “Elastic Behavior of Cross-Linked and Bundled Actin Networks,” *Science (80-.)*, vol. 304, no. 5675, pp. 1301–1306, 2004.
- [96] S. Hadjiantoniou, L. Guolla, and A. E. Pelling, “Mechanically induced deformation and strain dynamics in actin stress fibers,” *Commun. Integr. Biol.*, vol. 5, no. 6, pp. 627–630, 2012.
- [97] L. Guolla, M. Bertrand, K. Haase, and A. E. Pelling, “Force transduction and strain dynamics in actin stress fibres in response to nanonewton forces,” *J. Cell Sci.*, vol. 125, no. 3, pp. 603–613, 2012.

- [98] N. Wang and D. Stamenović, “Contribution of intermediate filaments to cell stiffness, stiffening, and growth,” *Am. J. Physiol. - Cell Physiol.*, vol. 279, no. 1, pp. 188–194, 2000.
- [99] D. M. Toivola, P. Strnad, A. Habtezion, and M. B. Omary, “Intermediate filaments take the heat as stress proteins,” *Trends Cell Biol.*, vol. 20, no. 2, pp. 79–91, 2010.
- [100] J. Hu *et al.*, “High stretchability, strength, and toughness of living cells enabled by hyperelastic vimentin intermediate filaments,” *Proc. Natl. Acad. Sci. U. S. A.*, vol. 116, no. 35, pp. 17175–17180, 2019.
- [101] P. A. Janmey, U. Euteneuer, P. Traub, and M. Schliwa, “Viscoelastic properties of vimentin compared with other filamentous biopolymer networks,” *J. Cell Biol.*, vol. 113, no. 1, pp. 155–160, 1991.
- [102] H. Ladjal, J. Hanus, A. Pillarisetti, C. Keefer, A. Ferreira, and J. P. Desai, “Atomic force microscopy-based single-cell indentation: Experimentation and finite element simulation,” in *2009 IEEE/RSJ International Conference on Intelligent Robots and Systems*, 2009, pp. 1326–1332.
- [103] K. B. Bernick, T. P. Prevost, S. Suresh, and S. Socrate, “Biomechanics of single cortical neurons,” *Acta Biomater.*, vol. 7, no. 3, pp. 1210–1219, Mar. 2011.
- [104] M. Sato, K. Nagayama, N. Kataoka, M. Sasaki, and K. Hane, “Local mechanical properties measured by atomic force microscopy for cultured bovine endothelial cells exposed to shear stress,” *J. Biomech.*, vol. 33, no. 1, pp. 127–135, 2000.
- [105] M. Sato, N. Ohshima, and R. M. Nerem, “Viscoelastic properties of cultured porcine aortic endothelial cells exposed to shear stress,” *J. Biomech.*, vol. 29, no. 4, pp. 461–467, Apr. 1996.

- [106] S. Motte and L. J. Kaufman, “Strain Stiffening in Collagen I Networks,” *Biopolymers*, vol. 99, no. 1, pp. 35–46, 2013.
- [107] T. C. Gasser, S. Gallinetti, X. Xing, C. Forsell, J. Swedenborg, and J. Roy, “Spatial orientation of collagen fibers in the abdominal aortic aneurysm’s wall and its relation to wall mechanics,” *Acta Biomater.*, vol. 8, no. 8, pp. 3091–3103, 2012.
- [108] V. S. Deshpande, R. M. McMeeking, and A. G. Evans, “A bio-chemo-mechanical model for cell contractility,” *Proc. Natl. Acad. Sci.*, vol. 103, no. 38, pp. 14015–14020, 2006.
- [109] J. P. McGarry *et al.*, “Simulation of the contractile response of cells on an array of micro-posts,” *Philos. Trans. R. Soc. A Math. Phys. Eng. Sci.*, vol. 367, no. 1902, pp. 3477–3497, Sep. 2009.
- [110] R. Teixeira *et al.*, “Circumferential vascular strain rate to estimate vascular load in aortic stenosis: a speckle tracking echocardiography study,” *Int. J. Cardiovasc. Imaging*, vol. 31, no. 4, pp. 681–689, 2015.
- [111] J. Wan, F. He, Y. Zhao, H. Zhang, X. Zhou, and M. Wan, “Non-invasive Vascular Radial/Circumferential Strain Imaging and Wall Shear Rate Estimation Using Video Images of Diagnostic Ultrasound,” *Ultrasound Med. Biol.*, vol. 40, no. 3, pp. 622–636, 2014.
- [112] J. H. Haga, Y. J. Li, and S. Chien, “Molecular basis of the effects of mechanical stretch on vascular smooth muscle cells,” *J. Biomech.*, vol. 40, no. 5, pp. 947–960, Jan. 2007.
- [113] K. G. Birukov *et al.*, “Stretch affects phenotype and proliferation of vascular smooth muscle cells,” *Mol. Cell. Biochem.*, vol. 144, no. 2, pp. 131–139, 1995.

- [114] P. R. Standley, A. Camaratta, B. P. Nolan, C. T. Purgason, and M. A. Stanley, “Cyclic stretch induces vascular smooth muscle cell alignment via NO signaling,” *Am. J. Physiol. Circ. Physiol.*, vol. 283, no. 5, pp. H1907–H1914, Nov. 2002.
- [115] E. S. Hald and P. W. Alford, “Smooth Muscle Phenotype Switching in Blast Traumatic Brain Injury-Induced Cerebral Vasospasm,” *Transl. Stroke Res.*, vol. 5, no. 3, pp. 385–393, 2014.
- [116] C. A. Lemarié, P. Tharaux, and S. Lehoux, “Extracellular matrix alterations in hypertensive vascular remodeling,” *J. Mol. Cell. Cardiol.*, vol. 48, no. 3, pp. 433–439, 2010.
- [117] T. Rothermel, I. Franczek, and P. Alford, “Anisotropic Mechanics of Vascular Smooth Muscle Cells Exposed to Dynamic Loads,” *J. Biomech. Eng.*, vol. 123, no. 12, Aug. 2021.
- [118] M. T. Draney *et al.*, “Quantification of Vessel Wall Cyclic Strain Using Cine Phase Contrast Magnetic Resonance Imaging,” *Ann. Biomed. Eng.*, vol. 30, no. 8, pp. 1033–1045, Sep. 2002.
- [119] B. C. Isenberg, P. A. DiMilla, M. Walker, S. Kim, and J. Y. Wong, “Vascular Smooth Muscle Cell Durotaxis Depends on Substrate Stiffness Gradient Strength,” *Biophys. J.*, vol. 97, no. 5, pp. 1313–1322, Sep. 2009.
- [120] D. P. McDaniel *et al.*, “The Stiffness of Collagen Fibrils Influences Vascular Smooth Muscle Cell Phenotype,” *Biophys. J.*, vol. 92, no. 5, pp. 1759–1769, Mar. 2007.
- [121] H. Iwasaki, S. Eguchi, H. Ueno, F. Marumo, and Y. Hirata, “Mechanical stretch stimulates growth of vascular smooth muscle cells via epidermal growth factor

- receptor,” *Am. J. Physiol. - Hear. Circ. Physiol.*, vol. 278, no. 2 47-2, pp. 521–529, 2000.
- [122] C. Li, F. Wernig, M. Leitges, Y. Hu, and Q. Xu, “Mechanical stress-activated PKC δ regulates smooth muscle cell migration,” *FASEB J.*, vol. 17, no. 14, pp. 1–21, Nov. 2003.
- [123] Q. Chen, W. Li, Z. Quan, and B. E. Sumpio, “Modulation of vascular smooth muscle cell alignment by cyclic strain is dependent on reactive oxygen species and P38 mitogen-activated protein kinase,” *J. Vasc. Surg.*, vol. 37, no. 3, pp. 660–668, 2003.
- [124] P. Kollmannsberger, C. T. Mierke, and B. Fabry, “Nonlinear viscoelasticity of adherent cells is controlled by cytoskeletal tension,” *Soft Matter*, vol. 7, no. 7, pp. 3127–3132, 2011.
- [125] F. M. Hecht, J. Rheinlaender, N. Schierbaum, W. H. Goldmann, B. Fabry, and T. E. Schäffer, “Imaging viscoelastic properties of live cells by AFM: power-law rheology on the nanoscale,” *Soft Matter*, vol. 11, no. 23, pp. 4584–4591, 2015.
- [126] J. Alcaraz *et al.*, “Microrheology of human lung epithelial cells measured by atomic force microscopy,” *Biophys. J.*, vol. 84, no. 3, pp. 2071–2079, Mar. 2003.
- [127] L. Deng *et al.*, “Fast and slow dynamics of the cytoskeleton,” *Nat. Mater.*, vol. 5, no. 8, pp. 636–640, Aug. 2006.
- [128] S. C. W. Tan, W. X. Pan, G. Ma, N. Cai, K. W. Leong, and K. Liao, “Viscoelastic behaviour of human mesenchymal stem cells,” *BMC Cell Biol.*, vol. 9, no. 1, p. 40, 2008.
- [129] Y.-B. Lu *et al.*, “Viscoelastic properties of individual glial cells and neurons in the

- CNS,” *Proc. Natl. Acad. Sci.*, vol. 103, no. 47, pp. 17759–17764, Nov. 2006.
- [130] X. Trepap, M. Grabulosa, F. Puig, G. N. Maksym, D. Navajas, and R. Farré, “Viscoelasticity of human alveolar epithelial cells subjected to stretch,” *Am. J. Physiol. Cell. Mol. Physiol.*, vol. 287, no. 5, pp. L1025–L1034, Nov. 2004.
- [131] N. Bonakdar *et al.*, “Mechanical plasticity of cells,” *Nat. Mater.*, vol. 15, no. 10, pp. 1090–1094, 2016.
- [132] M. Puig-de-Morales-Marinkovic, K. T. Turner, J. P. Butler, J. J. Fredberg, and S. Suresh, “Viscoelasticity of the human red blood cell,” *Am. J. Physiol. - Cell Physiol.*, vol. 293, no. 2, pp. 597–605, 2007.
- [133] A. R. Bausch, W. Möller, and E. Sackmann, “Measurement of Local Viscoelasticity and Forces in Living Cells by Magnetic Tweezers,” *Biophys. J.*, vol. 76, no. 1, pp. 573–579, Jan. 1999.
- [134] A. R. Bausch, F. Ziemann, A. A. Boulbitch, K. Jacobson, and E. Sackmann, “Local Measurements of Viscoelastic Parameters of Adherent Cell Surfaces by Magnetic Bead Microrheometry,” *Biophys. J.*, vol. 75, no. 4, pp. 2038–2049, Oct. 1998.
- [135] S. Moreno-Flores, R. Benitez, M. dM Vivanco, and J. L. Toca-Herrera, “Stress relaxation and creep on living cells with the atomic force microscope: a means to calculate elastic moduli and viscosities of cell components,” *Nanotechnology*, vol. 21, no. 44, p. 445101, Nov. 2010.
- [136] S. Moreno-Flores, R. Benitez, M. dM Vivanco, and J. L. Toca-Herrera, “Stress relaxation microscopy: Imaging local stress in cells,” *J. Biomech.*, vol. 43, no. 2, pp. 349–354, Jan. 2010.

- [137] T. Okajima *et al.*, “Stress relaxation of HepG2 cells measured by atomic force microscopy,” *Nanotechnology*, vol. 18, no. 8, p. 084010, Feb. 2007.
- [138] X. Trepap *et al.*, “Universal physical responses to stretch in the living cell,” *Nature*, vol. 447, no. 7144, pp. 592–595, 2007.
- [139] C. A. Putman, K. O. van der Werf, B. G. de Groot, N. F. van Hulst, and J. Greve, “Viscoelasticity of living cells allows high resolution imaging by tapping mode atomic force microscopy,” *Biophys. J.*, vol. 67, no. 4, pp. 1749–1753, 1994.
- [140] A. V. Hill, “The heat of shortening and the dynamic constants of muscle,” *Proc. R. Soc. London. Ser. B - Biol. Sci.*, vol. 126, no. 843, pp. 136–195, Oct. 1938.
- [141] R. L. Armentano, J. G. Barra, J. Levenson, A. Simon, and R. H. Pichel, “Arterial Wall Mechanics in Conscious Dogs,” *Circ. Res.*, vol. 76, no. 3, pp. 468–478, Mar. 1995.
- [142] M. Goto and Y. Kimoto, “Hysteresis and Stress-Relaxation of the Blood Vessels Studied by a Universal Tensile Testing Instrument,” *Jpn. J. Physiol.*, vol. 16, no. 2, pp. 169–184, 1966.
- [143] G. A. Holzapfel, G. Sommer, C. T. Gasser, and P. Regitnig, “Determination of layer-specific mechanical properties of human coronary arteries with nonatherosclerotic intimal thickening and related constitutive modeling,” *Am. J. Physiol. Circ. Physiol.*, vol. 289, no. 5, pp. H2048–H2058, Nov. 2005.
- [144] P. Dobrin and A. Rovick, “Influence of vascular smooth muscle on contractile mechanics and elasticity of arteries,” *Am. J. Physiol. Content*, vol. 217, no. 6, pp. 1644–1651, Dec. 1969.
- [145] M. Sato and N. Ohshima, “Nonlinear viscoelastic behaviour of canine arterial

- walls,” *Med. Biol. Eng. Comput.*, vol. 23, no. 6, pp. 565–571, Nov. 1985.
- [146] M. Zatzman, R. W. Stacy, J. Randall, and A. Eberstein, “Time Course of Stress Relaxation in Isolated Arterial Segments,” *Am. J. Physiol. Content*, vol. 177, no. 2, pp. 299–302, May 1954.
- [147] D. Craiem, F. J. Rojo, J. M. Atienza, R. L. Armentano, and G. V. Guinea, “Fractional-order viscoelasticity applied to describe uniaxial stress relaxation of human arteries,” *Phys. Med. Biol.*, vol. 53, no. 17, pp. 4543–4554, 2008.
- [148] J. T. Young, R. N. Vaishnav, and D. J. Patel, “Nonlinear anisotropic viscoelastic properties of canine arterial segments,” *J. Biomech.*, vol. 10, no. 9, pp. 549–559, Jan. 1977.
- [149] A. I. Veress *et al.*, “Vascular mechanics of the coronary artery.,” *Z. Kardiol.*, vol. 89 Suppl 2, no. 14, pp. 92–100, Feb. 2000.
- [150] Q. Yu, J. Zhou, and Y. C. Fung, “Neutral axis location in bending and Young’s modulus of different layers of arterial wall,” *Am. J. Physiol. Circ. Physiol.*, vol. 265, no. 1, pp. H52–H60, Jul. 1993.
- [151] S. Q. Liu and Y. C. Fung, “Relationship Between Hypertension, Hypertrophy, and Opening Angle of Zero-Stress State of Arteries Following Aortic Constriction,” *J. Biomech. Eng.*, vol. 111, no. 4, pp. 325–335, Nov. 1989.
- [152] D. Li, D. Xu, P. Li, J. Wei, K. Yang, and C. Zhao, “Viscoelastic evaluation of fetal umbilical vein for reconstruction of middle cerebral artery.,” *Neural Regen. Res.*, vol. 8, no. 32, pp. 3055–62, Nov. 2013.
- [153] E. J. Koay, A. C. Shieh, and K. A. Athanasiou, “Creep Indentation of Single Cells,” *J. Biomech. Eng.*, vol. 125, no. 3, pp. 334–341, Jun. 2003.

- [154] G. Lenormand, E. Millet, B. Fabry, J. P. Butler, and J. J. Fredberg, “Linearity and time-scale invariance of the creep function in living cells,” *J. R. Soc. Interface*, vol. 1, no. 1, pp. 91–97, Nov. 2004.
- [155] N. Desprat, A. Richert, J. Simeon, and A. Asnacios, “Creep Function of a Single Living Cell,” *Biophys. J.*, vol. 88, no. 3, pp. 2224–2233, Mar. 2005.
- [156] E. M. Darling, S. Zauscher, and F. Guilak, “Viscoelastic properties of zonal articular chondrocytes measured by atomic force microscopy,” *Osteoarthr. Cartil.*, vol. 14, no. 6, pp. 571–579, Jun. 2006.
- [157] E. M. Darling, S. Zauscher, J. A. Block, and F. Guilak, “A Thin-Layer Model for Viscoelastic, Stress-Relaxation Testing of Cells Using Atomic Force Microscopy: Do Cell Properties Reflect Metastatic Potential?,” *Biophys. J.*, vol. 92, no. 5, pp. 1784–1791, Mar. 2007.
- [158] J. D. Hemmer, J. Nagatomi, S. T. Wood, A. A. Vertegel, D. Dean, and M. LaBerge, “Role of Cytoskeletal Components in Stress-Relaxation Behavior of Adherent Vascular Smooth Muscle Cells,” *J. Biomech. Eng.*, vol. 131, no. 4, pp. 1–9, Apr. 2009.
- [159] Y. Bu, L. Li, and J. Z. Wang, “Power law creep and relaxation with the atomic force microscope: Determining viscoelastic property of living cells,” *Sci. China Technol. Sci.*, vol. 62, no. 5, pp. 781–786, 2019.
- [160] J. J. Muñoz and S. Albo, “Physiology-based model of cell viscoelasticity,” *Phys. Rev. E - Stat. Nonlinear, Soft Matter Phys.*, vol. 88, no. 1, pp. 1–8, 2013.
- [161] V. B. Shenoy, H. Wang, and X. Wang, “A chemo-mechanical free-energy-based approach to model durotaxis and extracellular stiffness-dependent contraction and

- polarization of cells,” *Interface Focus*, vol. 6, no. 1, p. 20150067, Feb. 2016.
- [162] P. Moreo, J. M. García-Aznar, and M. Doblaré, “Modeling mechanosensing and its effect on the migration and proliferation of adherent cells,” *Acta Biomater.*, vol. 4, no. 3, pp. 613–621, May 2008.
- [163] G. S. Rosalem, E. B. Las Casas, T. P. Lima, and L. A. González-Torres, “A mechanobiological model to study upstream cell migration guided by tensotaxis,” *Biomech. Model. Mechanobiol.*, vol. 19, no. 5, pp. 1537–1549, Oct. 2020.
- [164] M.-C. Kim, D. M. Neal, R. D. Kamm, and H. H. Asada, “Dynamic Modeling of Cell Migration and Spreading Behaviors on Fibronectin Coated Planar Substrates and Micropatterned Geometries,” *PLoS Comput. Biol.*, vol. 9, no. 2, p. e1002926, Feb. 2013.
- [165] F. J. Vernerey and M. Farsad, “A mathematical model of the coupled mechanisms of cell adhesion, contraction and spreading,” *J. Math. Biol.*, vol. 68, no. 4, pp. 989–1022, Mar. 2014.
- [166] Z. Wei, V. S. Deshpande, R. M. McMeeking, and A. G. Evans, “Analysis and Interpretation of Stress Fiber Organization in Cells Subject to Cyclic Stretch,” *J. Biomech. Eng.*, vol. 130, no. 3, Jun. 2008.
- [167] W. Carver, M. L. Nagpal, M. Nachtigal, T. K. Borg, and L. Terracio, “Collagen expression in mechanically stimulated cardiac fibroblasts,” *Circ. Res.*, vol. 69, no. 1, pp. 116–122, 1991.
- [168] T. R. Olsen *et al.*, “Longitudinal stretching for maturation of vascular tissues using magnetic forces,” *Bioengineering*, vol. 3, no. 4, pp. 1–14, 2016.
- [169] B. E. Sumpio, A. J. Banes, M. Buckley, and G. Johnson, “Alterations in aortic

- endothelial cell morphology and cytoskeletal protein synthesis during cyclic tensional deformation,” *J. Vasc. Surg.*, vol. 7, no. 1, pp. 130–138, 1988.
- [170] D. Y. M. Leung, S. Glagov, and M. B. Mathews, “A new in vitro system for studying cell response to mechanical stimulation,” *Exp. Cell Res.*, vol. 109, no. 2, pp. 285–298, 1977.
- [171] J. Yan *et al.*, “Cyclic Stretch Induces Vascular Smooth Muscle Cells to Secrete Connective Tissue Growth Factor and Promote Endothelial Progenitor Cell Differentiation and Angiogenesis,” *Front. Cell Dev. Biol.*, vol. 8, no. December, pp. 1–15, Dec. 2020.
- [172] G. C. Cheng *et al.*, “Mechanical Strain Tightly Controls Fibroblast Growth Factor-2 Release From Cultured Human Vascular Smooth Muscle Cells,” *Circ. Res.*, vol. 80, no. 1, pp. 28–36, Jan. 1997.
- [173] E. Wilson, Q. Mai, K. Sudhir, R. H. Weiss, and H. E. Ives, “Mechanical strain induces growth of vascular smooth muscle cells via autocrine action of PDGF,” *J. Cell Biol.*, vol. 123, no. 3, pp. 741–747, 1993.
- [174] S. Ghazanfari, M. Tafazzoli-Shadpour, and M. A. Shokrgozar, “Effects of cyclic stretch on proliferation of mesenchymal stem cells and their differentiation to smooth muscle cells,” *Biochem. Biophys. Res. Commun.*, vol. 388, no. 3, pp. 601–605, 2009.
- [175] N. Shimizu *et al.*, “Cyclic strain induces mouse embryonic stem cell differentiation into vascular smooth muscle cells by activating PDGF receptor β ,” *J. Appl. Physiol.*, vol. 104, no. 3, pp. 766–772, 2008.
- [176] H. Wang, W. Ip, R. Boissy, and E. S. Grood, “Cell orientation response to

- cyclically deformed substrates: Experimental validation of a cell model,” *J. Biomech.*, vol. 28, no. 12, pp. 1543–1552, 1995.
- [177] P. C. Dartsch and E. Betz, “Response of cultured endothelial cells to mechanical stimulation,” *Basic Res. Cardiol.*, vol. 84, no. 3, pp. 268–281, 1989.
- [178] P. C. Dartsch, H. Hammerle, and E. Betz, “Orientation of cultured arterial smooth muscle cells growing on cyclically stretched substrates,” *Acta Anat. (Basel)*, vol. 125, no. 2, pp. 108–113, 1986.
- [179] J. H. C. Wang, “Substrate deformation determines actin cytoskeleton reorganization: A mathematical modeling and experimental study,” *J. Theor. Biol.*, vol. 202, no. 1, pp. 33–41, 2000.
- [180] C. Neidlinger-Wilke, E. S. Grood, J. H. C. Wang, R. A. Brand, and L. Claes, “Cell alignment is induced by cyclic changes in cell length: Studies of cells grown in cyclically stretched substrates,” *J. Orthop. Res.*, vol. 19, no. 2, pp. 286–293, 2001.
- [181] R. C. Buck, “Reorientation response of cells to repeated stretch and recoil of the substratum,” *Exp. Cell Res.*, vol. 127, no. 2, pp. 470–474, 1980.
- [182] A. M. Greiner, H. Chen, J. P. Spatz, and R. Kemkemer, “Cyclic Tensile Strain Controls Cell Shape and Directs Actin Stress Fiber Formation and Focal Adhesion Alignment in Spreading Cells,” *PLoS One*, vol. 8, no. 10, 2013.
- [183] Y. Cui *et al.*, “Cyclic stretching of soft substrates induces spreading and growth,” *Nat. Commun.*, vol. 6, pp. 1–8, 2015.
- [184] Fu, Liu, Halim, Ju, Luo, and Song, “Mesenchymal Stem Cell Migration and Tissue Repair,” *Cells*, vol. 8, no. 8, p. 784, 2019.
- [185] K. Nagayama, Y. Suzuki, and D. Fujiwara, “Directional dependence of cyclic

- stretch-induced cell migration in wound healing process of monolayer cells,” *Adv. Biomed. Eng.*, vol. 8, pp. 163–169, 2019.
- [186] B. Zhang *et al.*, “Cyclic mechanical stretching promotes migration but inhibits invasion of rat bone marrow stromal cells,” *Stem Cell Res.*, vol. 14, no. 2, pp. 155–164, 2015.
- [187] S. Na, A. Trache, J. Trzeciakowski, Z. Sun, G. A. Meininger, and J. D. Humphrey, “Time-dependent changes in smooth muscle cell stiffness and focal adhesion area in response to cyclic equibiaxial stretch,” *Ann. Biomed. Eng.*, vol. 36, no. 3, pp. 369–380, 2008.
- [188] V. S. Deshpande, M. Mrksich, R. M. McMeeking, and A. G. Evans, “A bio-mechanical model for coupling cell contractility with focal adhesion formation,” *J. Mech. Phys. Solids*, vol. 56, no. 4, pp. 1484–1510, 2008.
- [189] P. W. Alford and L. A. Taber, “Computational study of growth and remodelling in the aortic arch,” *Comput. Methods Biomech. Biomed. Engin.*, vol. 11, no. 5, pp. 525–538, Oct. 2008.
- [190] L. A. Taber and J. D. Humphrey, “Stress-modulated growth, residual stress, and vascular heterogeneity,” *J. Biomech. Eng.*, vol. 123, no. 6, pp. 528–535, 2001.
- [191] L. A. Taber, “A model for aortic growth based on fluid shear and fiber stresses,” *J. Biomech. Eng.*, vol. 120, no. 3, pp. 348–354, 1998.
- [192] L. A. Taber and D. W. Eggers, “Theoretical study of stress-modulated growth in the aorta,” *J. Theor. Biol.*, vol. 180, no. 4, pp. 343–357, 1996.
- [193] B. L. Cook, C. J. Chau, and P. W. Alford, “Architecture-Dependent Mechano-Adaptation in Single Vascular Smooth Muscle Cells,” *J. Biomech. Eng.*, vol. 143,

no. 10, pp. 1–10, Oct. 2021.

- [194] C. L. Dinardo *et al.*, “Variation of mechanical properties and quantitative proteomics of VSMC along the arterial tree,” *Am. J. Physiol. - Hear. Circ. Physiol.*, vol. 306, no. 4, pp. 505–516, 2014.
- [195] S. S. M. Rensen, P. A. F. M. Doevendans, and G. J. J. M. Van Eys, “Regulation and characteristics of vascular smooth muscle cell phenotypic diversity,” *Netherlands Hear. J.*, vol. 15, no. 3, pp. 100–108, 2007.
- [196] H. Miyazaki, Y. Hasegawa, and K. Hayashi, “Tensile Properties of Contractile and Synthetic Vascular Smooth Muscle Cells,” *JSME Int. J. Ser. C Mech. Syst. Mach. Elem. Manuf.*, vol. 45, no. 4, pp. 870–879, 2002.
- [197] M. Han, J. K. Wen, B. Zheng, Y. Cheng, and C. Zhang, “Serum deprivation results in redifferentiation of human umbilical vascular smooth muscle cells,” *Am. J. Physiol. - Cell Physiol.*, vol. 291, no. 1, pp. 50–58, 2006.
- [198] B. A. Smith, B. Tolloczko, J. G. Martin, and P. Grütter, “Probing the Viscoelastic Behavior of Cultured Airway Smooth Muscle Cells with Atomic Force Microscopy: Stiffening Induced by Contractile Agonist,” *Biophys. J.*, vol. 88, no. 4, pp. 2994–3007, Apr. 2005.
- [199] B. Fabry *et al.*, “Selected Contribution: Time course and heterogeneity of contractile responses in cultured human airway smooth muscle cells,” *J. Appl. Physiol.*, vol. 91, no. 2, pp. 986–994, Aug. 2001.
- [200] D. Liao, C. Sevcencu, K. Yoshida, and H. Gregersen, “Viscoelastic properties of isolated rat colon smooth muscle cells,” *Cell Biol. Int.*, vol. 30, no. 10, pp. 854–858, Oct. 2006.

- [201] G. L. Clark *et al.*, “Smooth muscle regional contribution to vaginal wall function,” *Interface Focus*, vol. 9, no. 4, p. 20190025, Aug. 2019.
- [202] J. P. S. Ferreira *et al.*, “Altered mechanics of vaginal smooth muscle cells due to the lysyl oxidase-like 1 knockout,” *Acta Biomater.*, vol. 110, pp. 175–187, Jul. 2020.
- [203] A. Pathak, V. S. Deshpande, R. M. McMeeking, and A. G. Evans, “The simulation of stress fibre and focal adhesion development in cells on patterned substrates,” *J. R. Soc. Interface*, vol. 5, no. 22, pp. 507–524, May 2008.
- [204] C. E. Chan and D. J. Odde, “Traction Dynamics of Filopodia on Compliant Substrates,” *Science (80-.)*, vol. 322, no. 5908, pp. 1687–1691, Dec. 2008.
- [205] J. U. Voigt and M. Cvijic, “2- and 3-Dimensional Myocardial Strain in Cardiac Health and Disease,” *JACC Cardiovasc. Imaging*, vol. 12, no. 9, pp. 1849–1863, 2019.
- [206] B. Brady, G. King, R. T. Murphy, and D. Walsh, “Myocardial strain: a clinical review,” *Irish J. Med. Sci. (1971 -)*, vol. 192, no. 4, pp. 1649–1656, Aug. 2023.
- [207] W. M. Torres *et al.*, “Regional and temporal changes in left ventricular strain and stiffness in a porcine model of myocardial infarction,” *Am. J. Physiol. Circ. Physiol.*, vol. 315, no. 4, pp. H958–H967, Oct. 2018.
- [208] A. Rösner *et al.*, “Changes in Right Ventricular Shape and Deformation Following Coronary Artery Bypass Surgery-Insights from Echocardiography with Strain Rate and Magnetic Resonance Imaging,” *Echocardiography*, vol. 32, no. 12, pp. 1809–1820, Dec. 2015.
- [209] B. Russell, D. Motlagh, and W. W. Ashley, “Form follows function: how muscle

- shape is regulated by work,” *J. Appl. Physiol.*, vol. 88, no. 3, pp. 1127–1132, Mar. 2000.
- [210] O. Frank, “Zur Dynamik des Herzmuskels,” *Zeitschr. Biol.*, vol. 32, pp. 370–437, 1895.
- [211] S. W. Patterson and E. H. Starling, “On the mechanical factors which determine the output of the ventricles,” *J. Physiol.*, vol. 48, no. 5, pp. 357–379, Sep. 1914.
- [212] A. J. BRADY, “Length-Tension Relations in Cardiac Muscle,” *Am. Zool.*, vol. 7, no. 3, pp. 603–610, Aug. 1967.
- [213] W. K. K. Weiwad, W. A. Linke, and M. H. P. Wussling, “Sarcomere Length–tension Relationship of Rat Cardiac Myocytes at Lengths Greater than Optimum,” *J. Mol. Cell. Cardiol.*, vol. 32, no. 2, pp. 247–259, Feb. 2000.
- [214] L. M. Hanft and K. S. McDonald, “Length dependence of force generation exhibit similarities between rat cardiac myocytes and skeletal muscle fibres,” *J. Physiol.*, vol. 588, no. 15, pp. 2891–2903, Aug. 2010.
- [215] D. G. ALLEN, B. R. JEWELL, and J. W. MURRAY, “The contribution of activation processes to the length–tension relation of cardiac muscle,” *Nature*, vol. 248, no. 5449, pp. 606–607, Apr. 1974.
- [216] A. M. Gordon and G. H. Pollack, “Effects of calcium on the sarcomere length-tension relation in rat cardiac muscle. Implications for the Frank-Starling mechanism,” *Circ. Res.*, vol. 47, no. 4, pp. 610–619, Oct. 1980.
- [217] R. E. Palmer, A. J. Brady, and K. P. Roos, “Mechanical measurements from isolated cardiac myocytes using a pipette attachment system,” *Am. J. Physiol. Physiol.*, vol. 270, no. 2, pp. C697–C704, Feb. 1996.

- [218] J. F. Saenz Cogollo, M. Tedesco, S. Martinoia, and R. Raiteri, “A new integrated system combining atomic force microscopy and micro-electrode array for measuring the mechanical properties of living cardiac myocytes,” *Biomed. Microdevices*, vol. 13, no. 4, pp. 613–621, Aug. 2011.
- [219] C. D. Williams, M. K. Salcedo, T. C. Irving, M. Regnier, and T. L. Daniel, “The length–tension curve in muscle depends on lattice spacing,” *Proc. R. Soc. B Biol. Sci.*, vol. 280, no. 1766, p. 20130697, Sep. 2013.
- [220] C. David Williams, M. Regnier, and T. L. Daniel, “Axial and radial forces of cross-bridges depend on lattice spacing,” *PLoS Comput. Biol.*, vol. 6, no. 12, 2010.
- [221] E. L. de Beer *et al.*, “Effect of sarcomere length and filament lattice spacing on force development in skinned cardiac and skeletal muscle preparations from the rabbit,” *Basic Res. Cardiol.*, vol. 83, no. 4, pp. 410–423, 1988.
- [222] O. Cazorla, Y. Wu, T. C. Irving, and H. Granzier, “Titin-based modulation of calcium sensitivity of active tension in mouse skinned cardiac myocytes,” *Circ. Res.*, vol. 88, no. 10, pp. 1028–1035, 2001.
- [223] D. ALLEN and J. KENTISH, “The cellular basis of the length-tension relation in cardiac muscle,” *J. Mol. Cell. Cardiol.*, vol. 17, no. 9, pp. 821–840, Sep. 1985.
- [224] T. M. Rothermel, B. L. Cook, and P. W. Alford, “Cellular Microbiaxial Stretching Assay for Measurement and Characterization of the Anisotropic Mechanical Properties of Micropatterned Cells,” *Curr. Protoc.*, vol. 2, no. 2, Feb. 2022.
- [225] E. Ehler, T. Moore-Morris, and S. Lange, “Isolation and culture of neonatal mouse cardiomyocytes,” *J. Vis. Exp.*, vol. 15, no. 79, pp. 1–10, 2013.
- [226] L. A. Taber, “Pattern formation in a nonlinear membrane model for epithelial

- morphogenesis,” *Acta Biotheor.*, vol. 48, no. 1, pp. 47–63, 2000.
- [227] L. A. Taber, B. B. Keller, and E. B. Clark, “Cardiac Mechanics in the Stage-16 Chick Embryo,” *J. Biomech. Eng.*, vol. 114, no. 4, pp. 427–434, Nov. 1992.
- [228] S. D. Boothe *et al.*, “The Effect of Substrate Stiffness on Cardiomyocyte Action Potentials,” *Cell Biochem. Biophys.*, vol. 74, no. 4, pp. 527–535, Dec. 2016.
- [229] J. G. Jacot, A. D. McCulloch, and J. H. Omens, “Substrate Stiffness Affects the Functional Maturation of Neonatal Rat Ventricular Myocytes,” *Biophys. J.*, vol. 95, no. 7, pp. 3479–3487, Oct. 2008.
- [230] Y. Guo and W. T. Pu, “Cardiomyocyte Maturation,” *Circ. Res.*, vol. 126, no. 8, pp. 1086–1106, Apr. 2020.
- [231] G. P. Farman, J. S. Walker, P. P. de Tombe, and T. C. Irving, “Impact of osmotic compression on sarcomere structure and myofilament calcium sensitivity of isolated rat myocardium,” *Am. J. Physiol. Circ. Physiol.*, vol. 291, no. 4, pp. H1847–H1855, Oct. 2006.
- [232] D. A. Martyn, B. B. Adhikari, M. Regnier, J. Gu, S. Xu, and L. C. Yu, “Response of Equatorial X-Ray Reflections and Stiffness to Altered Sarcomere Length and Myofilament Lattice Spacing in Relaxed Skinned Cardiac Muscle,” *Biophys. J.*, vol. 86, no. 2, pp. 1002–1011, 2004.
- [233] S. Göktepe, O. J. Abilez, K. K. Parker, and E. Kuhl, “A multiscale model for eccentric and concentric cardiac growth through sarcomerogenesis,” *J. Theor. Biol.*, vol. 265, no. 3, pp. 433–442, Aug. 2010.
- [234] R. Hassoun, H. Budde, A. Mügge, and N. Hamdani, “Cardiomyocyte Dysfunction in Inherited Cardiomyopathies,” *Int. J. Mol. Sci.*, vol. 22, no. 20, p. 11154, Oct.

2021.

- [235] L. Butler *et al.*, “Enhanced Characterization of Contractility in Cardiomyocytes During Early Drug Safety Assessment,” *Toxicol. Sci.*, vol. 145, no. 2, pp. 396–406, Jun. 2015.
- [236] J. C. Benech *et al.*, “Diabetes increases stiffness of live cardiomyocytes measured by atomic force microscopy nanoindentation,” *Am. J. Physiol. Physiol.*, vol. 307, no. 10, pp. C910–C919, Nov. 2014.
- [237] M. Papadaki *et al.*, “Diabetes with heart failure increases methylglyoxal modifications in the sarcomere, which inhibit function,” *JCI Insight*, vol. 3, no. 20, pp. 1–17, Oct. 2018.
- [238] M. Papadaki *et al.*, “Myofilament glycation in diabetes reduces contractility by inhibiting tropomyosin movement, is rescued by cMyBPC domains,” *J. Mol. Cell. Cardiol.*, vol. 162, no. August 2021, pp. 1–9, Jan. 2022.
- [239] M. Wheelwright, Z. Win, J. L. Mikkila, K. Y. Amen, P. W. Alford, and J. M. Metzger, “Investigation of human iPSC-derived cardiac myocyte functional maturation by single cell traction force microscopy,” *PLoS One*, vol. 13, no. 4, p. e0194909, Apr. 2018.
- [240] W. Dou *et al.*, “A microdevice platform for characterizing the effect of mechanical strain magnitudes on the maturation of iPSC-Cardiomyocytes,” *Biosens. Bioelectron.*, vol. 175, no. December 2020, p. 112875, Mar. 2021.
- [241] C. Y. Chen *et al.*, “Suppression of detyrosinated microtubules improves cardiomyocyte function in human heart failure,” *Nat. Med.*, vol. 24, no. 8, pp. 1225–1233, 2018.

- [242] M. A. Caporizzo, C. Y. Chen, A. K. Salomon, K. B. Margulies, and B. L. Prosser, “Microtubules Provide a Viscoelastic Resistance to Myocyte Motion,” *Biophys. J.*, vol. 115, no. 9, pp. 1796–1807, Nov. 2018.
- [243] P. Robison *et al.*, “Detyrosinated microtubules buckle and bear load in contracting cardiomyocytes,” *Science (80-.)*, vol. 352, no. 6284, Apr. 2016.
- [244] M. A. Caporizzo, C. Y. Chen, K. Bedi, K. B. Margulies, and B. L. Prosser, “Microtubules Increase Diastolic Stiffness in Failing Human Cardiomyocytes and Myocardium,” *Circulation*, vol. 141, no. 11, pp. 902–915, Mar. 2020.
- [245] V. P. Shirinsky *et al.*, “Mechano-chemical control of human endothelium orientation and size.,” *J. Cell Biol.*, vol. 109, no. 1, pp. 331–339, Jul. 1989.
- [246] S. Ueda, A. M. Blee, K. G. Macway, D. J. Renner, and S. Yamada, “Force Dependent Biotinylation of Myosin IIA by α -Catenin Tagged with a Promiscuous Biotin Ligase,” *PLoS One*, vol. 10, no. 3, p. e0122886, Mar. 2015.
- [247] M. S. Barnabei and J. M. Metzger, “Ex Vivo Stretch Reveals Altered Mechanical Properties of Isolated Dystrophin-Deficient Hearts,” *PLoS One*, vol. 7, no. 3, pp. 1–11, 2012.
- [248] D. Townsend *et al.*, “Chronic administration of membrane sealant prevents severe cardiac injury and ventricular dilatation in dystrophic dogs Find the latest version : Chronic administration of membrane sealant prevents severe cardiac injury and ventricular dilatation in dystroph,” *J. Clin. Invest.*, vol. 120, no. 4, 2010.
- [249] B. L. Cook and P. W. Alford, “Continuum interpretation of mechano-adaptation in micropatterned epithelia informed by in vitro experiments,” *Integr. Biol.*, vol. 15, pp. 1–16, Apr. 2023.

- [250] Y. Nakagawa, “Metabolism and toxicity of benzophenone in isolated rat hepatocytes and estrogenic activity of its metabolites in MCF-7 cells,” *Toxicology*, vol. 156, no. 1, pp. 27–36, Dec. 2000.
- [251] A. Wnuk, J. Rzemieniec, W. Lasoń, W. Krzeptowski, and M. Kajta, “Apoptosis Induced by the UV Filter Benzophenone-3 in Mouse Neuronal Cells Is Mediated via Attenuation of E_{α} /Ppar γ and Stimulation of E_{β} /Gpr30 Signaling,” *Mol. Neurobiol.*, vol. 55, no. 3, pp. 2362–2383, Mar. 2018.
- [252] J. L. Tan, W. Liu, C. M. Nelson, S. Raghavan, and C. S. Chen, “Simple Approach to Micropattern Cells on Common Culture Substrates by Tuning Substrate Wettability,” *Tissue Eng.*, vol. 10, no. 5–6, pp. 865–872, May 2004.
- [253] R. N. Palchesko, L. Zhang, Y. Sun, and A. W. Feinberg, “Development of Polydimethylsiloxane Substrates with Tunable Elastic Modulus to Study Cell Mechanobiology in Muscle and Nerve,” *PLoS One*, vol. 7, no. 12, p. e51499, Dec. 2012.
- [254] J. L. Teo *et al.*, “Caveolae Control Contractile Tension for Epithelia to Eliminate Tumor Cells,” *Dev. Cell*, vol. 54, no. 1, pp. 75–91.e7, Jul. 2020.
- [255] M. T. Yang, J. Fu, Y.-K. Wang, R. A. Desai, and C. S. Chen, “Assaying stem cell mechanobiology on microfabricated elastomeric substrates with geometrically modulated rigidity,” *Nat. Protoc.*, vol. 6, no. 2, pp. 187–213, Feb. 2011.
- [256] T. Razafiarison *et al.*, “Biomaterial surface energy-driven ligand assembly strongly regulates stem cell mechanosensitivity and fate on very soft substrates,” *Proc. Natl. Acad. Sci.*, vol. 115, no. 18, pp. 4631–4636, May 2018.
- [257] J. L. Teo, C. T. Lim, A. S. Yap, and T. B. Saw, “A Biologist’s Guide to Traction

Force Microscopy Using Polydimethylsiloxane Substrate for Two-Dimensional Cell Cultures,” *STAR Protoc.*, vol. 1, no. 2, p. 100098, Sep. 2020.

- [258] M. L. Rathod *et al.*, “PDMS Sylgard 527-Based Freely Suspended Ultrathin Membranes Exhibiting Mechanistic Characteristics of Vascular Basement Membranes,” *ACS Appl. Mater. Interfaces*, vol. 10, no. 47, pp. 40388–40400, Nov. 2018.

Appendix A. PDMS 527 coated membranes functionalized with fluorescent beads as TFM substrates for C μ BS

A.1 Introduction

C μ BS has proven to be an effective method for measuring the mechanical properties and growth and remodeling of both single cells and microtissues [45], [193], [249]. One limitation of C μ BS is the use of benzophenone to bond the polyacrylamide gel to the elastomer membrane. Benzophenone has been shown to be cytotoxic to cells [250], [251]. C μ BS uses a small amount of benzophenone and a three day rinse period to leach any residual benzophenone out of the membranes to reduce any adverse effects on cells. However, elimination of benzophenone is of potential interest to increase not only cell viability, but also the time effectiveness of substrate preparation.

Another common substrate for micropatterning cells is PDMS [252]. Several groups have used PDMS as a substrate when studying cellular mechanics [253]–[255]. In our own experience, established cell lines in culture and robust cell types such as fibroblast pattern well on PDMS substrates and PA gels for C μ BS. However, freshly isolated primary cells like embryonic heart cells from chick embryos are more sensitive to their extracellular environment. In general, these primary cells have difficulty adhering to the polyacrylamide gel C μ BS substrates, but pattern well on PDMS. Until now, we have not used PDMS as a substrate for C μ BS because of inability to incorporate fluorescent beads as fiduciary markers for traction force microscopy (TFM). Recently, several groups have described methods for adhering fluorescent beads to PDMS surfaces for performing TFM [256], [257]. Since PDMS has well characterized mechanical properties, tunable stiffness, and

does not require the use of benzophenone, it has the potential to be very useful as a substrate for performing C μ BS.

Here, I describe a method for preparing micropatterned PDMS substrates functionalized with fluorescent microspheres for performing TFM experiments using C μ BS. The protocol described here is adapted from Teo et al. [257] to work with C μ BS protocols as previously described [224] and standard micropatterning techniques.

A.2 Methods

A.2.1 Preparation of PDMS coated membranes

1. Elastomer membranes for C μ BS experiments are cut as previously described [224].
2. Membranes are cleaned in 70% ethanol and blown dry to remove any dust or debris from their surface.

Note: It is important that the surface of the membranes are clean so that there is a flat surface for spin coating.

3. A quartz disc or large, round coverslip is adhered to the center of the membrane.

Note: This provides a flat surface for spin coating and micropatterning later on.

4. Spin coat the membranes with PDMS 527 prepared in a 1:1 ratio by centering the membrane on the chuck and dropping enough uncured PDMS in the center of the membrane so that it will coat the surface.

Note: PDMS 527 will start to cure in 30 min – 4 hrs at room temp, changing its properties and thus how it behaves during spin coating. Prepare fresh PDMS if spin coating takes longer than 30 min.

Note: PDMS has known mechanical properties and spin coating time and speed can be changed to alter the thickness of the layer formed [258] and tunable stiffness can be achieved by mixing with PDMS 184 [253].

5. Coated membranes are removed from the spin coater and allowed to cure overnight at 80°C.
6. Assemble C μ BS constructs as normal by clamping membranes between brackets and placing them under slight tension. Take care not to touch the spun coated PDMS 527 layer as it is soft and slightly tacky and contact could deform the surface.
7. Adhere a flexible ring to the top of the membrane to form a well for solutions. Adhere a quartz disc to the bottom of the membrane to provide a flat, stable surface for micropatterning.

A.2.2 Silanization and functionalization of PDMS coated membranes

1. Prepare 5% (v/v) solution of 3-Aminopropyltriethoxysilane (APTES) (Acros Organics) in 100% ethanol.

Note: Prepare fresh solution each time as APTES is sensitive to moisture.
2. Add enough APTES solution to the membrane to cover the bottom of the well (~2-3 mL) for 20 min at room temp.
3. Aspirate the APTES solution, wash three times with 100% ethanol, and dry the dishes for 5 minutes at 80°C.
4. Prepare a 0.5% (v/v) solution of fluorescent, carboxylate-modified microspheres (Invitrogen) in distilled water. Mix thoroughly.

5. Add enough bead solution to cover the bottom of each well (~2-3 mL) and incubate silanized PDMS membranes in bead solution for 30 min at room temp.
6. Aspirate bead solution and wash three times with distilled water.
7. Incubate in 100 mM Tris solution for 10 minutes at room temp.
Note: This is to inactivate the bead surface.
8. Aspirate Tris solution, wash three times with distilled water, and dry dish at 80°C.

A.2.3 Micropatterning fibronectin for cell adhesion

1. PDMS stamps with features for micropatterning are cleaned by sonicating stamps in 100% ethanol for 30 min.
2. Stamps are blown dry and inked with 0.1 mg/ml fibronectin (Gibco) solution for 1 hr.
3. Stamps are blown dry and gently placed feature side down on the functionalized membranes for at least 30 min at room temp.

Note: Do not UV functionalize the PDMS before stamping. Some protocols for micropatterning PDMS require UV functionalization of the PDMS prior to transferring the pattern; however, UV exposure at this stage interferes with the bead attachment to the substrate.

Note: Contact between the stamp and substrate can be confirmed by looking through the bottom of the membrane. Gently setting the stamp on the surface should be sufficient to transfer fibronectin patterns to the substrate. Applying too much pressure will cause the soft substrate to come into contact with the recessed portions of the stamp making the resulting patterns less distinct.

4. Gently peel off the stamp and add PBS to the well.

5. A 4% bovine serum albumin or 1% pluronics solution can be used to prevent nonspecific binding or clean up the edges of the patterns, if necessary. Add solution for 30 min and rinse 3 times with PBS.
6. Constructs can be UV sterilized in a biosafety cabinet for 15 min to prevent contamination.
7. Constructs are now ready to be seeded with the desired cell type. Constructs can be kept in PBS for several days prior to seeding if necessary.

A.3 Preliminary Results

A.3.1 Strains are linearly transferred to the functionalized PDMS substrates.

C μ BS substrates were prepared according to the protocol above. Using a confocal microscope, beads were observed on the surface of the PDMS. Substrates were stretched uniaxially and no dislodgement of beads occurred. Images of the bead layer during stretching for strains up to 25% were compared to the undeformed bead layer in ImageJ using Linear Stack Alignment with SIFT. Affine registration was used to align the deformed and undeformed images generating the deformation matrix \mathbf{F} . The Green-Lagrangian strain was calculated using $\mathbf{E} = \frac{1}{2}(\mathbf{F}^T \cdot \mathbf{F} - \mathbf{I})$ and the x and y direction component of the strain were compared to the C μ BS applied grip strains (Fig A.1(A)). The measured strains in the directions parallel and orthogonal to stretch were consistent with previous measurements using C μ BS such that for every 5% applied strain, the substrate is strained ~4% in the stretch direction and ~-1% normal to the stretch.

A.3.2 Cells are able to be micropatterned on the surface and their tractions measured using functionalized PDMS substrates.

Human umbilical artery smooth muscle cells (HUASMCs) (PromoCell Inc.) were seeded onto functionalized PDMS 527 coated membranes micropatterned with rectangles (aspect ratio: 1:4) of fibronectin (Fig A.1(B)). C μ BS experiments were performed and data was collected as previously described [224]. Cells were stretched up to 25% applied strain in 5% increments. Resulting cell stress was measured at each stretch (Fig A.1(C)). Consistent with previous studies [44] stress in the HUASMCs was highly anisotropic with stress in the long axis (P_x) greater than the short axis (P_y). Additionally, the stress as a function of stretch was able to be measured.

Neonatal mouse ventricular myocytes were seeded onto substrates with rectangular (aspect ratio: 1:7) patterns of fibronectin (Fig A.1(D)). Images were acquired of the bead

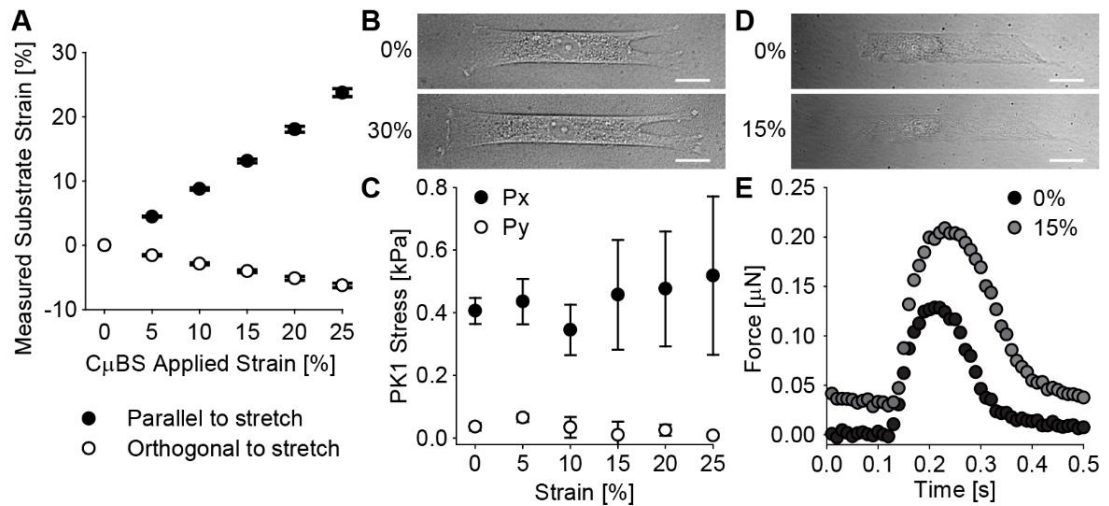


Figure A.1. Functionalized PDMS substrates function similarly to polyacrylamide gels for performing TFM and C μ BS.

(A) Measured substrate strains as a result of stretching with C μ BS, (B) Brightfield images of a micropatterned VSMC stretched to 30% applied strain, (C) Anisotropic stress-strain relationship for VSMCs measured on PDMS coated substrates (n=3), (D) Brightfield images of a micropatterned neonatal cardiac myocyte stretched to 15%, and (E) Corresponding traces of the total axial force exerted by the cardiac myocyte on the substrate during contraction. (scale bars: 20 μ m)

layer during unpaced contraction of a cardiac myocyte at 0% and 15% applied strain and used to calculate the temporal forces during contraction (Fig A.1(E)). Both the active and passive forces exerted by the myocyte increased at greater strains compared to the undeformed forces.

A.4 Conclusions

This work has demonstrated that PDMS membranes with a layer of PDMS 527 are able to be functionalized with fluorescent microspheres and micropatterned with fibronectin for cell adhesion. Strains are able to be transferred to the substrates and micropatterned cells and using images of the fluorescent bead layer, the resulting cellular forces and stresses are able to be obtained. Future work is need to characterize the thickness, stiffness, and smoothness of the PDMS 527 layer to ensure that the cells are sensing the stiffness of the spun coat layer and not the underlying membrane. Overall, this work demonstrates that the method described above offers an effective alternative to current methods for performing C μ BS and measuring cellular mechanical properties.